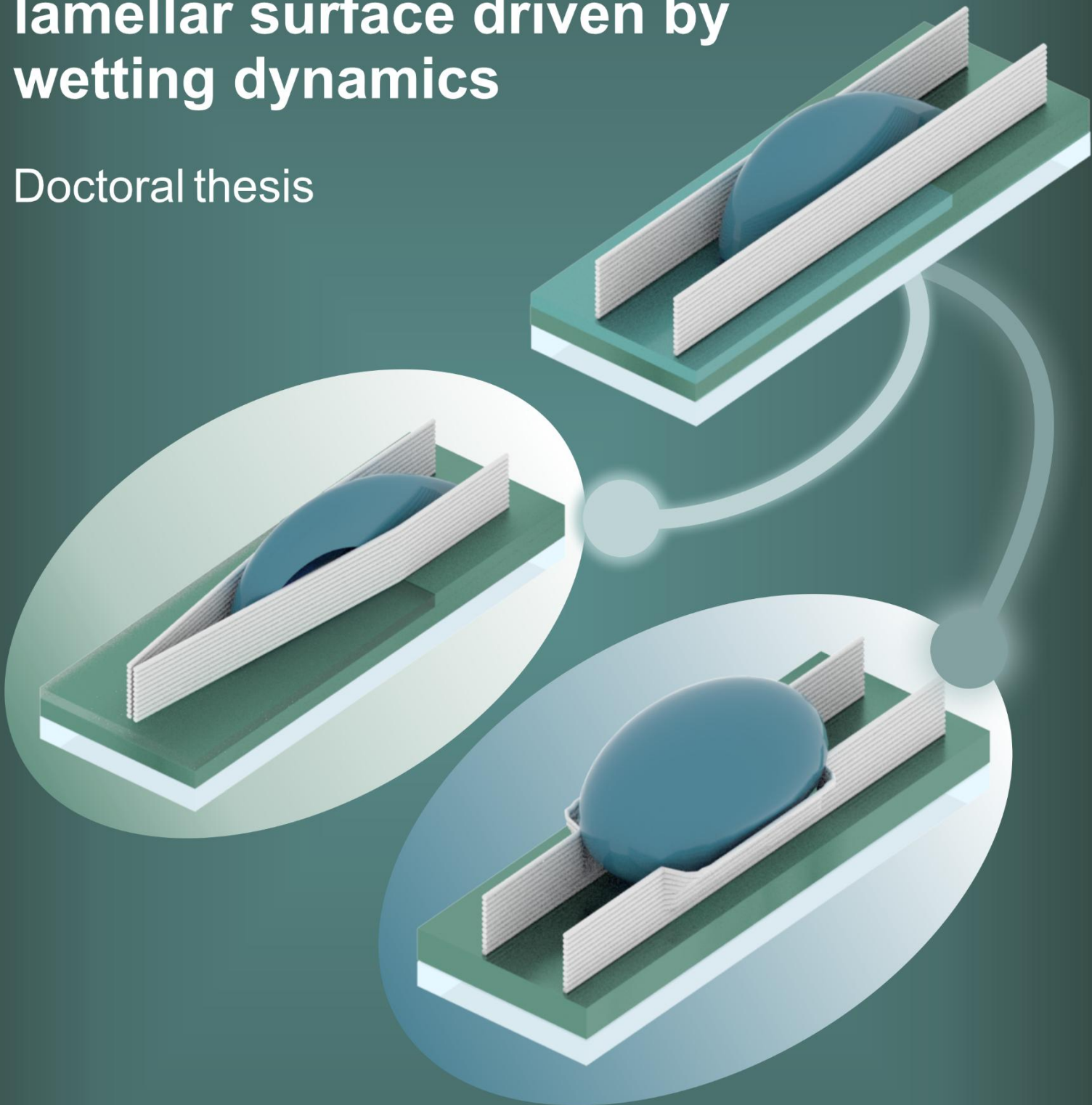# Tunable high aspect ratio lamellar surface driven by wetting dynamics

Doctoral thesis

Gissela Katherine Constante Ibarra

Supervised by Prof. Leonid Ionov

Bayreuth, 2025

Tunable high aspect ratio lamellar surface driven by wetting dynamics

DISSERTATION

zur Erlangung des akademischen Grades einer

Doktorin der Naturwissenschaften (Dr. rer. nat.)

im Rahmen des Promotionsprogramms Polymer Science

der Bayreuther Graduiertenschule für Mathematik und Naturwissenschaften

(BayNAT)

der Universität Bayreuth

vorgelegt von

Gissela Katherine Constante Ibarra

geboren in Ambato, Ecuador

Bayreuth 2025

This doctoral thesis was prepared at the department of Biofabrication Group at the University of Bayreuth from November 2019 until August 2024 and was supervised by Prof. Dr. Leonid Ionov.

This is a full reprint of the thesis submitted to obtain the academic degree of Doctor of Natural Sciences (Dr. rer. nat.) and approved by the Bayreuth Graduate School of Mathematical and Natural Sciences (BayNAT) of the University of Bayreuth.

Form of the dissertation: cumulative thesis

Date of submission: 14.08.2024

Admission by the executive board: 11.09.2024

Date of defence: 25.03.2025

Acting director: Prof. Dr. Jürgen Köhler

Doctoral committee:

Prof. Dr. Leonid Ionov   (reviewer)

Prof. Dr. Georg Papastavrou   (reviewer)

Prof. Dr. Johannes Brendel   (chairman)

Prof. Dr. Matteo Bianchini

Table of Contents

Summary

Bioinspiration from nature's designs fosters innovations in technology and materials science. By mimicking nature's designs, mechanisms, and systems, science has found creative alternatives to today's problems. This interdisciplinary approach not only advances technology but also promotes sustainable and efficient designs, where the interactions with the surfaces play an important role in the functionality of the organism or object. Understanding the interplay between surface topography and chemistry is essential in developing new surfaces and technologies, and by influencing the wetting state, one can achieve manipulation of droplets, or development of actuators. With the advent of smart materials, the potential applications for switchable surfaces in materials science have expanded. Smart materials can be used to fabricate surfaces that can switch their chemistry or physical properties to modify their wetting behavior. Understanding how water dynamics modify the topography of these smart surfaces will provide valuable insights for developing smart devices and microfluidic-controlled systems.

This research aims to develop high-aspect-ratio lamellar surfaces using shape memory polymers, elucidate the impact of water droplet dynamics on tunability, and explore potential applications in smart devices. The study combines simulation modeling, experimental fabrication, and analysis using melt-electrowriting to create and examine high-resolution surfaces. Key findings include the ability of thermoresponsive materials to change shape and wetting states, and their potential in microfluidic devices and smart valves. The high-aspect-ratio lamellar surfaces composed of shape memory polymer exhibit significant deformation under water droplet dynamics. These high-aspect-ratio surfaces play a crucial role in the degree of deflection of the lamellae under external forces. For a better understanding of the tunable topography by wetting, this dissertation focuses on the interplay of mechanical properties, surface tension, and topographical surface characteristics.

Publications stemming from this research demonstrate the creation of thermally controlled smart valves in microfluidic devices, light-induced deformation for precise fluid interaction control, and the role of elastocapillarity in smart surfaces. Overall, this work advances materials science by providing new insights into the fabrication and application of bioinspired surfaces, highlighting the significant potential of smart materials with shape-changing capabilities for innovative technologies such as the fabrication of smart devices.

Zusammenfassung

Die Bioinspiration durch das Design der Natur fördert Innovationen in der Technologie und Materialwissenschaft. Durch die Nachahmung der Designs, Mechanismen und Systeme der Natur hat die Wissenschaft kreative Alternativen für die Probleme von heute gefunden. Dieser interdisziplinäre Ansatz bringt nicht nur die Technik voran, sondern fördert auch nachhaltige und effiziente Designs, bei denen die Wechselwirkungen mit den Oberflächen eine wichtige Rolle für die Funktionalität des Organismus oder Objekts spielen. Das Verständnis des Zusammenspiels zwischen Oberflächentopographie und Chemie ist für die Entwicklung neuer Oberflächen und Technologien von entscheidender Bedeutung, da es den Benetzungszustand, die Manipulation von Tröpfchen oder die Entwicklung von Aktuatoren beeinflusst. Mit dem Aufkommen intelligenter Materialien haben sich die potenziellen Anwendungen für schaltbare Oberflächen in der Materialwissenschaft erweitert. Intelligente Materialien können zur Herstellung von Oberflächen verwendet werden, die ihre chemischen oder physikalischen Eigenschaften ändern können, um ihr Benetzungsverhalten zu modifizieren. Wenn man versteht, wie die Wasserdynamik die Topografie dieser intelligenten Oberflächen verändert, erhält man wertvolle Erkenntnisse für die Entwicklung intelligenter Geräte und mikrofluidisch gesteuerter Systeme.

Ziel dieser Forschungsarbeit ist die Entwicklung lamellarer Oberflächen mit hohem Aspektverhältnis unter Verwendung von Formgedächtnispolymeren, die Klärung der Auswirkungen der Wassertropfendynamik auf die Abstimmbarkeit und die Erforschung möglicher Anwendungen in intelligenten Geräten. Die Studie kombiniert Simulationsmodellierung, experimentelle Herstellung und Analyse mittels Schmelzelektrolyse, um hochauflösende Oberflächen zu erzeugen und zu untersuchen. Zu den wichtigsten Ergebnissen gehören die Fähigkeit thermoresponsiver Materialien, ihre Form und ihren Benetzungszustand zu verändern, sowie ihr Potenzial für mikrofluidische Geräte und intelligente Ventile. Die lamellaren Oberflächen mit hohem Aspektverhältnis, die aus Formgedächtnispolymeren bestehen, weisen eine erhebliche Verformung unter der Dynamik von Wassertröpfchen auf. Diese Oberflächen mit hohem Aspektverhältnis spielen eine entscheidende Rolle für den Grad der Ablenkung der Lamellen durch äußere Kräfte. Um die durch Benetzung einstellbare Topographie besser zu verstehen, konzentriert sich diese Dissertation auf das Zusammenspiel von mechanischen Eigenschaften, Oberflächenspannung und topographischen Oberflächenmerkmalen.

Die aus dieser Forschung hervorgegangenen Veröffentlichungen zeigen die Schaffung thermisch gesteuerter intelligenter Ventile in mikrofluidischen Geräten, die lichtinduzierte Verformung zur präzisen Steuerung von Flüssigkeitsinteraktionen und die Rolle der Elastokapillarität in intelligenten Oberflächen. Insgesamt bringt diese Arbeit die Materialwissenschaft voran, indem sie neue Einblicke in die Herstellung und Anwendung von bioinspirierten Oberflächen liefert und das bedeutende Potenzial intelligenter Materialien mit formverändernden Fähigkeiten für innovative Technologien wie die Herstellung intelligenter Geräte hervorhebt.

1.   Introduction

1.1. Bioinspiration and biomimicry

The process of evolution through natural selection has led to the development of organisms with modified structures, surfaces, and organs, aimed at optimizing functionality and increasing the survival rate and reproductive success of the species.[1] The preservation of the species depends on their capacity to adapt to the changing environment like modification from leaves to spines of desertic plants to avoid dehydration. This is an example that involves structural adaptations.[2] As well, organisms can go through behavioral adaptation[2] for example the hibernation of animals in winter to save energy. Bioinspiration uses the "know-how" of biology and applies it to non-biological technologies for the development of new materials, devices, and structures by studying the processes that nature has created to optimize functionality.[3]

There are multiple examples of bioinspired surfaces used in industry, medicine, and technology development, as depicted in **Figure 1.** One significant example of bioinspired surfaces is the lotus leaf, which has been widely studied for its self-cleaning properties.[4-6] The poor wettability of the surface allows it to remove dust and impurities from the leaf. Taking a close sight of the surface, one can observe the presence of micro and nano bumps, which increases the roughness of the surface.[6] This diminishes the spreading of the water drops on the surface due to its high surface energy, leading to the rolling of the water droplets.[7] The characteristic hydrophobicity of the lotus leaf is also explained by its surface chemistry. Nanoscopic tubular wax crystals are found on the bumps with a density of 200 tubules per 10 μm^2.[8] Bioinspiration of lotus leaf led to the creation of materials with self-cleaning and anti-biofouling properties that are commonly used for paint coatings for ships and walls as presented in **Figure 1a**.

In robotic development, researchers investigate the structured surface of the gecko's feet to develop adaptative adhesion on soft grippers (**Figure 1b**).[9] The presence of sticky setal arrays on toes is responsible for adhering to almost any surface. Each seta ends up in a spatula-like structure at the end, which binds to other surfaces through Van der Waals forces. These forces are broken by bending. The enhanced adhesion was used as a soft gripping system that has the ability to manipulate objects with different shapes.[9] Furthermore, this innovative

technology has been applied to develop gecko-like surfaces for robotic feet, enabling robots to walk on vertical surfaces.[10]

Self-cleaning not only avoids the accumulation of unwanted materials on the surfaces but also allows for the air-retaining surface. The bioinspired self-cleaning surface of salvinia leaf was used in the development of coatings to reduce water drag on ships (**Figure 1c**).[11, 12] The hydrophobic pillars with hydrophilic tips in the leaf surface help to retain air. The pillars that have a complex shape are coated with nanoscale wax crystals. The hydrophobic nature of the wax crystals prevents water from penetrating between the hairs. The top of the pillars contains hydrophilic molecules. The hydrophilic tips are in permanent contact with water, which pins the water at the air-water interface. Coating layers created with this surface were applied on the hull of ships. The Salvinia-effect coat increased the ship's speed due to the water drag reduction and reduced the energetic costs.[13]

Bioinspiration also was used to solve drought problems by collecting water from fog in desertic areas as the desert beetles do it (**Figure 1d**). A pattern of hydrophilic bumps and hydrophobic channels on the beetles' shells helps to accumulate water molecules from the air moisture. After the accumulation, the beetle leans and water drips to its mouth.[14] Water harvesting uses the same principle, the combination of hydrophilic areas to accumulate water from fog and hydrophobic sections for collection of water. Yu and collaborators created a patterned fabric with wettability gradient, mimicking the bumped surface of the Namib desert beetle to collect water from fog harvesting.[15] The fog collector was made by netting superwettable and superhydrophobic yarn and depositing copper particles on top of the mesh. Copper particles increase the thermal conductivity of the mesh which enhanced the collection of water. Another interesting application to mimic beetle-patterned shells, a net made from polypropylene was used by the organization FogQuest to create fog collectors. The mesh is woven in a stretched triangular pattern enabling the accumulation and rapid run-off of the water into the collectors.[16] This project has been implemented in various countries where water supply accessibility is either limited or not suitable for human consumption. It serves as a clear example of how bioinspiration has been utilized not only to develop new technologies but also to address social issues.

In conclusion, the intricate surfaces and features of biological organisms remain a wellspring of inspiration driving advancements across diverse fields, spanning from robotics to biotechnology and medical devices. This enduring influence of nature on human innovation

underscores the importance of continued exploration into organisms for future breakthroughs. Bioinspiration stands out as a pivotal strategy in the quest for novel ideas, yet it presents significant challenges. Indeed, mimicking nature requires a profound understanding of its mechanisms—a pursuit currently at the forefront of materials science research. Central to this endeavor is unraveling the intricate interplay of chemistry and physics within biological systems, serving as a cornerstone for the development of innovative materials.
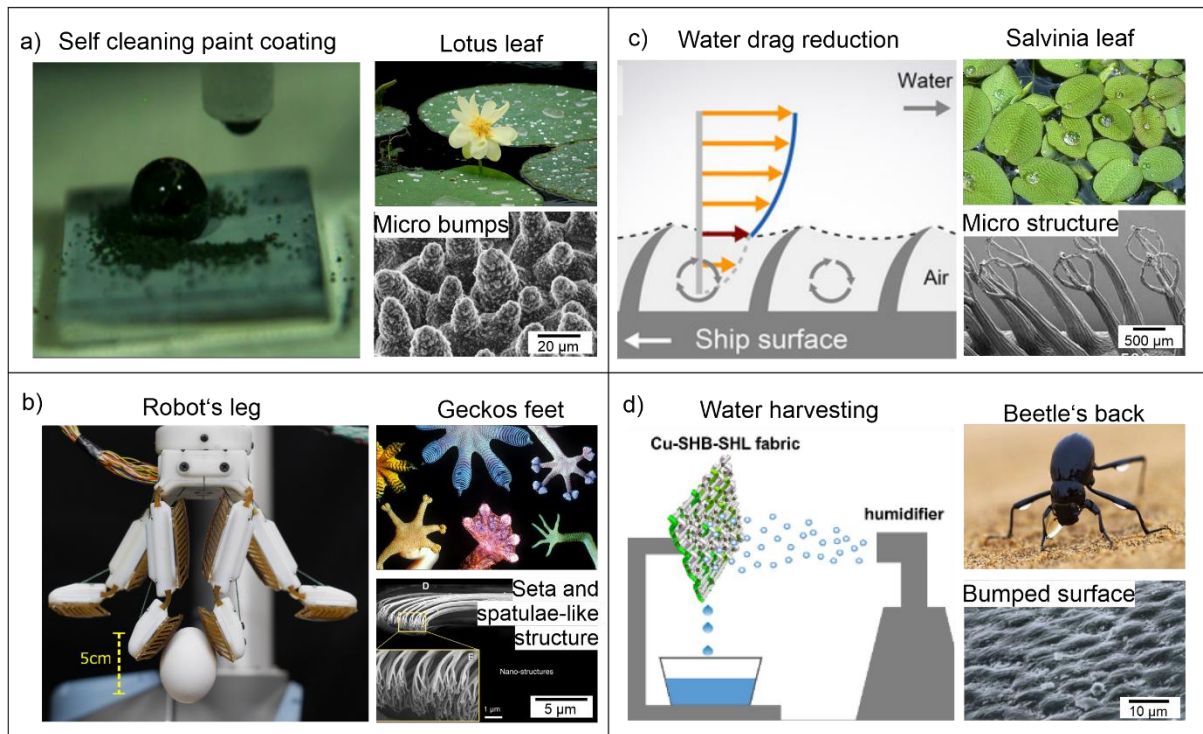

Figure 1. Bioinspiration and biomimicry with the correspondence organisms. **a)** Self-cleaning painting[17]. [Reprinted with permission from [17]. AAAS]. Lotus leaf[18] and its micro and nanostructured surface.[8] [Reproduced with permission from [8]. Copyrights © 2011 Creative Commons] **b)** Bioinspired robotic gripping fingers [9] from Gekos' feet.[19] [Reproduced with permission from [19]. Copyright © 2002, The National Academy of Sciences]. SEM image of the surface of the seta and spatula-like structure.[20] [Reproduced with permission.[20] Copyright © 2010 WILEY-VCH Verlag GmbH & Co. KGaA, Weinheim]. **c)** Salvinia effect used to coat ships for drag reduction[12] [Reproduced with permission from [12]. Copyrights © 2021WILEY-VCH GmbH] that contain the same microstructure surface[21] [Reproduced with permission.[21] Copyright © 2010, WILEY-VCH Verlag GmbH & Co. KGaA, Weinheim] as the salvinia leaf,[22] [Reproduced with permission from [22]. Copyright © 2003, Kurt Stueber] and **d)** harvesting of water from fog[15] [Reproduced with permission from [15]. Copyright © 2021,

Elsevier] as the Namib desert beetle[23] [Foto: Martin Harvey, Alamy], which possess a bumped surface.[24] [Reproduced with permission from [24]. Copyright © 2001, Springer Nature Limited].

1.2. Wettability of surfaces

The previous chapter explained the potential of bioinspiration in the development of new materials and surfaces. All the examples cited before share one common feature - the specificity of their wettability properties is strongly linked to some functionalities of the organism. Wettability is a physical property describing the ability of a surface to get wetted – hydrophilic – or not – hydrophobic – by the spreading or not of the liquid droplet.[25] The description of the wettability is made through the analysis of the interaction between a fluid, typically water, and the surface. The interaction between the surface and the liquid droplet can be measured by the surface contact angle (θ), which is determined by the surface energy (γ) between the liquid (L) and the solid (S), liquid and gas (G) (air), and solid and gas,[26] as shown in **Figure 2**. The contact angle is also measured as the angle formed between the right and left edge of the water droplet, using the solid surface as a baseline. When the contact angle is higher than 90°, the surface is known as hydrophobic, while contact angles lower than 90° present hydrophilic properties.
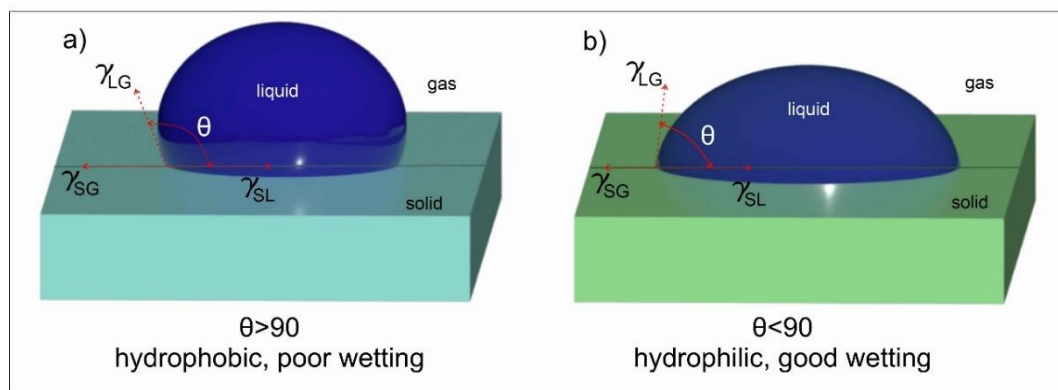
**Figure 2.** Contact angle scheme of **(a)** hydrophobic, and **(b)** hydrophilic surfaces.

1.2.1. Modification of wettability: surface chemistry and surface topography

The exceptional wetting properties of the organisms are explained by the synergy between the surface chemistry and surface topography. By creating a surface with a particular architecture, the interaction of the water with the solid surface can become weaker leading to the water drop to spherilize. Similarly, active chemical groups on the surface can induce or reduce wettability.

Surface chemistry

When considering the forces involved in wetting, one primarily looks at the interplay between cohesive forces within the liquid and adhesive forces between the liquid and the solid surface. The capacity of water to form hydrogen bonds with the surface allows the water to spread on the surface. Hydrophilic groups - such as hydroxyl groups (-OH) present in sugars and alcohols, carbonyl groups; (-C=O) in aldehydes and ketones; carboxyl groups (-COOH) in carboxylic acids; amino groups (-NH$_2$) found in amino acids; and sulfhydryl groups (-SH) also known as thiol group, can establish hydrogen bonds with water molecules (**Figure 3a**). As a result, the water spreads on the surface leading to a contact angle close to zero, ending in complete wetting of the surface.[27]

On the other hand, if water cannot form hydrogen bonds with the functional group moieties on the surface, the cohesion force between water molecules becomes stronger, preventing the liquid from spreading across the surface. Hydrophobic groups such as methyl groups (-CH$_2$) and rings of hydrocarbons lack the ability to form hydrogen bonds (**Figure 3b**). Consequently, the surface energy of hydrophobic materials is relatively low, causing water droplets to bead up with high contact angle values. Natural hydrophobes like wax, oil, fats, and alkanes exhibit unique functional properties such as waterproofing, antifouling, corrosion resistance, and self-cleaning.[28]
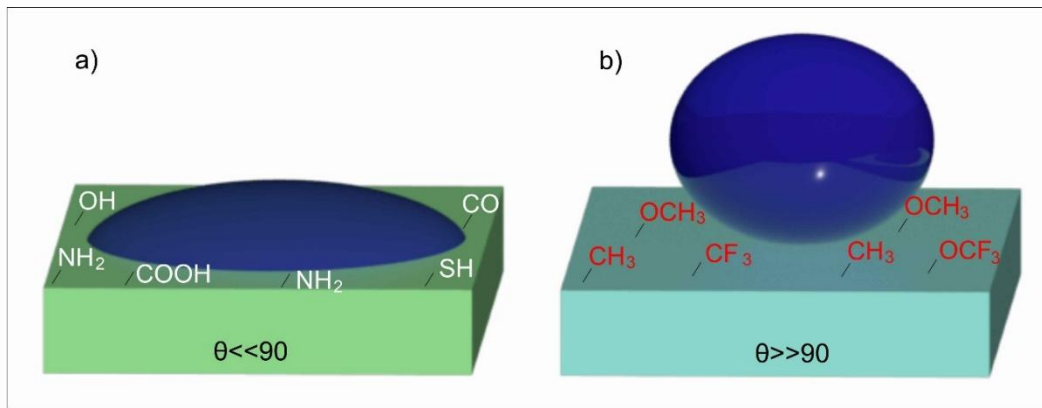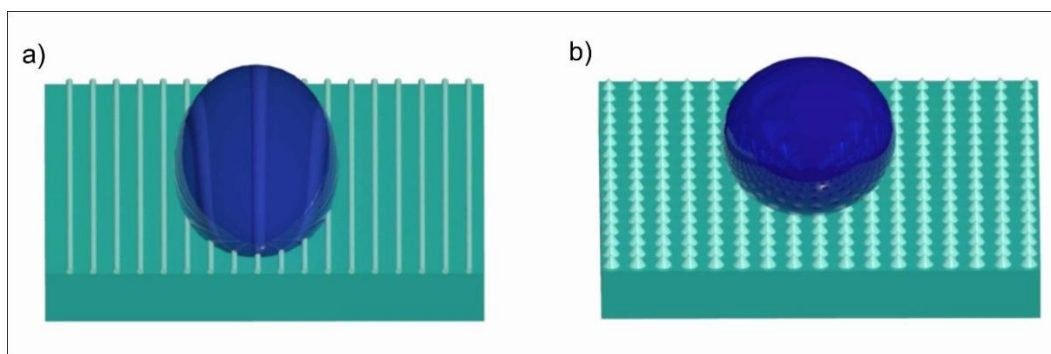
Figure 3. Scheme of wetting behavior by changing the surface chemistry: **a)** when the surface has hydrophilic functional groups and **b)** hydrophobic groups.

Surface topography

Surface topography plays a significant role in determining the wetting behavior of a surface. The roughness or texture of a surface can influence the contact angle, in general, rougher surfaces tend to have higher contact angles compared to smoother surfaces. This means that liquids may bead up more on rough surfaces and spread out more on smooth surfaces. The exact effect depends on the specific topography of the surface, as observed in **Figure 4**. On a surface with a longitudinal orientation topography provides directional wetting (**Figure 4a)**, or enhances the hydrophobicity (**Figure 4b**). Additionally, the roughness of the surface leads to an increase in the surface area, providing more opportunities for interactions between the liquid and the surface, including van der Waals forces and hydrogen bonding. These interactions can enhance wetting by promoting better adhesion of the liquid to the surface. This phenomenon occurs for surfaces that have small contact angles, whereas surfaces with large contact angles exhibit the opposite effect, rounded droplets, as observed in the lotus leaf effect.

A combination of surface topography and surface chemistry produces surfaces with very large contact angles for hydrophobic materials or small contact angles to achieve complete wetting. Development and fabrication of such surfaces are constantly investigated, as well as the proper modeling to describe and predict the behavior of liquid droplets on the surface.

Figure 4. Scheme of wetting behavior by changing the topography of the surface: **a)** directional wetting by fabrication of parallel pattern, and **b)** bumpy surface to increase the contact angle of the droplet.

1.2.2. Basic theories of the mechanism of wetting

The mechanism of wetting involves several interrelated phenomena, including surface tension, adhesion, and cohesion. Surface tension is the force that causes molecules at the surface of a liquid to minimize their surface area, resulting in the formation of a cohesive film. When the liquid comes into contact with a solid surface, surface tension minimizes the contact area between the liquid and the solid. Adhesion is the attraction between molecules of different substances. When a liquid contacts a solid surface, adhesive forces between the liquid molecules and the solid surface pull the liquid toward the surface. Cohesion refers to the attraction between molecules of the same substance. Cohesive forces within the liquid cause it to resist deformation and maintain its integrity.[29]

The interaction between a liquid droplet and a surface is intricately governed by the interplay of their respective surface energies. As discussed earlier, the contact angle of the liquid serves as a crucial indicator of the surface's wettability. Accurately estimating this contact angle is paramount for enhancing surface design and creation. This estimation hinges on Young's equation, which forms the basis for predicting the contact angle and thus enables precise manipulation of surface properties.

Contact angle: Young's equation

The wetting behavior is explained by Young's model[30] on a smooth solid surface (**Figure 2**), and Wenzel's model[31] and Cassie-Baxter model[32] describe the wetting on an inhomogeneous surface (**Figure 5**),. According to Young's equation, the equilibrium contact angle is:

$$cos\theta = \frac{\gamma_{SG} - \gamma_{SL}}{\gamma_{LG}}$$

<div align="right">

Equation 1

</div>

Where θ represents the contact angle, and γ is the surface tension. L, S, and G are liquid, solid, and gas, respectively.

The contact angle (θ) is the angle formed between the tangent to the liquid surface at the point of contact and the solid surface (**Figure 2**). As explained before, a small contact angle indicates strong wetting. For complete wetting, the liquid completely spreads across the solid surface, forming a thin, continuous film. This occurs when the adhesive forces between the liquid and the solid are stronger than the cohesive forces within the liquid. Partial wetting occurs when the liquid partially spreads across the solid surface, forming droplets or a partial film. This occurs when the cohesive forces within the liquid are stronger than the adhesive forces between the liquid and the solid. Non-wetting surfaces occur when the liquid forms droplets on the solid surface and does not spread at all. In this case, the cohesive forces within the liquid are much stronger than the adhesive forces between the liquid and the solid.[33]

Contact angle: Wenzel and Cassie-Baxter state

For a better understanding of the interaction of the liquid-solid interface, is needed to consider the roughness of the surface. Under this statement, two states can be distinguished: the Wenzel state for weak hydrophobicity and the Cassie-Baxter state for strong hydrophobicity.[34]

Wenzel's equation: $cos\theta_W = r(\gamma_{SG} - \gamma_{SL})/\gamma_{LG}$

<div align="right">

Equation 2

</div>

Cassie – Baxter equation: $cos\theta_{CB} = f[(\gamma_{SG} - \gamma_{SL})/\gamma_{LG}] - (1 - f)$

Equation 3

Where r represents the roughness ratio factor ($r = A_{rough}/A_{flat}$), r is always bigger than 1. Thus, as r increases, the total interface energy also increases, leading to an increment in the hydrophobicity on hydrophobic surfaces, or increasing the wettability on hydrophilic surfaces. f is the fraction of the solid/liquid interface in the entire composite surface beneath the liquid.
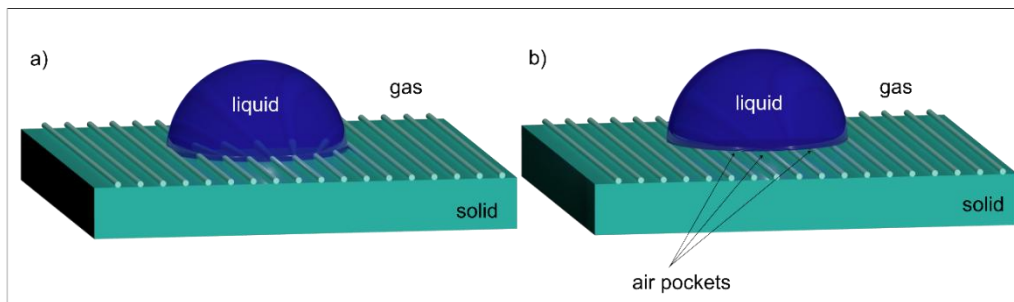
Figure 5. a) Wenzel model and **b)** Cassie-Baxter model on rough surfaces showing different states of wetting.

Based on **Equation 2**, roughness can increase the contact angle when the surface is hydrophobic or reduce the contact angle when is hydrophilic. Both modifications can achieve wettability gradients without modifying the surface chemistry. In the Wenzel state (**Figure 5a**), the liquid on the surface enters the grooves, resulting in higher surface wettability due to the increase in contact area. In contrast, in the Cassie–Baxter state (**Figure 5b**), the air remains trapped in the grooves. This results in a higher contact angle compared to the contact angle on a flat surface:[35]

Sliding contact angle

Unlike the static contact angle, which is measured when the droplet is at rest, the sliding contact angle provides insights into the wetting behavior under dynamic conditions, such as when a droplet is moving or spreading on a surface. It takes into account the influence of factors

such as surface roughness,[36, 37] surface energy,[38] viscosity of the liquid,[39], and velocity of the droplet.[40] The sliding contact angle may change during the dynamic wetting process, influenced by these factors. A surface with lower energy tends to exhibit lower contact angle hysteresis, facilitating easier droplet movement. The contact angle hysteresis is the difference between the advancing contact angle and receding contact angle and provides information about the pinning or depinning behavior of the droplet on the solid surface. The advancing contact angle refers to the contact angle measured when the droplet is moving forward, while the receding contact angle is measured when the droplet is retracting or receding. (**Figure 6**)

In a typical wetting experiment using the tilted plate method, a drop is placed onto a surface, which is then inclined until the drop begins to slide. When the droplets slide down on tilted surfaces, the driving motion force, in this case the external gravitational force F_g, (**Equation 4**) can be modified by changing the tilting angle α,[41] to control the droplet velocity.[42]

$$F_g = mg \, \sin \alpha$$

Equation 4

Where m is the mass of the water drop, g is the acceleration of gravity (9.81 m/s^2).
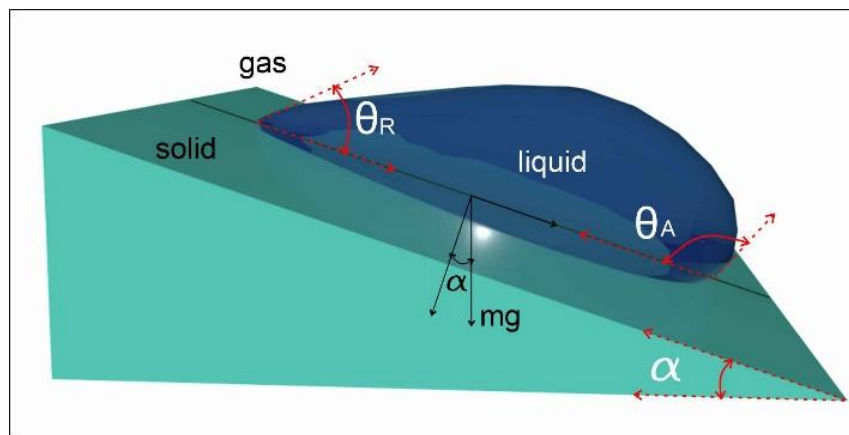
Figure 6. Sliding droplet at an inclined surface at α tilting angle.

1.3. Elastocapillarity

The phenomenon of elastocapillarity is an interplay between elasticity and capillarity and occurs when the surface tension of a liquid interacts with the deformable properties of a solid material. The deformation of a soft solid can be expressed by the bending or collapsing of beams and films under the influence of capillary forces. The extent of deformation is determined by a complex interaction of factors, including the surface tension of the liquid, the mechanical properties of the solid material, and the geometric arrangement of the system.[43]

When the walls – lamellae are rigid, the capillary height is determined by Jurin's law.[44] This law balances the capillary forces and the weight of the liquid column:

$$h = \frac{2\gamma \cos\theta}{\rho g d}$$

Equation 5

Where h is the height of the rising liquid between the walls, γ and ρ are the surface tension and density of the liquid, respectively; and d is the distance between the walls.

Nevertheless, when the walls are soft and flexible and are fixed in one end as in **Figure 7,** the liquid brings the walls together. This reduces of distance and increases the capillary rise of the liquid.[44] Elastocapillarity length (L_{EC}) is the length of the walls above which capillary-driven coalescence occurs and can be calculated as following:[44]

$$L_{EC} = \sqrt{B/\gamma}$$

Equation 6

Where B is the bending stiffness and γ liquid surface tension. B of the material is derived from the Euler-Bernoulli Beam equation resulting in:[45]

$$B = Eb^3/12(1 - v^2)$$

Equation 7

Where E is Young's modulus, b is the thickness of the sheet, and v is the Poisson ratio of the material. Euler-Bernoulli Beam equation describes the bending deformation. It states that the bending curvature is proportional to the bending moment applied and inversely proportional to the flexural rigidity (EI), where E is the modulus of elasticity and I is the area moment of inertia. This equation makes the following assumptions: the material is homogeneous and isotropic, and neglects the deformation of the cross-section, because, in spite that the neutral axis of the beam is curved after deformation, the deformed angles are small.[46]

When the walls are long enough ($>L_{EC}$) and two of them have collapsed together (ℓ_B), there is left a gap separated by the distance d, named L_d. For walls with L_{EC} lower than L_d, there is no bending or collapsing of the walls, avoiding stiction of them. L_d is estimated by:

$$L_d^4 = 9d^2 L_{EC}^2/2$$

Equation 8

This considers $d<<L_d$, gravity is neglected, and the adhesion is limited only to the bending energy. Under this statement, L_d is independent of the total length of the walls.[47, 48]
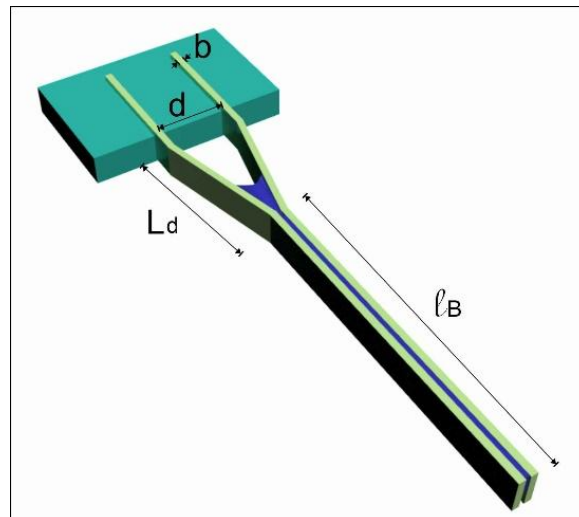
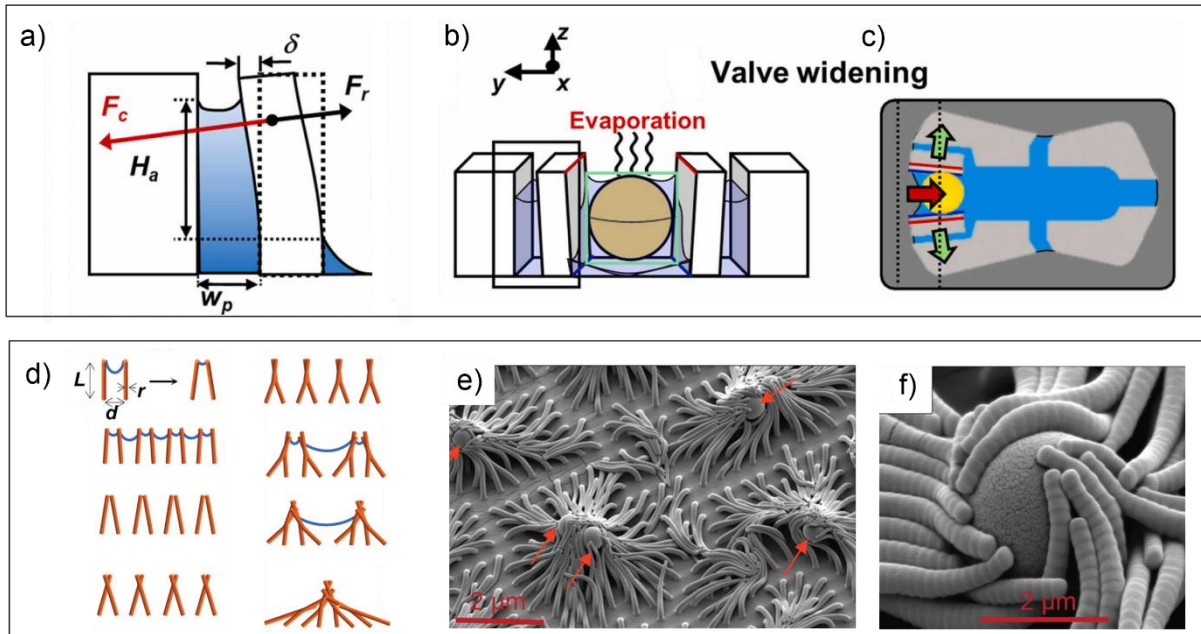**Figure 7.** Elastocapillary effect on bending beams that are clamped in one edge.

1.3.1. Elastocapillarity applications

Understanding and manipulating elastocapillary coalescence can lead to the development of novel techniques and materials with tailored properties and functionalities. Elastocapillary coalescence has applications in various fields, including microfluidic device fabrication,[49] surface patterning,[50] and the design of functional materials.[51] By harnessing the interaction between liquid droplets and deformable surfaces, scientists can engineer materials with tailored wetting behaviors. This has implications for a wide range of applications, including self-cleaning surfaces, anti-fog coatings, and adhesion control in biological systems.

One key application of elastocapillarity is in the study and development of microfluidic devices. In **Figure 8a-c,** Lee and collaborators fabricated an open-microfluidic device with a particle docking system. The PDMS microplates can reversibly bend as a valve for trapping the particles.[52] This technology is versatile for a wide range of applications, including multiplexed bioassays for drug screening and cytotoxicity assessments. The device utilizes spontaneous evaporation to drive particle coupling, improving process efficiency. Nevertheless, despite its advantages, the requirement for complex chip fabrications may limit its widespread adoption among end users. The relationship between the degree of evaporation and preconcentration efficiency requires further characterization in follow-up studies to fully understand and optimize the process. The driving force of the open-microfluidic device is the capillary force to open the docking system for particles, making it an easy and spontaneous way to control the device.

Another interesting application is the self-organized bristles (**Figure 8d-f**). Pokroy and collaborators study and develop a theoretical model to characterize the geometry of bundles. The hierarchical assembly of the clusters is used for trapping particles and also adhesive properties.[53] The assembling of the bundles is made by the bend of the fibers when come in contact with a liquid. This process showcases the potential for creating complex materials through simple physical principles.

These interesting applications related to the elastocapillarity phenomenon show the potential of exploiting this effect to construct devices with remote control, or even in biotechnological applications for substances detection. Proper analysis and modeling are essential to apply this technology in future devices.

Figure 8. Elastocapillary effect on soft substrates for **a-c)** switchable elastocapillary functional valve on microfluidics,[52] [Reproduced with permission from [52]. Copyrights © 2022 Elsevier B.V. All rights reserved] and **d-f)** self-organized helical blisters for particle trapping.[53] [From [53] / Reprinted with permission from AAAS]

## 1.4. Smart surfaces: Tuning the wettability

Smart surfaces with tunable wettability hold immense promise across diverse applications. In industries like oil and gas, where efficient separation of oil and water is crucial,[54] these surfaces offer enhanced performance and reduced environmental impact. In the biomedical field, they enable precise control over liquid interactions for applications like drug delivery, tissue engineering, and diagnostics. Additionally, in consumer electronics, smart surfaces can prevent water damage and improve the durability of devices.

Traditionally, surfaces were perceived as passive with fixed properties, but the development of smart materials and nanotechnology has enabled the progress of surfaces that dynamically alter their wettability in response to external stimuli. This transformative capability not only opens new avenues for innovation but also addresses challenges in fields ranging from fluid dynamics to biomimicry.

The concept of tunable wettability refers to surfaces that can switch between hydrophobic and hydrophilic states or exhibit gradients of wettability across their surface. This tunability is achieved through various mechanisms, including changes in surface chemistry, morphology, and the application of external stimuli such as temperature, light, or electric fields.

Some examples of the development of smart surfaces with diverse wetting are presented in **Figure 9**. For instance, Zhang and colleagues fabricated a flat and wrinkled surface grafted with a pH-responsive polymer (**Figure 9a**). It was observed that the wetting switchability range is higher for wrinkled surfaces going from total wetting (~10° CA) to a hydrophobic behavior (>120° CA).[55]

Not only pH modification can lead to several states of wetting. Temperature-responsive surfaces are a major interest of scientists. One interesting approach is presented by Song and collaboration. They fabricated a surface with unidirectional motion of droplets that is conducted by switching of temperature (**Figure 9b**).[56] The main component of the surface is the PNIPAAm, at 25°C the polymer is hydrophilic, allowing the spreading of the droplet, but when the temperature increases to 55°C, the PNIPAAm surface becomes hydrophobic, in this case, the droplet is pinned on the surface. By the switching of temperature, the droplet can increase and decrease its contact line which allows it to move along the surface in a controlled manner. As well, controlling the transportation of droplets is also achieved by creating a magnetically responsive surface as presented by Yang and colleagues (**Figure 9c**). A magnetically responsive superhydrophobic microfibrillar surface can switch the adhesion to pin and unpin the droplets This surface can be used for programmable fluid collection and transport of smart microfluidic devices fabrication.[57]
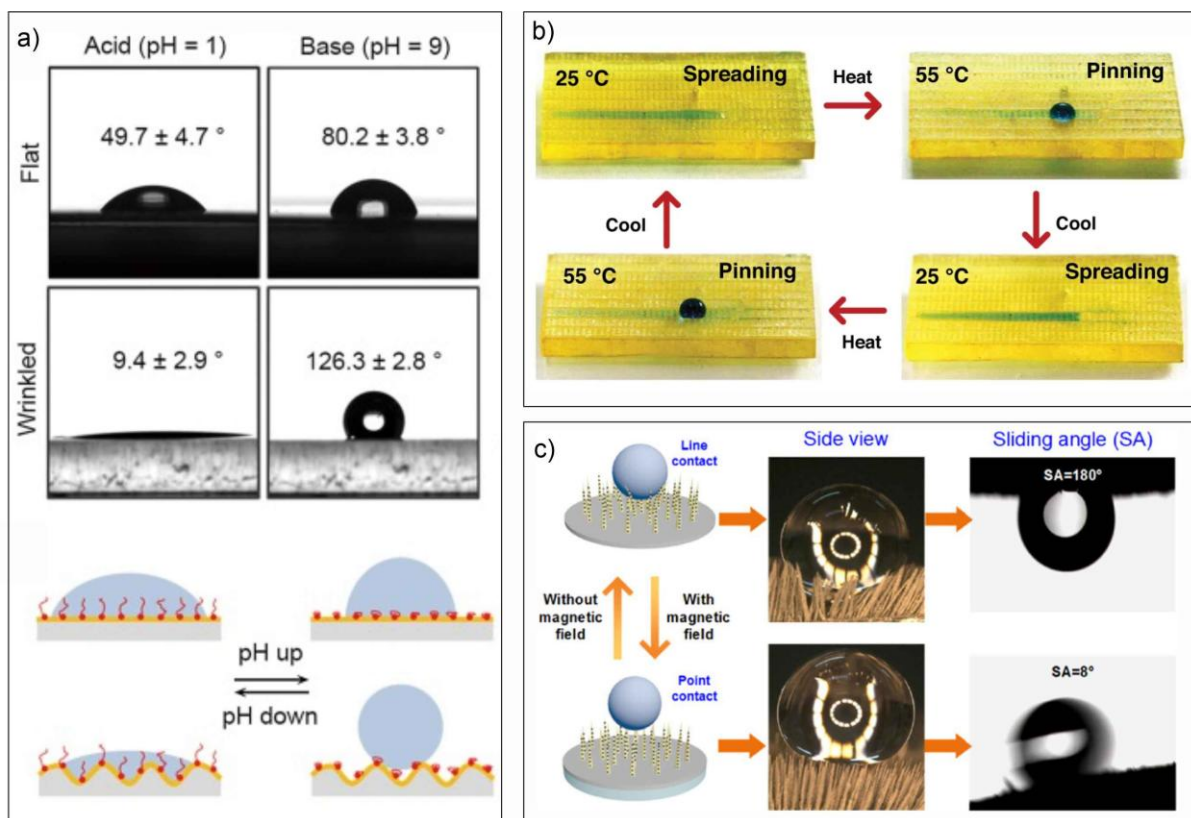
Figure 9. Switchable wettability of smart surfaces driven by different stimuli, **a)** pH-responsive surface.[55] [Reproduced with permission from [55]. Copyright © 2020 Elsevier B.V. All rights reserved] **b)** Thermoresponsive topographical surface,[56] and **c)** magnetic responsive fibrillar surface.[57] [Reproduced with permission from [57]. Copyrights © 2018 American Chemical Society].

1.4.1. Smart materials

Fabrication of these smart surfaces with switchable wettability requires proper materials that can present different changes either in their chemistry or their physical properties. Smart materials or shape-changing materials are the ones that are able to transform their shape through the application of an external stimulus. The name smart is used because these materials have the ability to sense the environment and surroundings and respond to them.[58] The advantage of using responsive materials is the capability to have external control. Several stimuli are used to possess total control of the object.

Smart materials can be classified as passive or active. Passive smart materials transfer a type of energy, for example, the optic fibers that transfer electromagnetic waves. Active materials are divided into two: (i) materials that do not change their properties after stimuli exposure, and (ii) materials that transform one type of energy into another. The materials that can transform energy into other types bring the attention of researchers because their actuation will depend on the applied stimulus. Between the properties that characterize the active materials, there are (i) transiency, (ii) immediacy, (iii) selectivity, (iv) shape-changing, and (v) self-healing.[59]

Among the smart materials commonly used, one can find diverse types like piezoelectric materials that convert mechanical energy into electric energy or vice versa. Smart chromoactive materials change their color after stimuli exposure. Magnetorheological materials change their rheological properties when exposed to magnetic fields. Shape memory materials, which can change their shape and return to the original state when they are exposed to heat or other stimuli.[59]

1.4.2. Shape memory polymers

Shape memory polymers (SMPs) are polymer networks that can be fixed in a transitory state. SMPs are widely used due to their advantages as lightweight, versatility, customized, low cost, easy processing, and biocompatibility. SMPs commonly use heat as a stimulus for shape transformation, which is why they are known as thermoresponsive polymers. When the SMPs are heated over the transition point, they behave as elastomers and are soft. SMPs act like "regular" polymers in the frozen state, below the glass transition point,[60] which means that in the frozen state, the polymer does not have special properties of SMPs, and maintains a fixed shape.

Actuation of thermoresponsive polymers requires thermal energy to melt the crystalline sections of the polymer (**Figure 10**). The heating can be direct or indirect like photothermal heating. Direct heating causes the crystalline parts of the polymer to transform into amorphous polymer chains, allowing the mobility of the fibers. The temperature must be higher than the transition temperature (T_{trans}). T_{trans} depends on the polymer structure, T_{trans} can be the glass transition temperature (T_g) for the amorphous polymers, or the melting point (T_m) for

semicrystalline polymers, copolymers, and crosslinked ones.[61] (i) First one involves the mechanical deformation of the SMPs which are based on the transition form to rubber state, where the material is highly elastic and low stress can deform the shape (**Figure 10a, b**). When the temperature is lower than T_{trans}, the polymer goes from a glassy state to a rubbery state. At the glassy state, Young's modulus is higher, and the strength of the material is higher too, and after the addition of energy, the modulus decreases, facilitating the deformation of the material. (ii) The second one is the storage property of the programmed deformation (**Figure 10c**). Depending on the temperature of the material, the deformation can be "saved" or released. SMPs preserve the temporarily deformed shape in a stress-free state. (iii) The third point is the recovery state of the original shape after the elimination of the external stress and in the presence of the stimuli (**Figure 10d**). [62]
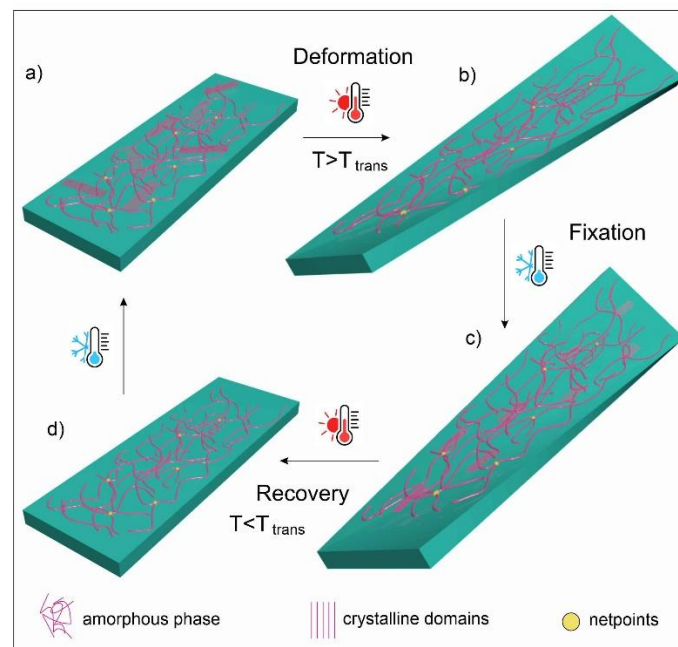
Figure 10. Shape memory thermoresponsive actuation of polymers: **a)** semicrystalline polymer can be deformed **b)** by melting the crystalline phase of the polymer chains by increasing the temperature over the transition temperature. By fast cooling, while applying the deformation stress, **c)** the polymer chains crystallize fixating the temporal shape. The recovery to the original state involves the melting of the temporary fixed crystalline phase to the amorphous phase to return to **d)** the original state and cooling of the material leads to the formation of crystalline parts **(a).**

1.4.3. Thermodynamics of shape memory effect (SME)

The shape memory effect (SME) of polymers involves thermodynamical changes. SME comes from the ability to have different conformations of the polymer chains, which are reversible. The thermodynamic changes during each phase are described next:

Deformation of the SME: the heating of amorphous polymers above their T_g increases the enthalpy, allowing the polymer chains to become more mobile. This leads to highly coiled amorphous polymer chains with high entropy, as described by Boltzmann's equation:

$$S = k \ln W$$

Equation 9

Where S is the entropy, k is the Boltzmann's constant, and W is the number of accessible microstates of a system.

Fixation of the SME: During the transition to a deformed state, the stress applied to the material leads to a decrease in the entropy of the system producing aligned and organized polymer chains. The deformation step requires an input of energy as mechanical work. The energy is absorbed by the material and stored in the polymer chains. The amount of energy absorbed during deformation depends on factors such as the applied stress, deformation rate, and polymer properties.

Recovery of the SME: During the recovery of the original state of the polymer, the release of the applied stress and stored energy when the temperature is higher than T_{trans}, produces that the polymer chains restore their random coil conformation. This process is accompanied by an increase in entropy, which leads to the recovery of the original shape of the material.[63] The addition of energy by heating the deformed polymer above its T_{trans} provides the necessary thermal energy to overcome the energy barrier (activation energy) and allow the polymer chains to relax back to their original configuration.[64]

1.4.4. Thermoplastic polyurethane

Polyurethanes are versatile copolymers that are widely used for their abrasion and tear resistance, tensile and compression strength, and hardness, created in replacement of natural rubber. They are commonly used for coatings, construction foams as insulating material, packaging,[65] and as well as biomedical materials in catheters, wound dressings, and short-term implants.[66]

Polyurethanes are the result of the reaction of isocyanates and polyols. The reaction between the alcohol group (-OH) and the isocyanate (NCO) forms the urethane group (-NH-CO-O-) also known as carbamate. These two segments define the final properties of the polyurethane allowing the manufacturer to customize the polyurethane to several applications. The soft segment (SS) composed of the polyol presents better mobility due to its long chain length. The polyol also provides flexibility to the polyurethane – longer chain length, higher flexibility. While the hard segment (HS) is formed by the linkage between the isocyanates and the chain extender. The isocyanates are short molecules that can organize in a crystal lattice, which makes the polyurethane hard and non-flexible.[65] The glass transition (T_g) of SS usually is below room temperature and the T_g of HS is above the ambient temperature. The formation of H-bonds of the HS is the reason for the increase of energy in order to break those linkages, allowing the polyurethane to melt in comparison to other similar esters. The energy that the H-bond has can be between 20-50 kJ/mol. The amine group (N-H) is the proton donor and the carbonyl group (C=O) acts as a proton acceptor. Another potential proton acceptor is the alkoxy oxygen (-O-) from the urethane bond.[67]

Among the polyurethanes, elastomers exhibit high elasticity. Elastomers can be stretched to several times their original length without breaking. This is mainly explained by the long chain segment of the SS (polyol), while the HS brings more stability and strength to the material due to its performance as a physical crosslinking points. The physical crosslinking is formed by hydrogen bonding, polar interactions, or crystallization.[68] This characteristic of the HS allows it to restore the shape and avoid permanent deformation, it can withstand moderate deformation under external load. The SS formed by long aliphatic polymer chains is able to stretch and uncoil providing high elasticity. Nevertheless, the physical crosslinking can present creep behavior, which can alter the shape recovery. In contrast, chemical crosslinking can lead to a high deformation degree because the molecular chains do not slip between each other.

In **Figure 11,** the synthesis route for poly(1,4-butylene adipate)-based polyurethane (PU-PBA) is presented. For SS, polybutylene adipate (PBA) is used. PBA is also known as adipic acid-1,4-butanediol copolymer or poly(tetramethylene adipate). The HS is composed of 4,4'-diphenylmethane diisocyanate also known as methylene diphenyl diisocyanate (MDI) and butane diol (BD) as chain extender. The crosslinking effect of the HS on the SS prevents the viscous flow above the PBA melting transition.[69] The shape memory properties of the PU-PBA are based on the SS. The temperatures of crystallization and melting of PBA define the SME of the whole copolymer.
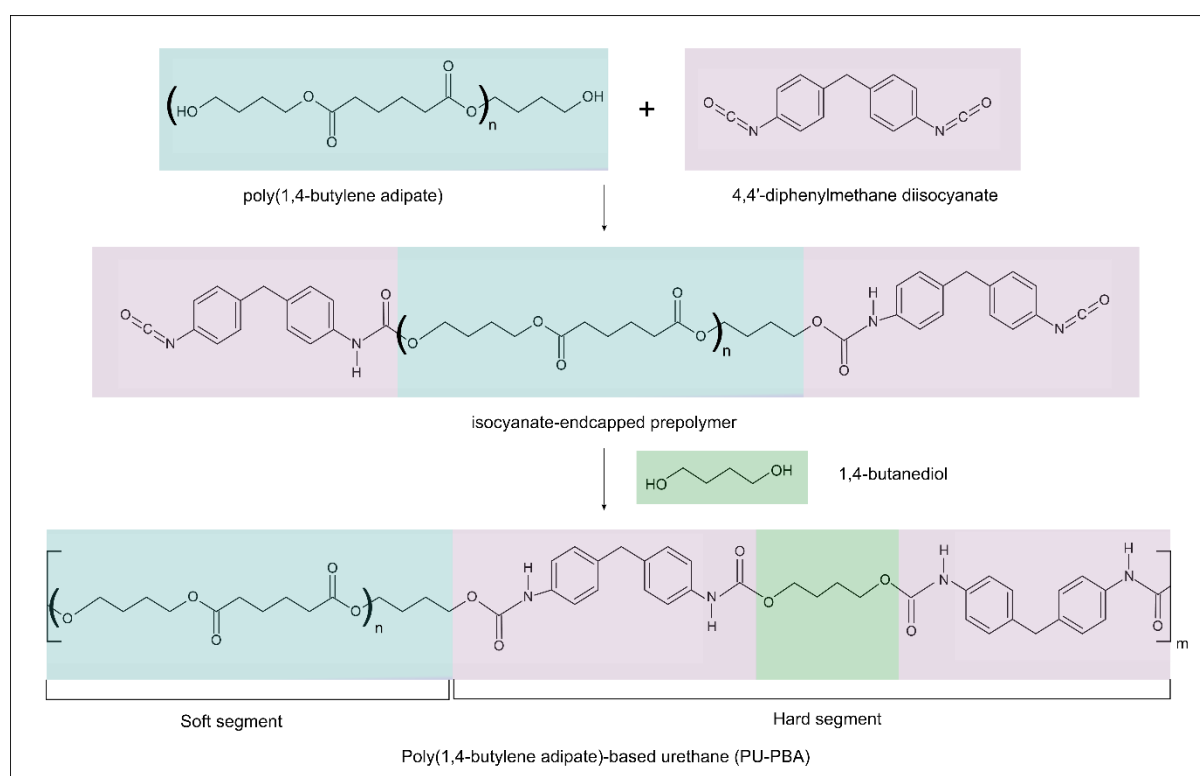
Figure 11. Synthesis schema of poly(1,4-butylene adipate)-based polyurethane (PU-PBA)

1.5. Fabrication techniques for smart surfaces

Topographical design of the surface, desired functionality, and choice of material influence deeply in the selection of the fabrication method of such surfaces. Especially the fabrication of micro and nano-structured surfaces requires techniques with high resolution like photolithography and stereolithography. Additive manufacturing enables the direct printing of

functional materials onto substrates, allowing for rapid prototyping and customization of structured surfaces for diverse applications ranging from microfluidics to tissue engineering.

Nevertheless a currently problematic is the limited amount of available materials that can be used in additive technologies. To overcome this issue, rapid prototyping is mostly used to create molds, that can be further used for casting other materials to produce the smart surfaces by replica-molding process. Overall, the integration of 3D printing with smart surfaces opens up a wide range of innovative applications across industries, driving advancements in functionality, customization, and sustainability. An investigation carried out by Wang and collaborators showed the fabrication of switchable hydrophobicity of a surface driven by a pneumatic system. Inflation and deflation of micro-air-sac network structure to produce different wetting states: rose-petal and lotus-effect (**Figure 12a**).[70] Replica-molding process also is used in combination with thermoresponsive polymers, as in the research presented by Zhang, et al. A surface with both surface chemistry and surface topography was fabricated to have precise wetting and their gradients. The SMP was cast on a mold created by photolithography and then grafted with PNIPAAm[71] (**Figure 12b**).
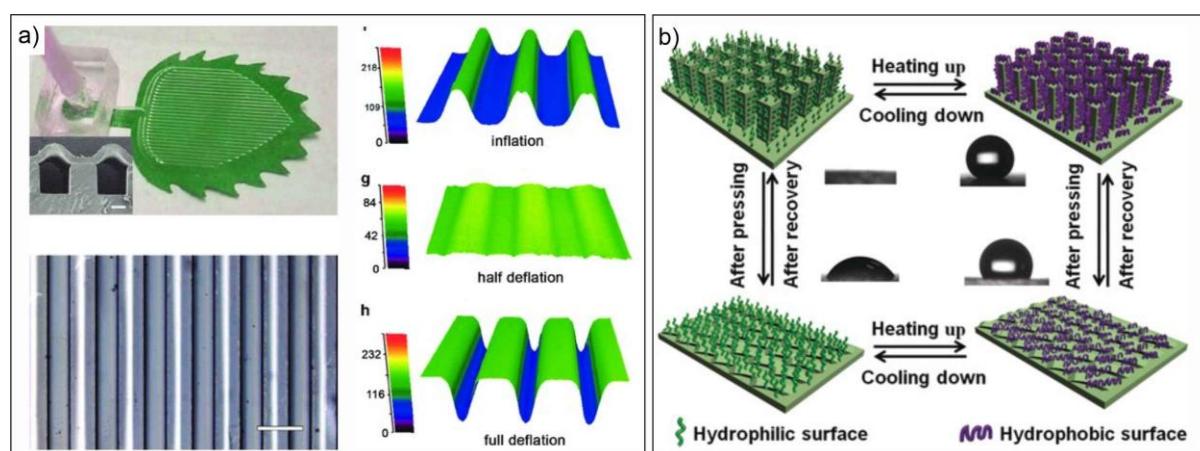
Figure 12. Smart surfaces produced by replica molding technique. **a)** pneumatic mechanism for switchable wettability,[70] [Reproduced with permission from [70]. Copyright © 2018, The Authors. Licensed by CC-BY] and **b)** thermoresponsive surface by switching chemistry and topography.[71] [Reproduced with permission from [71]. Copyright © 2018 Wiley-VCH Verlag GmbH & Co. KGaA, Weinheim]

These approaches require multiple steps during processing and toxic chemicals for fabrication. 3D printing of thermoplastic for smart surface fabrication is an alternative for building structures with higher dimensions hundreds of micrometers up to millimeters and

more. The low resolution of this technology linked to the diameter size of the nozzles is a problem in constructing micro and nano-structured surfaces. A potential alternative is the combination of 3D printing with other technologies to reduce the diameter of fibers. Under this statement, electrospinning and melt-electrospinning allow the thinning of the fibers from micrometers to nanometer scale. The thinning happens due to the electrical forces between the needle and metallic collector, which pulls the fiber and stretches the polymer until deposition. The combination of electrospinning with additive manufacturing results in the emergence of a novel technology known as melt electrowriting.

1.5.1. Melt electrowriting of SMPs

Melt electrowriting (MEW) is an innovative additive manufacturing technique that enables the precise deposition of microscale fibers through the application of an electric field. This process has gained significant attention in the fields of tissue engineering,[72-74] and advanced materials[75, 76] science due to its ability to fabricate complex structures with tailored properties.

MEW fundamentally is the combination of 3D printing and electrospinning process. The principle of MEW relies on the thinning of the fiber. The polymer or composite material is heated to its melting point and then dispensed through a fine metallic nozzle (**Figure 13a**). Simultaneously, an electric field is applied to the material, firstly causing the formation of a Taylor cone to reduce the diameter of the extruded fiber. The electrical field draws the fiber towards a grounded collector substrate. As the printhead moves along the surface, the fiber presents delayed deposition on the collector (**Figure 13b**). The material solidifies upon deposition. 3-dimensional structures are formed layer by layer with high precision and resolution.
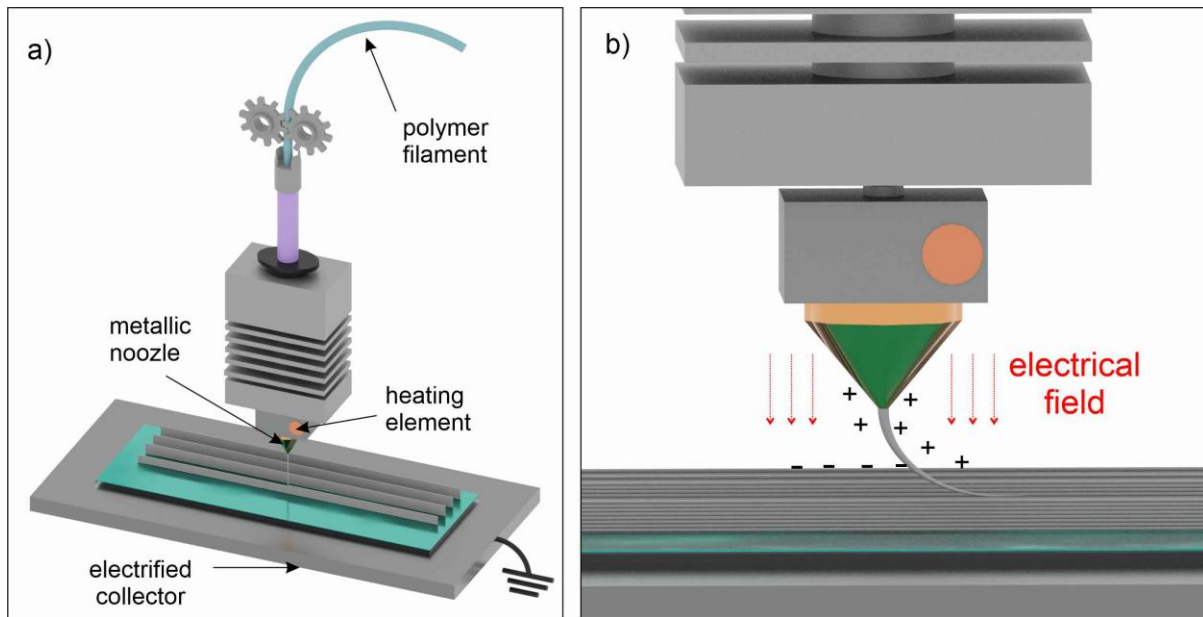
Figure 13. Melt electrowriting technology **a)** adapted from a fused filament feeding printer, and **b)** Taylor cone formation for thinning the fiber by the effect of the electrical field

Moreover, melt electrowriting offers versatility in terms of materials that can be used. A wide range of polymers, including biocompatible and biodegradable polymers such as polycaprolactone (PCL), poly(lactic-co-glycolic acid) (PLGA), and poly(ethylene glycol) (PEG), and even liquid crystal elastomers can be processed using this technique. Melt electrowriting represents a promising approach for the precise fabrication of micro-structured surfaces with a variety of materials.

1.6. Conclusion

Bioinspiration draws upon nature's designs, mechanisms, and systems to inspire innovation in various fields. From mimicking the structure of a lotus leaf for water-repellent surfaces to modeling robotic movements after animal locomotion, nature is constantly providing creative solutions to all types of problems. Bioinspiration as an interdisciplinary approach not only has a great impact on technology development but also raises sustainable and efficient designs. After detailed investigations, now it is widely known that the wetting of surfaces is explained by the interplay of surface topography and chemistry. The increase of the roughness in the surface topography converts hydrophilic surfaces into more hydrophilic, and hydrophobic into superhydrophobic surfaces as in the lotus leaf. While the surface chemistry produces total spreading of the water drop or complete rolling due to the superhydrophobic effect.

The development of new surfaces and technologies is dependent on the understanding of these surfaces. The estimation and prediction of the behavior of the droplets have been made through mathematical modeling between the interaction of droplet water and the solid surface like Young's model for smooth surfaces, and Wenzel's and Cassie-Baxter's model for rough surfaces. Starting from these equations, additional derivations can predict the wetting of the surface by obtaining the contact angle. The effect of water is not limited to the wetting state of the surface, but also to the folding of thin films into more complex structures by elastocapillarity forces.

Nowadays, the introduction of smart materials has broadened the possible applications in the field of materials science for switchable surfaces. This shape-changing of the smart surfaces relies on materials capable of altering their chemistry or physical properties. The smart materials can alter their surface leading to a change in the wetting state. The control on the shape-changing surface allows the control over their wetting behavior. The fabrication method for smart topographical surfaces commonly used in investigation involves replica molding processes. The molds are generated through rapid prototyping, which makes replica molding a complicated method, time-consuming, and also involves toxic reagents. Fabrication of small structures is feasible due to its high-resolution printing capabilities. Typically, these surfaces have a low aspect ratio (max 2:1), and require manual deformation for actuation studies, where external force is applied to change the topography.

Conventional three-dimensional printers as filament-fused fabrication are advantageous in contrast to SLA printing, mainly due to the material availability. The object can be directly produced but their smallest dimensions are limited to the size of the inner diameter of the needles during extrusion, which affects the resolution of the printed objects. 3D printing of shape-changing materials is interesting due to their versatility and easy processing. Thermoresponsive surfaces can undergo reversible phase transitions, allowing them to deform and recover their original shape.

An alternative fabrication approach that prevents the use of sacrificial materials and molds while maintaining high resolution for micrometric surfaces is melt-electrowriting technology. This method utilizes thermoplastics as the thermoresponsive polyurethanes that are extruded through a needle. Due to the electrical forces, the fiber diameter decreases significantly, resulting in the production of micrometric fibers. Through controlled deposition, a structured surface is formed.

The investigation of wetting of high aspect ratio surfaces that present a shape-changing effect needs to be further investigated. The modification of the topography of the smart surfaces due to water dynamics will provide valuable information to understand the behavior of smart surfaces and the creation of smart devices and microfluidic-controlled devices.

2.   Aim

This thesis aims to investigate the behavior of structured shape-changing surfaces with a high aspect ratio in response to water dynamics. The high aspect ratio of the lamellar surface plays an important role in the degree of deflection of the lamellae under external forces. Lamellae that are both high and thin, with a low elastic modulus, are more prone to bending when a droplet increases or decreases in volume. In this research, the deflation and inflation of water droplets cause the lamellae to collapse or separate, respectively. By examining the mechanical properties of the material at various temperatures, one can manipulate the behavior of these structured surfaces. It is important to study the effect of each factor that interplays in the characterization of these switchable surfaces, separately and together:

(i)   the mechanical properties and actuation properties,

(ii)   surface tension,

(iii)   the topographical surface.

To achieve this purpose, the subsequent objectives that involve the selection of material, fabrication methodology, and actuation tests are pursued during this investigation:

Objective 1: The first objective addresses developing a fabrication methodology of high-aspect-ratio lamellar surfaces with shape-changing properties. To achieve this objective a shape memory polymer with low elastic modulus and 3D printing processable properties is needed. The polymer must flow on printing temperatures and must possess transition temperatures in normal conditions. The polymer must be processable by melt-electrowriting technique to produce micrometric fibers and provide proper stacking to construct a high aspect ratio lamellar surface.

Objective 2: The second objective aims to elucidate the effect of water droplet dynamics (inflation and deflation) on the tunability of the topographical surface. This effect together with the response to the external stimuli can be used to control the deformation of surfaces.

Objective 3: The third objective is related to the potential application of these structured surfaces for constructing smart devices utilizing shape-changing materials and surface manipulation techniques.

3. Synopsis

In this dissertation, stimuli-responsive lamellar surfaces are used as a basis for deformation studies. This thesis focuses primarily on the modification of tunable topographical structures interaction of water droplets. This study investigates the possibility of modifying its topography by changing its mechanical properties. This information is deeply explained in three peer-reviewed publications, all of them as first author. Of these research articles, two are published (Publication 1, Publication 2) and one is submitted (Publication 3) (*Langmuir*).

My investigation is based on the analysis of the effect of the mechanical and actuation properties of thermoresponsive polymer on the switching of surface topography upon the exhibition of external stimuli and stress. In this case, the structured surface is modified when the surface tension forces are much stronger than the elastic forces of the material. Surface tension forces are sufficient to deform the surface when the material has a low modulus. The switching of the material's mechanical properties based on temperature is investigated in detail in the publications. In Publication 1, we investigated the effect of temperature: thermosetting polyurethane can change its modulus of elasticity at a given temperature, affecting the flexural behavior of long walls. In Publication 2, we advanced into the investigation of photothermal stimuli. This technique thermal and photothermal stimulation was used for the development of smart devices, like valves, that can shift the topography of the surface by the presence of water in the surface. Publication 3 provides an insight into cantilever-like lamellae, where only one section is fixed to a substrate, while the other section remains non-adhered. Overall, this research explores the effect of wettability on shape-changing lamellae surfaces with thermoresponsive properties, the analysis of the exerted forces on the surface, and its potential application for smart devices and self-folding structures.

## 3.1. Smart Mechanically Tunable Surfaces With Shape Memory Behavior And Wetting-Programmable Topography

This study examines innovative fabrication and properties of high-aspect-ratio lamellar surfaces using shape-memory polymers. These polymers exhibit tunable mechanical properties, crucial for controlling the wetting behavior of the structured surfaces. In this study, we introduced, for the first time, the fabrication of lamellae with a very high aspect ratio, allowing for pronounced and controllable deformation of the surface structures by external stimuli like temperature. The shape-memory behavior of the polymer enables it to switch between soft and hard states depending on the temperature, significantly influencing the surface's wettability. When heated or cooled, the lamellae become more deformable, affecting how easily the surfaces can be wetted (**Figure 14**). This tunable wettability is important for applications requiring precise fluid interaction control.
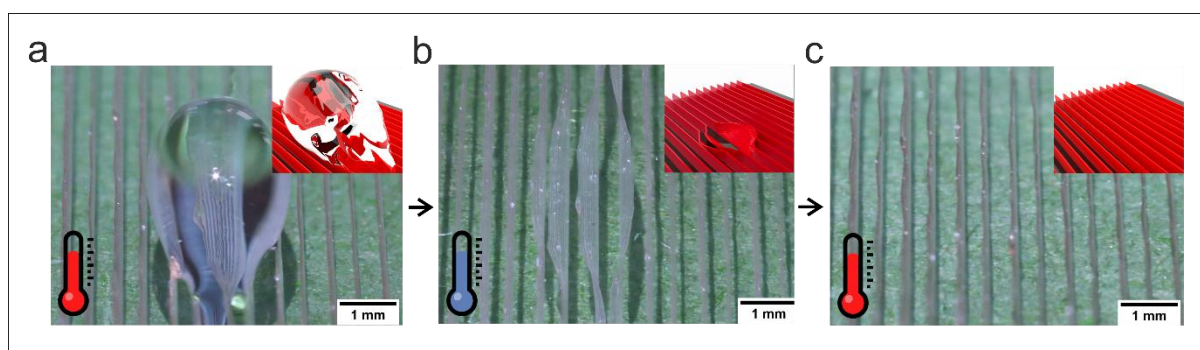
Figure 14. Actuation of the smart lamellar surface from **a)** bending of the lamellae by water drop, **b)** fixation of the deformed surface by lowering the temperature, and **c)** recovery of the original state of the surface. [Reprinted with permission from [77]. Copyright © 2022, American Chemical Society]

The thermoresponsive poly(1,4-butylene adipate)-based polyurethane (PU-PBA) was used for fabricating the high aspect ratio lamellae (**Figure 15a and b**). Through melt-electrowriting, fibers were fabricated in the micrometer range (**Figure 15c**), and by stacking, the height of the lamellae was up to 50 times higher than its thickness (**Figure 15b**). The high aspect ratio in combination with the mechanical properties of the material is responsible for the bending of the walls. The elastic modulus of the polymer was measured at different temperatures (**Figure 15d**) when the soft segment was crystallized (4°C) and after its melting (40°C). It is noticeable that the elastic modulus decreases more than 5 times, converting the

lamellae to a soft state. The correlation between the temperature, mechanical properties, and wettability are analyzed in detail in this publication.
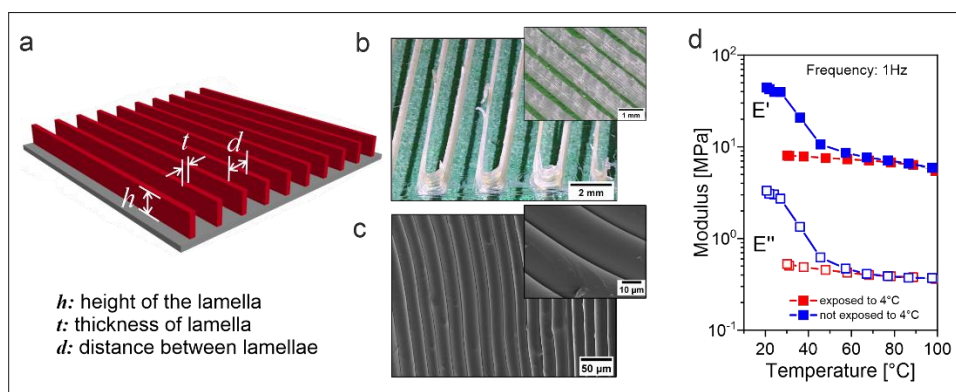

Figure 15. a) Schema of the smart lamellar surfaces, **b)** Top and lateral view images of the fabricated structured, and **c)** the SEM of the stacked fibers. **d)** presents the elastic and loss modulus at different temperatures when the polymeric lamellae is exposed and not exposed to 4 °C. [Reprinted with permission from [77]. Copyright © 2022, American Chemical Society]

The study emphasizes potential applications in microfluidic devices, highlighting that these smart surfaces can create thermally controlled smart valves.

3.2. Reversibly Photoswitchable High-Aspect Ratio Surfaces

Traditional shape-memory polymers (SMPs) usually allow one-way shape transformation, requiring manual deformation to achieve a temporary shape. These polymers are generally thermoresponsive. The actuation of SMPs can be enhanced through localized heating. Light-responsive materials enable local heating, remote activation, and rapid switching via photothermal effects. This research article reports the fabrication of photothermal responsive high-aspect ratio surfaces with switchable topography of shape-memory polymers and deposition of light-to-heat converting black ink via dip coating (**Figure 16a-d**). The reversible nature of the deformation process ensures that the surfaces can be used repeatedly without significant degradation of their properties.

The mechanical properties of the polymer changed significantly upon exposure to light (**Figure 16e**). The localized heating caused the soft segments (PBA) of the SMP to approach their melting temperature, leading to softening of the material. The transition from a rigid to a soft state was critical for enabling deformation by external forces, such as water droplets. Upon exposure to low temperatures, the lamellae remain hard and non-deformable by water droplets. Illumination raises the temperature close to the melting point of the polymer's soft segment, leading to softening and enabling local deformation by water droplets. Cooling fixes the deformed state, allowing reversible local deformation.
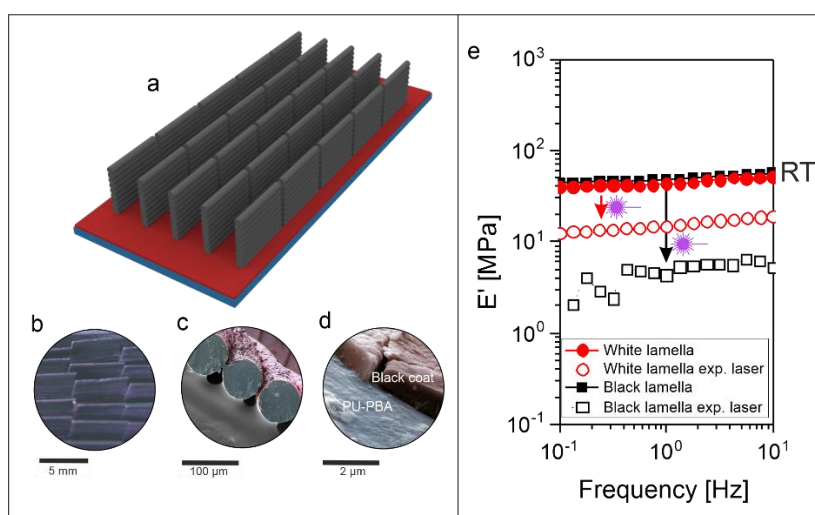
Figure 16. a) Schema and **b)** optical image of the lamellar surface coated with black ink, **c)** and **d)** SEM imaging of the black coating and its thickness. **e)** Elastic modulus of the black lamella when exposed to laser for photothermal effect on coated and non-coated lamellae.[78]

In microfluidic devices, the light-induced deformation and subsequent recovery of the lamellae allowed for the creation of smart valves (**Figure 17**). These valves could open and close in response to light, controlling the flow and mixing of fluids with high precision.
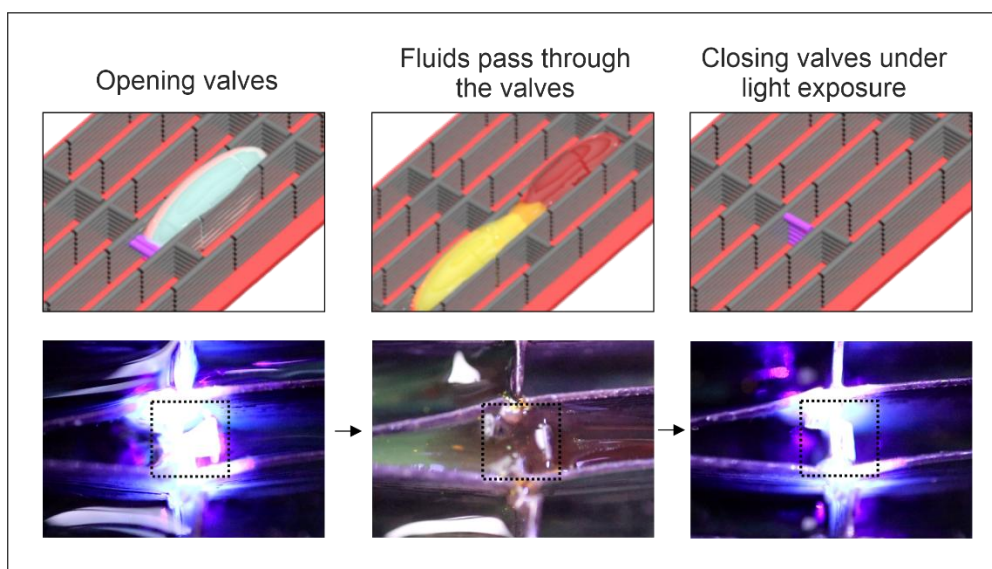

Figure 17. Bending of smart valves is controlled by local illumination, allowing the combination of fluids.[78] [Reproduced with permission from [78]. Copyright © 2023 The Authors. Small Structures published by Wiley-VCH GmbH].

3.3. Switchable Elastocapillarity of High-Aspect-Ratio Topographically Structured Surfaces

The paper explores elastocapillarity, the interaction between elasticity and capillarity, within the context of smart surfaces. This phenomenon is critical for various applications, including microfluidics, biotechnology, robotics, and medicine. The study focuses on the elastocapillarity of partially cantilever-like lamellae with switchable mechanical properties. Free-standing lamellae were fabricated using contrasting polymer coatings and their sliding behavior was analyzed.

The study used a shape-memory poly(1,4-butylene adipate)-based polyurethane (PU-PBA) for fabricating free-standing lamellae. Various polymer coatings, including poly-lactide (PLA) and polydimethylsiloxane (PDMS), were applied to control adhesion properties. The substrates were prepared through spin-coating and dip-coating techniques. Melt-electrowriting (MEW) was employed to fabricate the lamellae, and their mechanical properties were analyzed under different conditions.

The sliding behavior of water droplets on the structured surfaces was influenced by the substrate properties (**Figure 18**). The water acted as a lubricant, reducing frictional forces and facilitating droplet movement. Deformation studies showed temperature-dependent behaviors, with pronounced bending observed at higher temperatures. Recovery of deformation highlighted the role of capillary forces and lateral adhesion. On PDMS surfaces, stronger friction forces hindered significant movement, emphasizing the importance of surface properties in determining elastocapillarity. The study highlights the significant role of capillary forces and lateral adhesion in the dynamic interactions on these surfaces, providing valuable insights for applications in soft robotics.
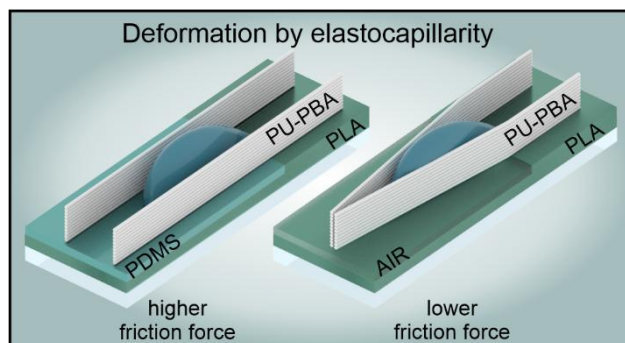
Figure 18. Collapsing of free-standing lamellae on substrates with different friction coefficient[79]. [Reprinted with permission from[79] Constante, G.; Schönfeld, D.; Pretsch, T.; Milkin, P.; Sadilov, I.; Ionov, L. *Langmuir* 2025, ASAP. DOI: 10.1021/acs.langmuir.5c02002. Copyright © 2025, American Chemical Society]

4.   Conclusion

This investigation has demonstrated the significant impact of mechanical and actuation properties of thermoresponsive polymers on the switching of surface topography under external stimuli and stress. Smart topographically lamellar surfaces are characterized by the deflection of the lamellae when the material exhibits a low modulus. The influence of mechanical properties, as they change with temperature, has been meticulously analyzed across the presented publications.

Publication 1 focused on the effect of temperature on thermoresponsive SMP. The study showed that modifying the modulus of the polymer by setting the temperature could control the bending curvature of long walls.

Publication 2 advanced the investigation to photothermal stimuli. Light-responsive lamellae enabled precise, localized heating and subsequent control of surface bending. This method allowed for the development of smart devices such as valves that could shift the surface topography in response to the presence of water.

Publication 3 explored cantilever-like lamellae with sections fixed to different substrates, analyzing the interaction between lamellae and substrates of varying hydrophilicity. The study emphasized the role of different moduli and surface interactions in determining elastocapillarity. The findings highlighted how capillary forces and lateral adhesion significantly influence the dynamic interactions and deformation behaviors of these surfaces.

Overall, this body of research delves into the effect of wettability on shape-changing lamellae surfaces with thermoresponsive properties. It showcases their potential applications in smart devices and self-folding structures. The ability to switch between soft and hard states, coupled with shape memory effects, enables reversible and localized deformation. This versatility is crucial for practical implementations in microfluidics, soft robotics, and other advanced technological applications.

5. Outlook

In future research, several key directions can be explored to further understand and enhance the tunable mechanical properties and applications of lamellar surfaces. Establishing collaborations to develop a mathematical model that accurately represents the tunable mechanical properties of the lamellar surface is essential. This model should consider key variables like the elastic modulus of the material, dimensions, and external forces. By doing so, the behavior of these surfaces can be predicted and optimized according to the application.

To enhance the functionality of these lamellar surfaces, we can explore combining them with other materials to create two- or three-way shape memory polymers. This integration could provide multi-responsive properties, enabling the surfaces to switch between different states or shapes.

Moreover, the transportation of single droplets along the surface through the movement of specific lamellae can be investigated, which expands the possible applications in microfluidics and lab-on-a-chip devices. Precise manipulation of fluids requires an understanding of the mechanisms for droplet movement.

Addressing these areas will enhance the understanding and capabilities of smart lamellar surfaces, opening the door to innovative applications in various fields such as soft robotics, biotechnology, and advanced manufacturing.

6.   References

1.   Endler, J. A.; McLellan, T., The Processes of Evolution: Toward a Newer Synthesis. *Annual Review of Ecology and Systematics* **1988,** *19*, 395-421.

2.   Brown, W. L., Jr., General Adaptation and Evolution. *Systematic Biology* **1958,** *7* (4), 157-168.

3.   Introduction: Bioinspired and Biomimetic Materials. *Chemical Reviews* **2017,** *117* (20), 12581-12583.

4.   Cheng, Y.-T.; Rodak, D. E., Is the lotus leaf superhydrophobic? *Applied Physics Letters* **2005,** *86* (14), 144101.

5.   Farzam, M.; Beitollahpoor, M.; Solomon, S. E.; Ashbaugh, H. S.; Pesika, N. S. Advances in the Fabrication and Characterization of Superhydrophobic Surfaces Inspired by the Lotus Leaf *Biomimetics* [Online], 2022.

6.   Ghasemlou, M.; Le, P. H.; Daver, F.; Murdoch, B. J.; Ivanova, E. P.; Adhikari, B., Robust and Eco-Friendly Superhydrophobic Starch Nanohybrid Materials with Engineered Lotus Leaf Mimetic Multiscale Hierarchical Structures. *ACS Applied Materials & Interfaces* **2021,** *13* (30), 36558-36573.

7.   Cheng, Y. T.; Rodak, D. E.; Wong, C. A.; Hayden, C. A., Effects of micro- and nano-structures on the self-cleaning behaviour of lotus leaves. *Nanotechnology* **2006,** *17* (5), 1359.

8.   Ensikat, H. J.; Ditsche-Kuru, P.; Neinhuis, C.; Barthlott, W., Superhydrophobicity in perfection: the outstanding properties of the lotus leaf. *Beilstein Journal of Nanotechnology* **2011,** *2*, 152-161.

9.   Song, S.; Drotlef, D.-M.; Majidi, C.; Sitti, M., Controllable load sharing for soft adhesive interfaces on three-dimensional surfaces. *Proceedings of the National Academy of Sciences* **2017,** *114* (22), E4344-E4353.

10.   Tian, Y., Gecko Toe Surface. In *Encyclopedia of Tribology*, Wang, Q. J.; Chung, Y.-W., Eds. Springer US: Boston, MA, 2013; pp 1530-1533.

11.   Gandyra, D.; Walheim, S.; Gorb, S.; Ditsche, P.; Barthlott, W.; Schimmel, T., Air Retention under Water by the Floating Fern Salvinia: The Crucial Role of a Trapped Air Layer as a Pneumatic Spring. *Small* **2020,** *16* (42), 2003425.

12.   Bing, W.; Wang, H.; Tian, L.; Zhao, J.; Jin, H.; Du, W.; Ren, L., Small Structure, Large Effect: Functional Surfaces Inspired by Salvinia Leaves. *Small Structures* **2021,** *2* (9), 2100079.

13.   AirCoat Bioinspired technology: air layer laminate composition. https://aircoat.eu/project/.

14.   Xu, C.; Feng, R.; Song, F.; Wang, X.-L.; Wang, Y.-Z., Desert Beetle-Inspired Superhydrophilic/Superhydrophobic Patterned Cellulose Film with Efficient Water Collection and Antibacterial Performance. *ACS Sustainable Chemistry & Engineering* **2018,** *6* (11), 14679-14684.

15.   Yu, Z.; Zhang, H.; Huang, J.; Li, S.; Zhang, S.; Cheng, Y.; Mao, J.; Dong, X.; Gao, S.; Wang, S.; Chen, Z.; Jiang, Y.; Lai, Y., Namib desert beetle inspired special patterned fabric with programmable and gradient wettability for efficient fog harvesting. *Journal of Materials Science & Technology* **2021,** *61*, 85-92.

16.   Klemm, O.; Schemenauer, R. S.; Lummerich, A.; Cereceda, P.; Marzol, V.; Corell, D.; van Heerden, J.; Reinhard, D.; Gherezghiher, T.; Olivier, J.; Osses, P.; Sarsour, J.; Frost, E.; Estrela, M. J.; Valiente, J. A.; Fessehaye, G. M., Fog as a Fresh-Water Resource: Overview and Perspectives. *AMBIO* **2012,** *41* (3), 221-234.

17.   Lu, Y.; Sathasivam, S.; Song, J.; Crick, C. R.; Carmalt, C. J.; Parkin, I. P., Robust self-cleaning surfaces that function when exposed to either air or oil. *Science* **2015,** *347* (6226), 1132-1135.

18.   Edupic Lotus leaf. https://naturesraincoats.com/lotus-leaf/ (accessed 25th January).

19.   Autumn, K.; Sitti, M.; Peattie, A.; Hansen, W.; Sponberg, S.; Liang, Y. A.; Kenny, T.; Fearing, R.; Israelachvili, J.; Full, R. J., Evidence for van der Waals adhesion in gecko setae. *Proceedings of the National Academy of Sciences USA* **2002,** *99*, 5.

20.   Autumn, K.; Majidi, C.; Groff, R. E.; Dittmore, A.; Fearing, R., Effective elastic modulus of isolated gecko setal arrays. *Journal of Experimental Biology* **2006,** *209* (18), 3558-3568.

21.   Barthlott, W.; Schimmel, T.; Wiersch, S.; Koch, K.; Brede, M.; Barczewski, M.; Walheim, S.; Weis, A.; Kaltenmaier, A.; Leder, A.; Bohn, H. F., The Salvinia Paradox: Superhydrophobic Surfaces with Hydrophilic Pins for Air Retention Under Water. *Advanced Materials* **2010,** *22* (21), 2325-2328.

22.   Stueber, K. Salvinia natans. www.biolib.de.

23.   Osterath, B., Why life thrives in the foggy Namib desert. *Deutsche Welle* 2017.

24.   Parker, A. R.; Lawrence, C. R., Water capture by a desert beetle. *Nature* **2001,** *414* (6859), 33-34.

25.		Chen, L.; Li, X., Chapter 4 - Sodium battery nanomaterials. In *Advanced Nanomaterials for Electrochemical-Based Energy Conversion and Storage*, Ran, F.; Chen, S., Eds. Elsevier: 2020; pp 115-160.

26.		Abraham, M.; Claudio, D. V.; Stefano, S.; Alidad, A.; W., D. J., Contact angles and wettability: towards common and accurate terminology. *Surface Innovations* **2017,** *5* (1), 3-8.

27.		Lößlein, S. M.; Mücklich, F.; Grützmacher, P. G., Topography versus chemistry – How can we control surface wetting? *Journal of Colloid and Interface Science* **2022,** *609*, 645-656.

28.		Bayer, I. S., Superhydrophobic Coatings from Ecofriendly Materials and Processes: A Review. *Advanced Materials Interfaces* **2020,** *7* (13), 2000095.

29.		Shuttleworth, R., The Surface Tension of Solids. *Proceedings of the Physical Society. Section A* **1950,** *63* (5), 444.

30.		Young, T., III. An essay on the cohesion of fluids. *Philosophical Transactions of the Royal Society of London* **1997,** *95*, 65-87.

31.		Wenzel, R. N. N., Resistance of solid surfaces to wetting by water. *Industrial & engineering chemistry.* **1936,** *28* (8), 988-994.

32.		Cassie, A. B. D.; Baxter, S., Wettability of porous surfaces. *Transactions of the Faraday Society* **1944,** *40* (0), 546-551.

33.		Banerjee, S. S., Simple derivation of Young, Wenzel and Cassie-Baxter equations and its interpretations. *arXiv: Materials Science* **2008**.

34.		Rauter, M. T.; Schnell, S. K.; Kjelstrup, S., Cassie–Baxter and Wenzel States and the Effect of Interfaces on Transport Properties across Membranes. *The Journal of Physical Chemistry B* **2021,** *125* (46), 12730-12740.

35.		Murakami, D.; Jinnai, H.; Takahara, A., Wetting Transition from the Cassie–Baxter State to the Wenzel State on Textured Polymer Surfaces. *Langmuir* **2014,** *30* (8), 2061-2067.

36.		Edachery, V.; R, S.; Kailas, S. V., Influence of surface texture directionality and roughness on wettability, sliding angle, contact angle hysteresis, and lubricant entrapment capability. *Tribology International* **2021,** *158*, 106932.

37.		Pierce, E.; Carmona, F. J.; Amirfazli, A., Understanding of sliding and contact angle results in tilted plate experiments. *Colloids and Surfaces A: Physicochemical and Engineering Aspects* **2008,** *323* (1), 73-82.

38.		Kalin, M.; Polajnar, M., The Effect of Wetting and Surface Energy on the Friction and Slip in Oil-Lubricated Contacts. *Tribology Letters* **2013,** *52* (2), 185-194.

39.   Rio, E.; Daerr, A.; Andreotti, B.; Limat, L., Boundary Conditions in the Vicinity of a Dynamic Contact Line: Experimental Investigation of Viscous Drops Sliding Down an Inclined Plane. *Physical Review Letters* **2005,** *94* (2), 024503.

40.   Beitollahpoor, M.; Farzam, M.; Pesika, N. S., Determination of the Sliding Angle of Water Drops on Surfaces from Friction Force Measurements. *Langmuir* **2022,** *38* (6), 2132-2136.

41.   Li, X.; Bodziony, F.; Yin, M.; Marschall, H.; Berger, R.; Butt, H.-J., Kinetic drop friction. *Nature Communications* **2023,** *14* (1), 4571.

42.   Tang, S.; Bhimavarapu, Y.; Gulec, S.; Das, R.; Liu, J.; N?guessan, H.; Whitehead, T.; Yao, C.-W.; Tadmor, R., Droplets Sliding down a Vertical Surface under Increasing Horizontal Forces. *Langmuir* **2019,** *35* (25), 8191-8198.

43.   Bico, J.; Reyssat, É.; Roman, B., Elastocapillarity: When Surface Tension Deforms Elastic Solids. *Annual Review of Fluid Mechanics* **2018,** *50* (Volume 50, 2018), 629-659.

44.   Roman, B.; Bico, J., Elasto-capillarity: deforming an elastic structure with a liquid droplet. *Journal of Physics: Condensed Matter* **2010,** *22* (49), 493101.

45.   Aristoff, J. M.; Duprat, C.; Stone, H. A., Elastocapillary imbibition. *International Journal of Non-Linear Mechanics* **2011,** *46* (4), 648-656.

46.   Wang, H.; Qin, Q.-H., Chapter 2 - Mechanics of solids and structures. In *Methods of Fundamental Solutions in Solid Mechanics*, Wang, H.; Qin, Q.-H., Eds. Elsevier: 2019; pp 53-90.

47.   Tawfick, S. H.; Bico, J.; Barcelo, S., Three-dimensional lithography by elasto-capillary engineering of filamentary materials. *MRS Bulletin* **2016,** *41* (2), 108-114.

48.   Bico, J.; Roman, B.; Moulin, L.; Boudaoud, A., Elastocapillary coalescence in wet hair. *Nature* **2004,** *432* (7018), 690-690.

49.   Samy, R. A.; Suthanthiraraj, P. P. A.; George, D.; Iqbal, R.; Sen, A. K., Elastocapillarity-based transport of liquidsin flexible confinements and over soft substrates. *Microfluidics and Nanofluidics* **2019,** *23* (8), 100.

50.   Yousafzai, M. S.; Yadav, V.; Amiri, S.; Staddon, M. F.; Errami, Y.; Jaspard, G.; Banerjee, S.; Murrell, M., Cell-Matrix Elastocapillary Interactions Drive Pressure-Based Wetting of Cell Aggregates. *Physical Review X* **2022,** *12* (3), 031027.

51.   De Volder, M.; Hart, A. J., Engineering Hierarchical Nanostructures by Elastocapillary Self-Assembly. *Angewandte Chemie International Edition* **2013,** *52* (9), 2412-2425.

52.   Lee, W.; Rhee, J.; Kim, J., Elastocapillarity-assisted spontaneous particle clustering system: Parallel observation of enhanced interparticle reaction utilizing evaporative preconcentration. *Sensors and Actuators B: Chemical* **2023,** *378*, 133175.

53.   Pokroy, B.; Kang, S. H.; Mahadevan, L.; Aizenberg, J., Self-Organization of a Mesoscale Bristle into Ordered, Hierarchical Helical Assemblies. *Science* **2009,** *323* (5911), 237-240.

54.   Ali, N.; Bilal, M.; Khan, A.; Ali, F.; Iqbal, H. M. N., Design, engineering and analytical perspectives of membrane materials with smart surfaces for efficient oil/water separation. *TrAC Trends in Analytical Chemistry* **2020,** *127*, 115902.

55.   Zhang, H.; Zhu, H.; Liang, X.; Liu, P.; Zhang, Q.; Zhu, S., Wrinkled smart surfaces: Enhanced switchable wettability and directional liquid transportation. *Applied Surface Science* **2020,** *513*, 145810.

56.   Song, Y.; Yang, J.; Zhang, X.; Zhang, Z.; Hu, X.; Cheng, G.; Liu, Y.; Lv, G.; Ding, J., Temperature-responsive peristome-structured smart surface for the unidirectional controllable motion of large droplets. *Microsystems & Nanoengineering* **2023,** *9* (1), 119.

57.   Yang, C.; Wu, L.; Li, G., Magnetically Responsive Superhydrophobic Surface: In Situ Reversible Switching of Water Droplet Wettability and Adhesion for Droplet Manipulation. *ACS Applied Materials & Interfaces* **2018,** *10* (23), 20150-20158.

58.   Xia, Y.; He, Y.; Zhang, F.; Liu, Y.; Leng, J., A Review of Shape Memory Polymers and Composites: Mechanisms, Materials, and Applications. *Advanced Materials* **2021,** *33* (6), 2000713.

59.   Bahl, S.; Nagar, H.; Singh, I.; Sehgal, S., Smart materials types, properties and applications: A review. *Materials Today: Proceedings* **2020,** *28*, 1302-1306.

60.   Apsite, I.; Salehi, S.; Ionov, L., Materials for Smart Soft Actuator Systems. *Chemical Reviews* **2022,** *122* (1), 1349-1415.

61.   Dayyoub, T.; Maksimkin, A. V.; Filippova, O. V.; Tcherdyntsev, V. V.; Telyshev, D. V. Shape Memory Polymers as Smart Materials: A Review *Polymers* [Online], 2022.

62.   Xue, Y.; Lei, J.; Liu, Z., A thermodynamic constitutive model for shape memory polymers based on phase transition. *Polymer* **2022,** *243*, 124623.

63.   Siwakoti, M.; Mailen, R. W., Relationship between recovered enthalpy and the shape-memory effect in shape memory polymers. *Journal of Applied Polymer Science* **2023,** *140* (48), e54727.

64.   Suethao, S.; Prasopdee, T.; Buaksuntear, K.; Shah, D. U.; Smitthipong, W. Recent Developments in Shape Memory Elastomers for Biotechnology Applications *Polymers* [Online], 2022.

65.   Das, A.; Mahanwar, P., A brief discussion on advances in polyurethane applications. *Advanced Industrial and Engineering Polymer Research* **2020,** *3* (3), 93-101.

66.   Wendels, S.; Avérous, L., Biobased polyurethanes for biomedical applications. *Bioactive Materials* **2021,** *6* (4), 1083-1106.

67.   Petrović, Z. S.; Ferguson, J., Polyurethane elastomers. *Progress in Polymer Science* **1991,** *16* (5), 695-836.

68.   Liu, W.; Zhao, Y.; Wang, R.; Li, J.; Li, J.; Luo, F.; Tan, H.; Fu, Q., Post-Crosslinked Polyurethanes with Excellent Shape Memory Property. *Macromolecular Rapid Communications* **2017,** *38* (23), 1700450.

69.   Bothe, M.; Emmerling, F.; Pretsch, T., Poly(ester urethane) with Varying Polyester Chain Length: Polymorphism and Shape-Memory Behavior. *Macromolecular Chemistry and Physics* **2013,** *214* (23), 2683-2693.

70.   Wang, J.-N.; Liu, Y.-Q.; Zhang, Y.-L.; Feng, J.; Sun, H.-B., Pneumatic smart surfaces with rapidly switchable dominant and latent superhydrophobicity. *NPG Asia Materials* **2018,** *10* (2), e470-e470.

71.   Zhang, D.; Cheng, Z.; Kang, H.; Yu, J.; Liu, Y.; Jiang, L., A Smart Superwetting Surface with Responsivity in Both Surface Chemistry and Microstructure. *Angewandte Chemie International Edition* **2018,** *57* (14), 3701-3705.

72.   Constante, G.; Apsite, I.; Alkhamis, H.; Dulle, M.; Schwarzer, M.; Caspari, A.; Synytska, A.; Salehi, S.; Ionov, L., 4D Biofabrication Using a Combination of 3D Printing and Melt-Electrowriting of Shape-Morphing Polymers. *ACS Applied Materials & Interfaces* **2021,** *13* (11), 12767-12776.

73.   Girard, F.; Lajoye, C.; Camman, M.; Tissot, N.; Berthelot Pedurand, F.; Tandon, B.; Moedder, D.; Liashenko, I.; Salameh, S.; Dalton, P. D.; Rielland, M., First Advanced Bilayer Scaffolds for Tailored Skin Tissue Engineering Produced via Electrospinning and Melt Electrowriting. *Advanced Functional Materials* **2024,** *n/a* (n/a), 2314757.

74.   Daghrery, A.; Ferreira, J. A.; Xu, J.; Golafshan, N.; Kaigler, D.; Bhaduri, S. B.; Malda, J.; Castilho, M.; Bottino, M. C., Tissue-specific melt electrowritten polymeric scaffolds for coordinated regeneration of soft and hard periodontal tissues. *Bioactive Materials* **2023,** *19*, 268-281.

75.   Javadzadeh, M.; del Barrio, J.; Sánchez-Somolinos, C., Melt Electrowriting of Liquid Crystal Elastomer Scaffolds with Programmed Mechanical Response. *Advanced Materials* **2023,** *35* (14), 2209244.

76.   G. Saiz, P.; Reizabal, A.; Luposchainsky, S.; Vilas-Vilela, J. L.; Lanceros-Mendez, S.; Dalton, P. D., Magnetically Responsive Melt Electrowritten Structures. *Advanced Materials Technologies* **2023,** *8* (13), 2202063.

77.   Constante, G.; Apsite, I.; Auerbach, P.; Aland, S.; Schönfeld, D.; Pretsch, T.; Milkin, P.; Ionov, L., Smart Mechanically Tunable Surfaces with Shape Memory Behavior and Wetting-Programmable Topography. *ACS Applied Materials & Interfaces* **2022,** *14* (17), 20208-20219.

78.   Constante, G.; Apsite, I.; Schönfeld, D.; Pretsch, T.; Ionov, L., Reversibly Photoswitchable High-Aspect Ratio Surfaces. *Small Structures* **2023,** *4* (10), 2300040.

79.   Constante, G.; Schönfeld, D.; Pretsch, T.; Milkin, P.; Sadilov, I.; Ionov, L., Switchable Elastocapillarity of High-Aspect-Ratio Topographically Structured Surfaces. *Langmuir* **2025**.

7.   Publication list

1. **Constante, G.**, Apsite, I., Auerbach, P., Aland, S., Schönfeld, D., Pretsch, T., Milkin, P., and Ionov, L (2022), Smart Mechanically Tunable Surfaces with Shape Memory Behavior and Wetting-Programmable Topography. *ACS Applied Materials & Interfaces* 14 (17), 20208-20219. https://pubs.acs.org/doi/10.1021/acsami.2c01078

2. **Constante, G.,** Apsite, I., Schönfeld, D., Pretsch, T. and Ionov, L. (2023), Reversibly Photoswitchable High-Aspect Ratio Surfaces. *Small Structures*, 4: 2300040. https://doi.org/10.1002/sstr.202300040

3. **Constante, G.,** Schönfeld, D., Pretsch, T., Milkin, P., Sadilov, I., and Ionov, L. (2025), Switchable Elastocapillarity of High-Aspect-Ratio Topographically Structured Surfaces. *Langmuir,* Article ASAP.
   https://pubs.acs.org/doi/10.1021/acs.langmuir.5c02002

Not included in this dissertation:

1. **Constante, G.,** Apsite, I., Alkhamis, H., Dulle, M., Schwarzer, M., Caspari, A., Synytska, A., Salehi, S., and Ionov, L. (2021), 4D Biofabrication Using a Combination of 3D Printing and Melt-Electrowriting of Shape-Morphing Polymers. *ACS Applied Materials & Interfaces* 13 (11), 12767-12776. https://pubs.acs.org/doi/10.1021/acsami.0c18608

2. Uribe-Gomez, J., Posada-Murcia, A., Shukla, A., Ergin, M., **Constante, G**., Apsite, I., Martin, D., Schwarzer, M., Caspari, A., Synytska, A., Salehi, S., and Ionov, L. (2021), Shape-Morphing Fibrous Hydrogel/Elastomer Bilayers Fabricated by a Combination of 3D Printing and Melt Electrowriting for Muscle Tissue Regeneration. *ACS Applied Bio Materials* 4 (2), 1720-1730. https://pubs.acs.org/doi/10.1021/acsabm.0c01495

3. Trujillo-Miranda, M., Apsite, I., Agudo, J. A. R., **Constante, G**., and Ionov, L. 4D Biofabrication of Mechanically Stable Tubular Constructs Using Shape Morphing Porous Bilayers for Vascularization Application. *Macromol. Biosci*. 2023, 23, 2200320. https://doi.org/10.1002/mabi.202200320

4. Pasini, C., Soreño, Z. V., Schönfeld, D., Pretsch, T., **Constante, G**., Sadilov, I., and Ionov, L. 4D Fabrication of Two-Way Shape Memory Polymeric Composites by

Electrospinning and Melt Electrowriting. *Macromol. Rapid Commun.* 2024, 45, 2400010. https://doi.org/10.1002/marc.202400010

5. Sadilov, I., **Constante, G.,** Dulle, M., Schönfeld, D., Pretsch, T., and Ionov, L. Reversible Switchable Topography Enabled by Melting and Crystallization of Melt-Electrowritten Polymer Fibers. *ACS Materials Letters*. 2025 7 (2), 401-408. https://pubs.acs.org/doi/10.1021/acsmaterialslett.4c02057

8.   Individual contribution to publications and manuscripts

1. **Constante, G.**, Apsite, I., Auerbach, P., Aland, S., Schönfeld, D., Pretsch, T., Milkin, P., and Ionov, L (2022), Smart Mechanically Tunable Surfaces with Shape Memory Behavior and Wetting-Programmable Topography. *ACS Applied Materials & Interfaces* 14 (17), 20208-20219. https://pubs.acs.org/doi/10.1021/acsami.2c01078

The research concept was developed by Prof. Leonid Ionov, Dr. Indra Apsite, and me. The polymer synthesis was carried out by Dennis Schönfeld and Dr. Thorsten Pretsch. The design and fabrication of the samples were prepared by myself. Thermal and mechanical characterization of the material was made by Pavel Milkin and I. Paul Auerbach and Prof. Sebastian Aland worked on numerical simulation studies for hard lamellae. I performed the shape-memory and application experiments and, together with Dr. Indra Apsite and Prof. Leonid Ionov, we did the data analysis. The manuscript (text and images) was made by me and modified by Dr. Indra Apsite and Prof. Leonid Ionov. Prof. Leonid Ionov supervised the project and contributed to the completion of the manuscript.

2. **Constante, G.,** Apsite, I., Schönfeld, D., Pretsch, T., and Ionov, L. (2023), Reversibly Photoswitchable High-Aspect Ratio Surfaces. *Small Structures*, 4: 2300040. https://doi.org/10.1002/sstr.202300040

The concept of the research was developed by Dr. Indra Apsite, Prof. Leonid Ionov, and me. Dennis Schönfeld and Dr. Thorsten Pretsch contributed to the polymer synthesis. The design and fabrication of the samples were prepared by myself. Photothermal and mechanical characterization of the material was performed by me. Shape-memory experiments and application were done by me, and together with Dr. Indra Apsite and Prof. Leonid Ionov, we analyzed data processing. The manuscript (text and images) was made by myself and modified by Dr. Indra Apsite and Prof. Leonid Ionov. Prof. Leonid Ionov supervised the project and contributed to the completion of the manuscript.

1. **Constante, G.,** Schönfeld, D., Pretsch, T., Milkin, P., Sadilov, I., and Ionov, L. (2025), Switchable Elastocapillarity of High-Aspect-Ratio Topographically Structured Surfaces. *Langmuir,* Article ASAP.

   https://pubs.acs.org/doi/10.1021/acs.langmuir.5c02002

The concept of the research was developed by Prof. Leonid Ionov and myself. The synthesis of the polymer was made by Dennis Schönfeld and Dr. Thorsten Pretsch. The design and fabrication of the samples were prepared by myself. Estimation of friction force between the materials of the samples was performed by Pavel Milkin and myself. Elastocapillarity deformation studies were done by me, and together with Prof. Leonid Ionov, the analysis of data was done. The analysis of forces during deflection and deformation of the lamellar surfaces was done by Ilia Sadilov and myself. The manuscript (text and images) was made by myself and modified by Prof. Leonid Ionov. Prof. Leonid Ionov supervised the project and contributed to the completion of the manuscript.

9.   Publications/Manuscripts

9.1. Publication 1

Smart Mechanically Tunable Surfaces with Shape Memory Behavior and Wetting-Programmable Topography

Gissela Constante, Indra Apsite, Paul Auerbach, Sebastian Aland, Dennis Schönfeld, Thorsten Pretsch, Pavel Milkin, and Leonid Ionov

Smart Mechanically Tunable Surfaces with Shape Memory Behavior and Wetting-Programmable Topography

Gissela Constante, Indra Apsite, Paul Auerbach, Sebastian Aland, Dennis Schönfeld, Thorsten Pretsch, Pavel Milkin, and Leonid Ionov*

Read Online

ACCESS | Metrics & More | Article Recommendations | Supporting Information

ABSTRACT: This paper reports for the first time the fabrication and investigation of wetting properties of structured surfaces formed by lamellae with an exceptionally high aspect ratio of up to 57:1 and more. The lamellar surfaces were fabricated using a polymer with tunable mechanical properties and shape-memory behavior. It was found that wetting properties of such structured surfaces depend on temperature, and thermal treatment history-structured surfaces are wetted easier at elevated temperature or after cooling to room temperature when the polymer is soft because of the easier deformability of lamellae. The shape of lamellae deformed by droplets can be temporarily fixed at low temperature and remains fixed upon heating to room temperature. Heating above the transition temperature of the shape-memory polymer restores the original shape. The high aspect ratio allows tuning of geometry not only manually, as it is done in most works reported previously but can also be made by a liquid droplet and is controlled by temperature. This behavior opens new opportunities for the design of novel smart elements for microfluidic devices such as smart valves, whose state and behavior can be switched by thermal stimuli: valves that can or cannot be opened that are able to close or can be fixed in an open or closed states.

KEYWORDS: shape-memory polymer, wettability, tunable topography, deformation, advancing and receding volume, thermoresponsiveness
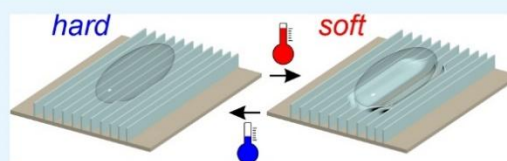
1. INTRODUCTION

Investigation of surface wettability and exploring possibilities for its manipulation became a subject of intense research over the last decades because of their importance for material design,[1] control of biological processes,[2] and even for the technological industry.[3] For instance, highly hydrophilic and superhydrophobic materials can be useful for the development of self-cleaning coatings that are used to reduce corrosion, weathering, and erosion[4,5] or to prevent the accumulation of marine organisms on boats.[6−8] Various kinds of wetting behavior are also observed in nature and are used by living organisms for adaptation and to increase their survival rate. For example, the leaves of the lotus plant *Nelumbo* possesses a superhydrophobic behavior that is due to their special surface structure: the surface is formed by hierarchical micropapillae with a combination of epicuticular wax crystals on top. This arrangement allows the rolling and sliding of water droplets, which collect dust and dirt particles from the leaf surface allowing self-cleaning without energy consumption.[9] Another example is rose petals, which possess microscale papillae that are partially covered with nanoscale striae[10] facilitating the pinning of water to help them stay hydrated.[10,11] In turn, rice leaves use aligned anisotropic topographic lamellae to produce a bidirectional wettability.[12] Their surface is covered with micro- and nanoscale structures that form a superhydrophobic surface for self-cleaning and water repellency.[13] Also, animals such as geckos and desert beetles have developed surfaces with

specific wettability to overcome harsh environmental conditions. Geckos have a specific arrangement on the skin at their feet to improve adherence by varying the surface through a transition between Wenzel and Cassie state.[14] Desert beetles have waxy bumps on their surface for collecting water from fogs.

Active control (switching) or passive adaptation of wetting properties can allow new applications of engineering materials and are beneficial for applications in biotechnology[15] like cell capture/release and biodetection,[16] microfluidics,[17] textiles,[18] fabrication of sensors,[19] and others. Minko et al. developed self-adaptative surfaces (SAS) based on polystyrene/poly-(vinylpyridine) brushes.[20] The design of smart surfaces with switchable/adaptive wetting is done primarily through two approaches. The first assumes the change in surface chemistry due to the incorporation of sensitive molecules that can respond to a certain stimulus, for example, pH,[21,22] light,[23] temperature,[24] and others. The second approach assumes the switching of the surface topography. Surfaces with specific topography are usually fabricated from materials with tunable

20208
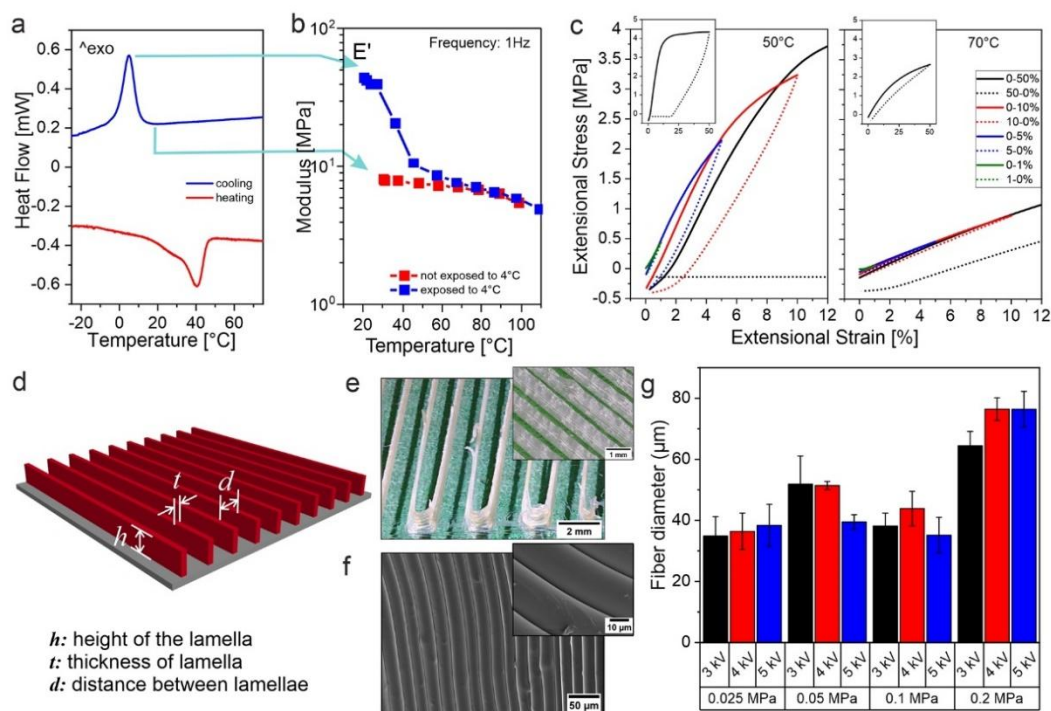
Figure 1. Thermal and mechanical properties of TPU PBA-75 and morphology of structured surfaces fabricated from TPU PBA-75 using melt electrowriting. (a) DSC; (b) DMA of polymer, which was exposed to 4 °C (blue) and which was not exposed to 4 °C (red); (c) results of cyclical stretching; (d) schematics and (e,f) microscopy images (optical microscopy) and (SEM) of the morphology of fabricated surfaces; (g) dependence of fiber diameter on conditions of melt electrowriting.

mechanical properties, which are reversibly deformed by pressing, stretching, or bending.[21,25] Fabrication of surfaces with switchable topography requires both the development of materials with tailorable properties and methods to fabricate structured surfaces. Examples of materials used for the fabrication of switchable topography surfaces are shape-memory polymers,[11] hydrogels,[21] and liquid crystalline elastomers.[26,27] For example, Zhang et al.[21] demonstrated switching of topography of surfaces formed by micropillars with shape-memory behavior. These surfaces are superhydrophobic when pillars are undeformed. The pillars can be deformed (compressed) manually at elevated temperature and fixed in the deformed state at room temperature. Such deformed surfaces do not possess superhydrophobic behavior but they are able to recover to their initial superhydrophobic state upon heating. Switching of surface topography can also be achieved by light as it was demonstrated on the example of films made of photosensitive liquid crystalline elastomers.[28] Adhesion properties of such surfaces can be, thus, switched by illumination with light. Magnetic field can also be used to switch surface topography magnetically switchable surfaces are designed by incorporation of magnetic particles.[11] Moreover, topography of surfaces with micro air sacs can be switched due to inflation or deflation of sacs by applying different pneumatic pressure. This change of wettability can be used for capturing/releasing water droplets.[29]

Diverse methods including photolithography,[15,30,31] stereolithography,[32] soft-lithography,[33] etching,[34] and self-assembly[35] are widely used for the preparation of such surfaces allowing the formation of microbumps with a height of a few microns to almost 100 μm.[21,30,31,36-38] The typical aspect ratio (height/

width ratio) of such structures is relatively low: 0.25:1,[37] 1:1,[36] 2:1,[30] 3:1.[21] Such microbump shape-memory structures provide superhydrophobic behavior in their initial state, and by mechanical programming (deformation) changes their wetting properties and the surfaces behave like rice leaves: water droplets are pinned.[39] Similarly, structures mimicking the behavior of rice leaf surfaces can be made using electrospinning, although this technique provides uneven deposition of fibers leading to a high variation in the fiber mat thickness and distance. With this method, the height of features remains low ($\sim$300 nm), and the distance between the fiber arrays varies between 0.25 and 1 μm.[40] Although these smart surfaces show interesting programmable hydrophilic and hydrophobic properties, their height is limited to a few micrometers, and the aspect ratio is not higher than 3:1. Because of the low aspect ratio, the features cannot be substantially deformed by droplets because of surface tension (the deflection amplitude of a beam decreases with its length at the same applied force). Therefore, manual deformation is always required to program the shape of the surface feature that substantially restricts the applicability of such surfaces.

In this article, we report for the first time on the fabrication of polymeric lamellar structures with tunable mechanical as well as shape-memory properties and investigate their surface-specific wetting properties. The individual structures were characterized by high aspect ratios, nominally by a height/width ratio up to 57:1, and they were studied with regard to their shape-memory behavior and tunable thermomechanical properties. The high aspect ratio allows tuning of geometry not only manually, as it is done in most works reported previously, but can also be realized by placing a liquid droplet on top of

the structure and is controlled by temperature. This approach opens new technological opportunities for the design of smart elements for microfluidic devices such as smart valves, which (i) cannot be opened at low temperature, (ii) can be opened by liquid at high temperature, (iii) can be left in an open state after cooling when liquid is applied and (iv) a closed state at elevated temperature if no liquid is applied. In this way, an approach is pursued in which the so-called "If-Then-Else" relationships apply. Such approaches of self-sufficiently reacting material systems are currently being intensively researched in connection with programmable materials.[41−46]

In contrast to previously reported surface patterning techniques, in this work we have used melt-electrowriting (MEW) to allow the fabrication of high aspect ratio features and expand the possibilities of the available materials. MEW is a novel, solvent-free additive manufacturing technique that relies on a combination of 3D printing and electrospinning that enables programmed deposition of polymeric microfibers with precision around 1 μm.[47] MEW allows the deposition of different classes of melt-processable polymers such as polyesters[48,49] and thermoplastic elastomers.[50,51] The main advantage of MEW of thermoplastic polymer materials is the possibility of depositing very thin continuous fibers (1−100 μm) one on top of the other in a programmable way[50,52] to produce a high aspect ratio of the "walls" or lamellae (aspect ratio can be up to 100:1). As material technology for the surface fabrication, we have used a thermoplastic polyurethane (TPU) with shape-memory behavior, which offers very interesting combinations of properties such as thermally adaptive mechanical properties and the ability to recover shape on heating.[53,54] As a matter of fact, the high aspect ratio of surface features, which is enabled by MEW, allows their deformation by water droplets. In combination with the switching of mechanical properties together with pronounced shape-memory properties, it allows reversible programming of the topology/morphology and wetting state of the surface affected by temperature and the presence of water droplets.

2. RESULTS AND DISCUSSION

As a material basis for the present work, we synthesized a phase segregated thermoplastic poly(ester urethane) (PEU). The hard segments of the PEU were built up by 4,4′-diphenylmethane diisocyanate (MDI) and 1,4-butanediol (BD), whereas poly(1,4-butylene adipate) (PBA) was used as soft segment. Since the weight percentage of the PBA phase was approximately 75%, the abbreviation TPU PBA-75 will be used hereafter. The physical properties of such thermoplastic polyurethanes are known to depend, among others, on the molecular weight of the soft segment, the molar ratio between hard and soft segments, and the polymerization process.[55−59]

The DSC thermogram of the synthesized TPU PBA-75 shows a peak associated with the melting of the soft segment with onset at 28 °C and a maximum at 40 °C (Figure 1a). The onset of the polymer's crystallization transition is at 10 °C and its maximum is at 5 °C. The degree of crystallinity (χ_c) was calculated from the melting enthalpy of $\Delta H_m = -22.18$ J g^{-1}, and it was $\chi_c = 21.9\%$. For pure PBA the melting enthalpy is 135 J g^{-1} ($\Delta H_m = 135$ J g^{-1}, $\chi_c = 100\%$).[60] Discrepancies between melting and crystallization temperatures of pure PBA and PBA-based TPU can be explained by the fact that in the case of the TPU, the crystallization of soft segments is hindered by the presence of hard polyurethane segments. In other words, TPU PBA-75 is a classical physically cross-linked

shape-memory polymer with a crystallizable soft segment. Interestingly, due to the soft segment phase transitions the PBA phase can be both amorphous or semicrystalline at room temperature for a certain time, depending on its previous exposure to high or low temperatures.

The mechanical properties of the polymer were characterized by small-amplitude dynamic mechanical analysis (DMA) (Figure 1b) and cyclic stretching with different amplitudes at a constant rate (Figure 1c). For the DMA experiment, the polymer was exposed to 4 °C overnight in order to ensure the distinct crystallization of the soft segment, and then it was heated to room temperature. Since PBA melts at about 40 °C, the soft segment is expected to be in a semicrystalline state at room temperature. Indeed, we observed that the precooled polymer is initially hard at room temperature ($E' \approx 55$ MPa), and heating above the melting temperature (about 40 °C) makes the polymer softer ($E' \approx 8$ MPa). The same polymer, which was not exposed to 4 °C and was kept at room temperature before doing the measurement, did not show a change of elastic modulus upon heating from room temperature to 80 °C. This means that soft segments remained mainly amorphous at room temperature and require lower temperatures to crystallize, showing a dependency on the thermal pretreatment. We performed cyclical mechanical tests at two different temperatures: 50 and 70 °C to investigate the mechanical properties (modulus and reversibility of deformation) at different amplitudes of deformation (Figure 1c). It was found that an increase in temperature from 50 to 70 °C results in a decrease of elastic modulus from 50 ± 5 down to 9 ± 1 MPa (Table S1). Moreover, it was found that the strain-reversibility and resilience increase upon heating to 70 °C (Table 1). These results fit with the deformation behavior of

Table 1. Resilience and Recovery of the TPU PBA-75 Measured at the Melting Point of the Soft Segment (50°C) and Temperature of Deformation Used for the Shape-Memory Studies (70°C)

temperature [°C]	max. strain [%]	resilience [%]	recovery [%]
50	5	60.38	77.75
70	5	86.68	90.78

similar shape-memory poly(ester urethanes) described previously.[61,62] Thus, the polymer is hard at room temperature, when it is preliminary exposed to 4 °C, and soft and elastic (deformation is reversible) at 70 °C. To investigate shape-memory behavior, lamellae were bent at 70 °C and then fixed by cooling to 4 °C. Upon heating to 70 °C, the lamellae recovered their original shape, and the structures demonstrate promising surface-related shape-memory properties. Thus, the polymer demonstrated shape-memory properties and memory of mechanical properties. The specific temperatures at which the polymer switches to soft (above room temperature) and hard (below room temperature but above water freezing point) states, as well as the specific temperature range (around room temperature) solely depend on thermal treatment (polymer exposed to 70 °C for 5 min). This makes the shape-memory polymer a highly interesting candidate for fabricating devices with tunable and programmable thermomechanical properties.

We fabricated surfaces from TPU PBA-75 with patterned topography. A design of parallel lamellae with different heights, which is determined by the number of layers, and the distance between them was produced using melt electrowriting (Figure

55
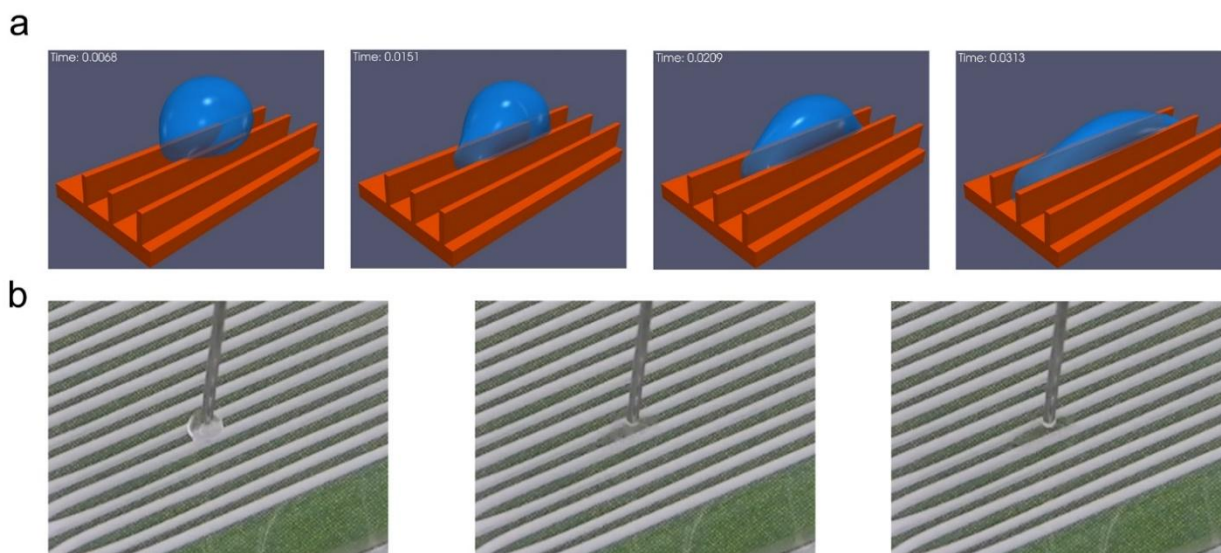
Figure 2. (a) Simulation and (b) experimental results of water behavior on a thick and hard lamellae structure.
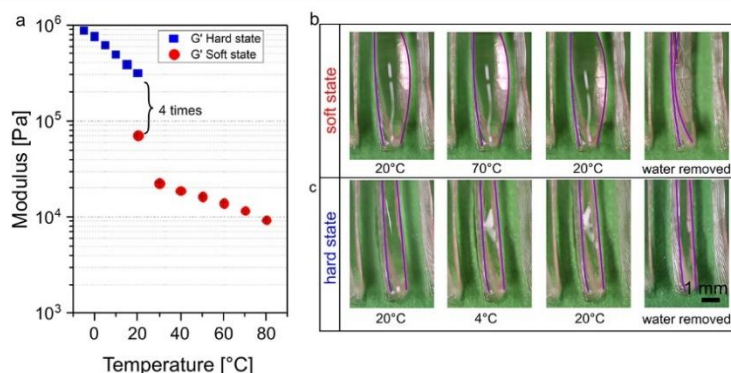

Figure 3. Thermomechanical studies of TPU PBA-75. (a) Pseudorheological studies of hard lamellae (thermal pretreatment: cooling to −5 °C and heating to 20 °C) and soft lamellae (thermal pretreatment heating to 80 °C and cooling to 20 °C); (b) images of the behavior analysis of the lamellae when it has been exposed to 70 °C; and (c) exposed to 4 °C.

1d−f) on a glass slide substrate coated by a thin layer of polylactic acid (PLA). A high aspect ratio of lamellae was achieved with the stacking of fibers (height/width ratio up to 57:1). The role of PLA was to decrease the hydrophilicity on the surface of the glass slide. The contact angle of water on the glass slide increased from less than 40° to 70° after coating with PLA. This coating also improved the fiber adhesion to the substrate. We studied the effects of MEW conditions on the diameter of the fiber and the uniformity of the lamellae (Figure 1g). Pressure and voltage were found to be crucial to define the smoothness, deposition, and diameter of the fibers deposited by MEW. In particular, an increase in pressure results in an increase in the diameter of deposited fibers, because higher pressure increases the flow rate through the nozzle. The average diameter of the fiber is 37 ± 2 and 72 ± 7 μm at 0.025 and 0.2 MPa, respectively. The precision of the deposition of the fibers was found to be highly dependent on the voltage applied during the spinning. Very high voltages (5 kV) result in the formation of buckled fibers (sinusoidal shape, Figure S2) that is due to the high ratio between the fiber stretching and fiber deposition rate. Finally, 3 kV pressures between 0.025 and

0.1 MPa were chosen for the fabrication of small-diameter fibers (around 30−40 μm). Using these conditions, we fabricated lamellar surfaces with different heights (500 and 1700 μm) and distances (500 and 150 μm). The thickness of lamellae was kept at an average of 40 μm. The roughness coefficient was calculated for the topographical surface using the equation $r = \frac{\text{total area}}{\text{projected area}}$ (Figure S3). Values from 1.65 to 7.36 were obtained by varying the distance (d) and the height (h) of the lamellae.

We also investigated how droplets fill the space between the lamellae upon their advancing. The shape of the droplets, deposited in the groove between the lamellae, is spherical right after deposition and becomes elongated along the lamellae during advancing (Figure 2), that is, the wetting of structured surfaces is anisotropic. We modeled the behavior of a droplet between two stiff undeformable lamellae (the thickness of the lamellae was set to 100 μm). Numerical simulations were performed by a finite difference simulation of the Navier−Stokes equations[63] using a highly performant graphic processing unit (GPU) parallelization.[64] To regularize the contact line singularity the droplet and ambient air were

56
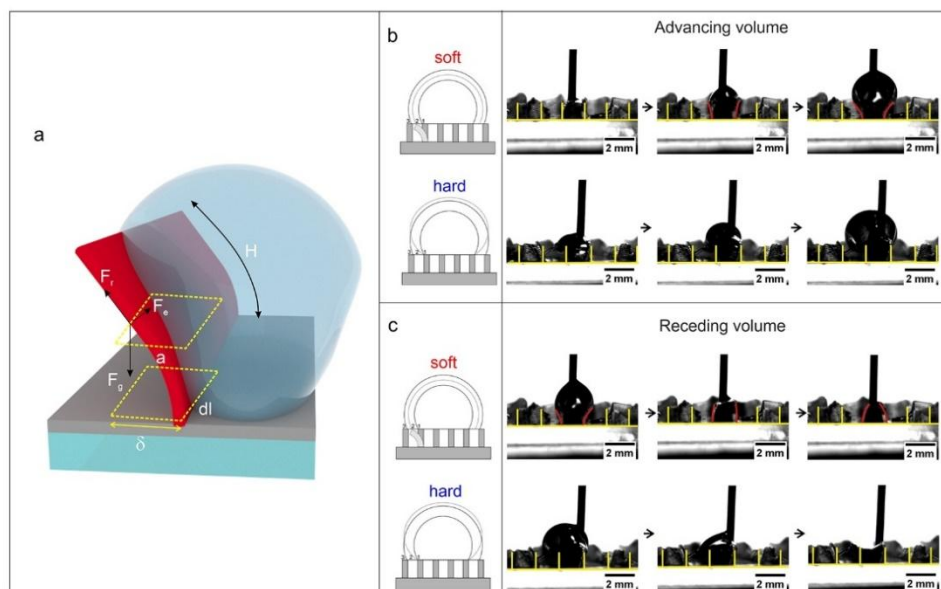
Figure 4. Deformation behavior of lamellae made from TPU PBA-75 (a) as influenced by advancing (b) and receding (c) water volume in the elastic (soft) and rigid (hard) state. Lamellae have been pushed or pulled away according to the direction of the volume of the drop.

modeled by a phase field function. The droplet was initially prescribed as a ball of radius 781 μm. The rigid lamellae were modeled by another stationary phase field and the contact angle of 72°, which is the contact angle on flat polyurethane, was imposed by the diffuse domain method.[65] The simulation shows that the droplet adapts its shape to adjust the contact angle and the dynamics of which are governed by the interplay of viscous and capillary forces. Thus, the modeling confirmed that the droplet must be initially rounded and shall get elongated during its development.

In accordance to the results of thermomechanical analysis, the lamellae showed different behavior at room temperature when they were exposed to different thermal treatments. The lamellae expressed "softness mechanical memory" when the soft segment was molten previously at higher temperatures (>70 °C). The "hardness mechanical memory" was observed when the soft segment of the polymer remains crystalline at 4 °C. The memory of mechanical properties was evidenced by quasi-rheological studies performed on the lamellae surfaces; the mechanical properties of lamellae deposited on the surface were tested by an oscillating plate in the setup used for rheological measurements. For this, the structured surfaces were exposed to high (70 °C) or low (4 °C) temperature for five minutes. Then the temperature was reduced/increased to 20 °C (RT) gradually, and G' and G'' were measured (Figure 3a). It was found that the same lamellae were hard and soft at room temperature depending on whether they were previously cooled down or heated, respectively. The results have been treated qualitatively, the obtained value does not correspond to the shear modulus of the bulk polymer. However, the trend is the same: the surface formed by the lamellae is either hard or soft at room temperature, depending on the thermal pretreatment. Thus, the mechanical properties and wetting behavior are temporarily adjustable.

The different mechanical behaviors of the lamellae according to different thermal histories are depicted in Figure 3b,c. At room temperature, a water droplet was deposited between two lamellae, which were exposed before to low (Figure 3c) and high (Figure 3b) temperatures. We observed that water droplets are able to deform the lamellae when they are soft (Figure 3b) and not able to deform them when they are hard (Figure 3c). Thus, the experiment clearly indicates different mechanical properties of lamellae when they were thermally treated, and on the fact that the lamellae can or cannot be deformed by capillary forces depending on their mechanical stiffness.

The wetting behavior of the topographical surface was analyzed by investigating advancing and receding water droplets (Figure 4) when the material was exposed to 70 °C, further in the text referred to as "soft" and, and when the material was exposed to 4 °C, further in the text referred to as "hard". Technically, 5 μL of water were added stepwise until 40 μL volume was reached. The volume of the droplet, the length of the contact line, and the number of lamellae that were in contact with the water drop were analyzed during the measurements of advancing and receding contact angles. First, experiments showed that the wetting properties of fabricated surfaces depend on the temperature in good correlation to the preliminary test in Figure 3. The lamellae remain undeformed upon the increase of the size of the droplet when they are in the hard state (E = 50 MPa, treated by cooling to 4 °C). On the other hand, lamellae in soft states (E = 9 MPa, T = 70 °C) were deformed by an advancing and receding water droplet. Interestingly, the contact angle undergoes irregular changes upon increase/decrease of its size that is due to jumping of the droplet between neighboring lamellae. It is clear that wetting properties depend on the mechanical properties of lamellae which in turn depend on the temperature.

The deformation amplitude of lamellae is determined by a balance of surface tension ($F_s \sim \gamma \cdot dl$),[66] elastic deformation ($\delta \sim F \cdot H^3/EI$, where H is the height of lamella, I is second moment of inertia $I = a \cdot dl^3/12$, a is the thickness of a lamella, and dl is its length), and gravity ($F_g \sim \rho \cdot g \cdot h \cdot b \cdot dl$) where h is the

57
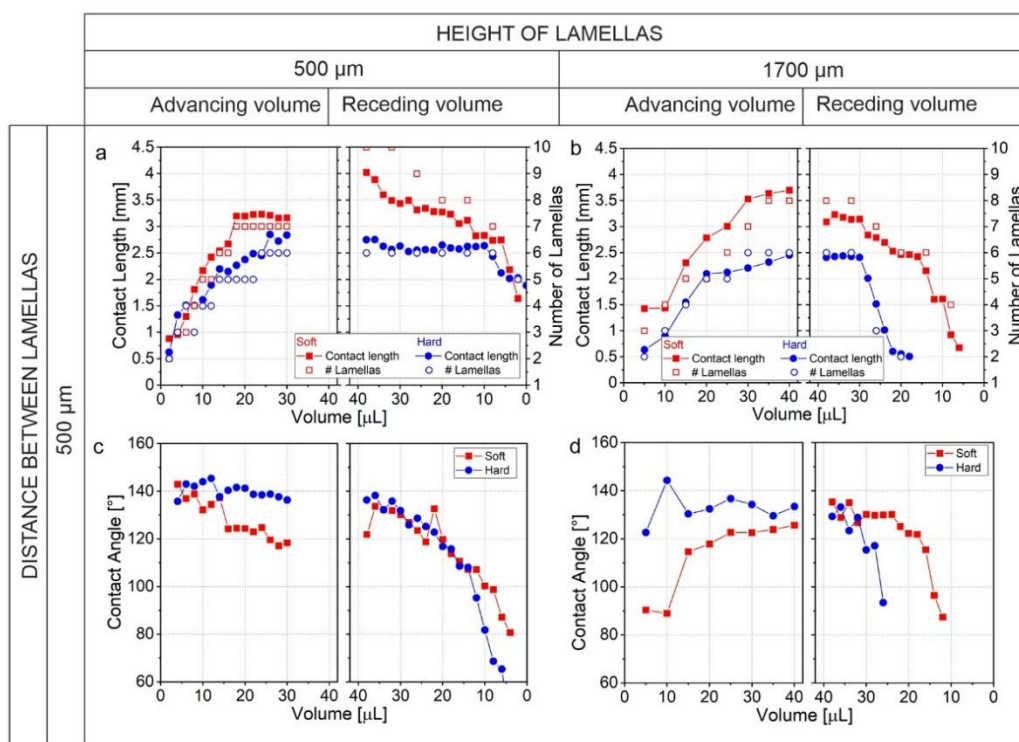
Figure 5. Effect of the volume of a water droplet on the contact length (a,b) and contact angle (c,d) between the droplet and the surface, and the number of lamellae in contact with the water droplet. The analysis has been made for both states of the lamellae, "soft" and "hard".

height of the droplet and S is surface area (Figure 4a). We used the following values: $H = 10^{-3}$ m, $a = 3 \times 10^{-5}$ m, $\delta = H/2 = 5 \times 10^{-4}$ m, and $h = 1 \times 10^{-3}$ m for estimation of linear density of the surface tension forces and gravity forces which are $F_s/dl \sim 72$ mN and $F_g/dl \sim 20$ mN. This means that gravity plays a considerable role and cannot be completely excluded from consideration. For simplicity, we however neglect effect of the gravity and the amplitude of lamellae deflection is determined by surface tension. The deflection is $\delta \sim \frac{\gamma \cdot H^3}{E \cdot a \cdot dl^2}$ and it increases linearly with the decrease of elastic modulus. This equation was derived for the case when a droplet is large or lamellas are small and whole lamella is deformed. In our case, only a part of lamella is deformed, therefore, the equation can be used only for quantitative estimation of dependences. An almost 6-fold decrease in the elastic modulus from 50 to 9 MPa (Table S1) leads to the same increase in deformation amplitude. Further, it increases with height (H) to the power of three. A 3-fold increase in the height (from 0.5 to 1.5 mm) leads to the 27-fold increase in deformation. Indeed, the low aspect ratio is the reason why structures prepared by photolithography and molding techniques[21,67] could not deformed by droplets and manual deformation was required to program their shape. The main advantage of our methods is that we are able to fabricate high aspect ratio structures; we were able to achieve an aspect ratio of 57 (larger aspect ratios are also possible), which either can or cannot be deformed by a droplet depending on their mechanical properties.

The deformation of lamellae was quantified by measuring the projected length of the contact line, which is also referred to as "contact length" (Figure S4). We also tracked the number of lamellae that were in contact with the liquid. Since the

distance between lamellae is known (it is determined during fabrication), we are able to correlate the contact length to the number of lamellae as expressed in Figure 5 in order to understand the degree and direction of lamellae deformation. In the case when lamellae are undeformed, the contact line shall be equal to interlamellar spacing (d) multiplied by the number of the spacings (n) (which is $n = N - 1$ with N as the number of lamellae): $L_{contact} = d \cdot (N - 1)$. The experimentally measured contact length can be different from the theoretically estimated one when lamellae are deformed. The bending of the lamellae in the direction away from the droplet should lead to a higher value of the experimentally measured contact length. This is typically observed during advancing contact angle measurements (Figure 4b and Figure 5). The bending of the lamellae in the direction to the droplet (receding volume) should lead to a lower value of the experimentally measured contact length. Indeed, the measured contact length is larger than the calculated one during droplet advancing and is smaller during droplet receding. Moreover, we observed that at a small interlamellar distance (500 μm) the contact length measured on soft surfaces is larger than that on hard surfaces during measurements of advancing and receding contact angles (Figure S5). As the distance between the lamellae increased, more volume was required to deform the same number of lamellae (Figure 5) because droplets do not only push on the lamellae but also spread along them (Figure S5). On the contrary, small droplets deform lamellae when the distance between them is small. For example, 6−10 μL large water drops were able deform 500 μm high lamellae when the distance between them is 500 μm. Generally, wetting results obtained for samples with large interlamellar distance (1500

58
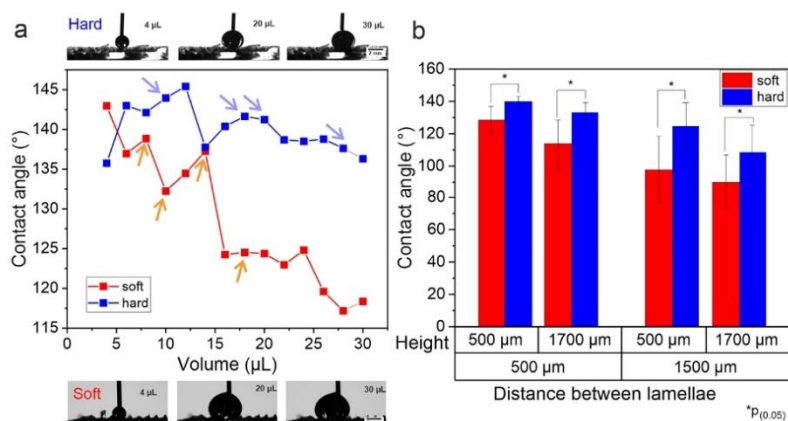
Figure 6. Advancing contact angle when the TPU PBA-75 is in a soft and hard state. (a) Example of the advancing angle for small topographies (500 μm height and 500 μm distance). Arrows show when the drop jumps to the next lamella (purple, hard state; orange, soft state). (b) Average advanced angle for the different topographies constructed.
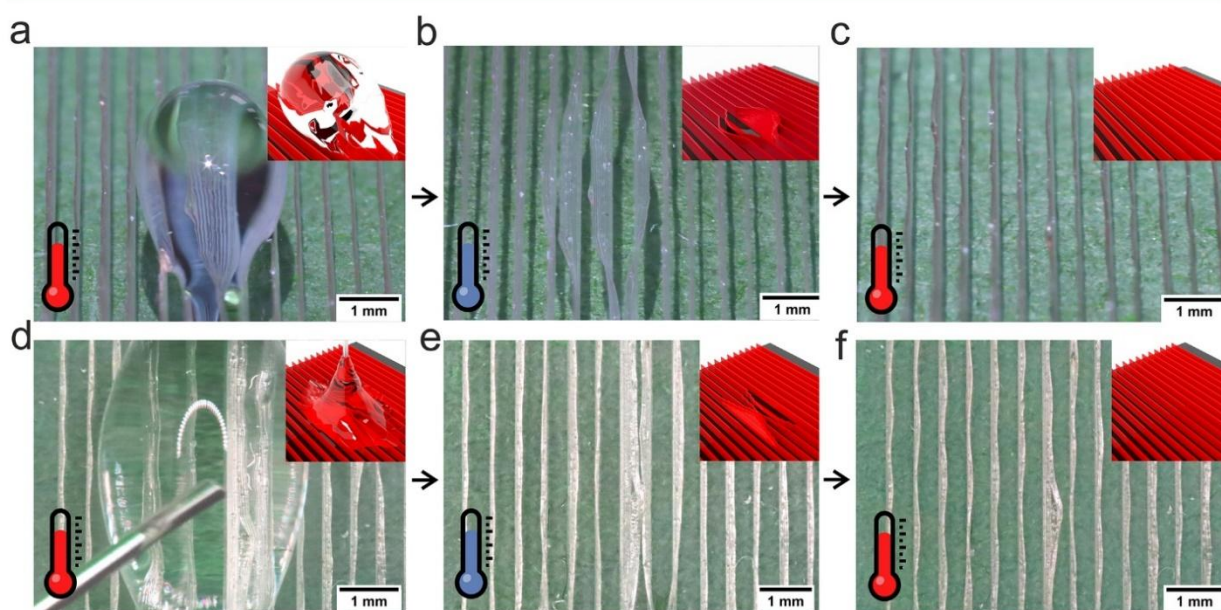
Figure 7. Shape-memory behavior of TPU PBA-75 when used as a lamellae-structured surface: (a,d) water droplet-induced deformation of the lamellae at 70 °C, (b,e) fixed shapes at 4 °C after removal of the drop, and (c,f) the recovery of the initial surface by heating to 70 °C. This study was made for advancing the volume of the water droplet (a−c) and also for the receding volume (d−f).

μm) are difficult to interpret because in this case, the size of the droplet is comparable to the distance between lamellae and the value of contact length if the droplet was larger enough to be able to touch the next lamella. Droplets of nearly the same size, one of which is able to touch lamella and one which is not able to touch lamella, show completely different wetting behavior. Thus, the water droplets have a different shape on surfaces in hard and soft states (Figure 5c,d). The advancing contact angle of droplets on surfaces in a soft state are lower than that on surfaces in hard state that is due to the adaptation of the droplet to the deformation of the lamella. On the other hand, the value of a receding contact angle on surfaces in a soft state are higher than that on surfaces in hard state. This means that water droplets are more mobile on soft surface and are more pinned to hard surface.

We performed a detailed investigation of the evolution of contact angle on hard and soft surfaces when the droplet size increases (Figure 5c,d, Figure 6). It was found that values of contact angle fluctuate during the deformation of the lamellae. This fluctuation is because jumping of the water drop to the next lamella requires certain activation energy. The contact angles increase upon inflation of droplets and drop down when it jumps to the next lamella. Generally, the contact angles on both hard and soft surfaces decrease upon the increase of the size of the droplet. The decrease on soft surfaces is however more pronounced. We explain this observation by the fact that lamellae in the soft state are easier to deform, and this deformation decreases contact angle as well as allows easier jumping to the next lamella. On the contrary, droplets on the hard surface require stronger inflation to be able to jump to the next lamella. As result, the average value of the contact angles

59
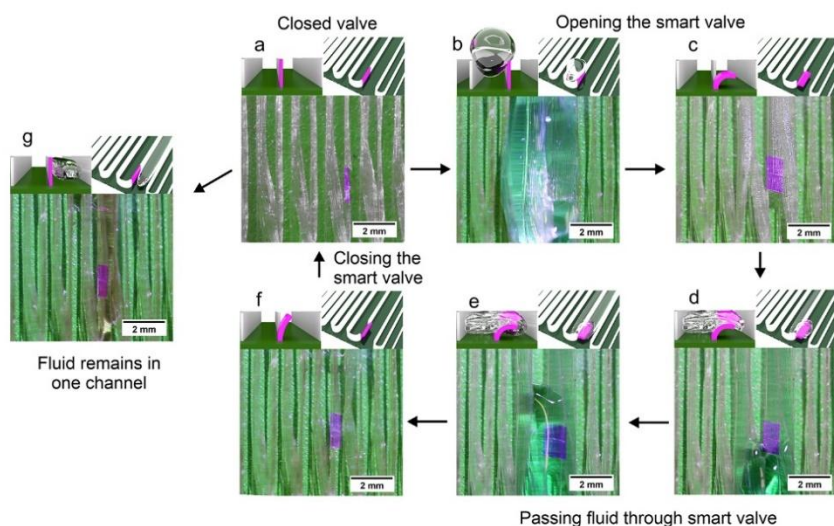
Figure 8. Application of the topographic surface of TPU PBA-75 for directing the flowing of a liquid by creating a smart valve: (a) the smart valve (purple) is made by scission of one lamella, (b) advancing volume of water drop for deforming the lamellae ($T = 70$ °C) and then fixating at 4 °C, (c) the smart valve bent (open state), (d,e) the smart valve remained open at room temperature while the fluid passed through, (f) the closing of the intelligent valve is carried out by increasing the temperature to 70 °C, and (g) the fluid cannot be directed to the next groove due to the closed smart valve.

on the soft surface is statistically significantly lower than on hard ones, and this difference increases with the distance between lamellae and their height. These observations clearly show that elastic force dominates over surface tension when lamellae are hard, while the deformation of soft lamellae is a result of the balance of surface tension and elastic force.

The TPU PBA-75, which was used for the fabrication of surfaces, exhibits shape-memory behavior. To prove this, we programmed the shape of the lamellae. Therefore, a water droplet was placed on a structured surface at 70 °C (Figure 7a,d). As a result, the droplet deformed the lamellae as discussed above. Subsequently, the surface, with the droplet sitting on deformed lamellae, was cooled down to 4 °C and then the droplet was removed (Figure 7b,e). The lamellae stayed in a deformed state even at room temperature because the melt transition temperature of the PBA soft segment was not exceeded. Heating to 70 °C results in restoration of the shape of lamellae due to the melting of the soft segment and the associated triggering of the shape-memory effect (SME) (Figure 7c,f). The experiment was repeated more than 5 times, demonstrating the reliable shape-memory properties of the lamellae.

Finally, we demonstrated the technological applicability of our insights by the combination of temperature-controlled deformability by droplets as well as SME and memory of mechanical properties for the fabrication of a smart valve, which can be controlled/programmed by a single water droplet (Figure 8). For this purpose, we fabricated lamellae with a distance of 1000 μm. The valve was made by making cuts in the direction perpendicular to one of the lamellae that formed a section, which can be bent (Figure 8a). The shape and deformability of this section can be programmed by temperature. When initially exposing the system to 4 °C and storing it at that temperature or room temperature, the valve is hard and cannot be deformed by a droplet deposited in the channel formed by lamellae (Figure 8g). The "smart valve" can be opened by advancing droplet at elevated temperatures ($T = 70$

°C) (Figure 8b). It can be fixed in (i) an open state, when it is bent and water is able to flow to the next channel. But the valve can remain in (ii) a closed state, when the lamellae has not been deformed by advancing volume, containing the fluid inside of one groove (Figure 8g). Switching back to the initial state (closing the valve) is possible by heating to 70 °C in order to trigger the SME (Figure 8f).

3. CONCLUSION

This article reports for the first time on the fabrication and investigation of wetting properties of structured surfaces with an extraordinary high aspect ratio of features (height/width ratio was 57:1, even a height/width ratio up to 75:1 was possible) formed by a polymer with switchable mechanical and shape-memory properties. It was found that wetting properties of structured surfaces depend on temperature: droplets jump from one lamella to the next one at elevated temperature when the polymer is in a soft state resulting in a lower contact angle. The lamellae are deformed by droplets at elevated temperatures and the deformed state can be temporarily fixed by cooling to 4 °C. The temporary topology recovers to the original one as soon as the structure is heated above the switching temperature of the shape-memory polymer. Thus, the high aspect ratio allows tuning of geometry not only manually, as it is done in most works reported previously, but can also be done by placing a liquid ,in this case a water droplet. Further, it is controlled by temperature: a liquid in combination with certain temperature conditions leads to distinct topography and wetting properties. This opens new opportunities for the design of smart elements of microfluidic devices such as valves which (i) cannot be opened at low temperature, (ii) can be opened by liquid at high temperature, (iii) can be left in an open state after cooling when liquid is applied, and (iv) close at elevated temperature if no liquid is applied.

60

4. EXPERIMENTAL SECTION

Materials. Desmophen 2505, which is a poly(1,4-butylene adipate) (PBA) diol, was supplied by Covestro Deutschland AG (Leverkusen, Germany), and 4,4′-diphenylmethane diisocyanate (MDI) was purchased from Fisher Scientific (Schwerte, Germany). 1,4-Butanediol (BD) as well as a molecular sieve with a pore size of 4 Å were obtained from Alfa Aesar (Kandel, Germany). Microscope glass slides were coated with a solution of polylactide (PLA 4032D) from NatureWorks Ltd. (Minnetonka, MN, U.S.A.) and dichloromethane from Merck (Darmstadt, Germany).

Synthesis of TPU. TPU PBA-75 was synthesized by the prepolymer method as recently reported.[44] For this purpose, 0.037 mol of the PBA-diol Desmophen 2505 was melted and dried overnight at 80 °C in a vacuum oven and 0.120 mol BD was stored over molecular sieve at ambient temperature. The next day, the PBA-diol was heated to 120 °C under nitrogen flow and stirring. A 0.157 mol sample of molten MDI was added, and the polymer melt was stirred continuously for about 90 min. Subsequently, the synthesized isocyanate-end-capped prepolymer was converted into TPU PBA-75 by adding BD as a chain extender. The stirring speed was then increased, and the viscosity change was monitored with an IKA Eurostar 60 control from IKA-Werke GmbH & Co. KG (Staufen, Germany). Once the viscosity increased significantly, the reaction was stopped by pouring the melt onto a plate covered with a polytetrafluoroethylene film. Finally, TPU PBA-75 obtained was cured in an oven at 80 °C for 120 min, before being ground into granules for MEW.

Spin-Coating of the Glass Slides. Microscope glass slides were spin-coated with a solution of PLA in dichloromethane (10 mg mL^{-1}). The rotational speed was set at 500 rpm for 10 s to ensure total coverage of the surface, and then, it increased to 4000 rpm for 1 min.

Fabrication of the Surfaces. The topographical structure was made via melt electrowriting of TPU PBA-75 in a 3D Discovery printer Regen Hu (Villaz-St-Pierre, Switzerland). Parameters as applied voltage, pressure, movement rate, and temperature were adjusted for the fabrication of microfibers during melt electrowriting. The TPU was melted at 215 °C. The voltage varied between 3 and 5 kV, and the distance set between the needle and the collector was set to 2 mm. Pneumatic pressure was used for the extrusion of the molten material and was fixed at 0.025, 0.05, 0.1, and 0.2 MPa. The movement rate (F) of the printhead was 10 mm s^{-1}. A metallic needle of 200 μm inner diameter was used to extrude the molten polymer. The lamellae were fabricated with the addition of linear fibers piled up one over the other. Height and distance between the lamellae varied between 500, 1250, and 1700 μm height and distances of 500, 1000, and 1500 μm.

Scanning Electron Microscopy (SEM). A scanning electron microscope (SEM) Thermo Fischer Scientific Apreo 2 SEM (Germany) was used for measuring the diameter and analyzing the morphology of MEW fibers. The samples were fixed on SEM stubs using copper adhesive tape and covered with ~1.3 nm platinum to ensure conductivity using a Leica EM ACE600 (Wetzlar, Germany). The sputtering rate was set at 0.02 nm s^{-1} with a current of 35 mA under argon at 0.05 mbar.

Differential Scanning Calorimetry (DSC). DSC 3 Mettler Toledo (Greifensee, Switzerland) was used for the thermal analysis of the TPU PBA-75. It performed two heating curves and one cooling curve. The first heating was conducted to erase the thermal history of the polymer. The heating rate was set at 1 °C min^{-1} under nitrogen flow.

Dynamical Mechanical Analysis (DMA). A Modular Compact Rheometer MCR 702 Multidrive from Anton Paar GmbH (Ostfildern, Germany) was used to perform the DMA analysis for the mechanical properties of the polymer, and cyclic extension measurements were made to analyze the elasticity of the material. A TPU filament with a diameter of 1.4 mm was used to determine the mechanical properties at temperatures between 20 and 100 °C. Because of limitations in the cooling system, the material was exposed to 4 °C overnight prior to the measurements to investigate the effect of the crystallization on the material. The frequency was kept at 1 Hz.

Recovery and resilience percentage of the material were calculated from results obtained from cyclic experiments. Following the same protocol as mentioned in our previous publication,[68] the recovery was calculated by the relation between the residual strain after the unloading step (ε) and the original strain (ε_0) (% recovery = $(1 - \varepsilon/\varepsilon_0) \times 100$). The resilience was obtained by the equation: %resilience = $(A_{unload}/A_{load}) \times 100$, where A_{unload} and A_{load} represented the area under the stress−strain curve for the unloading and loading curve, respectively.

Rheology. The rheological properties of the molten TPU PBA-75 were evaluated by using the MCR 702 Multidrive Anton Paar (Ostfildern, Germany). Parallel plate geometry of 25 mm diameter was used to measure the viscosity at 200 °C. The angular frequency was varied from 0.1−100 Hz. For the structured lamellae, a temperature ramp was performed from −5 to 20 °C and from 80 to 20 °C to analyze the temperature dependence of mechanical properties. The sample was fixed to the base and with a parallel plate geometry of 25 mm diameter, it measured the storage and loss modulus at a constant frequency of 1 Hz and constant shear strain of 1%.

Drop Shape Analysis. A Krüss Drop Shape Analyzer DSA25 (Hamburg, Germany) was used to determine the variation of the contact angle. The sessile drop method was used to determine the contact angle of the flat surface composed of spin-coated PLA. For advancing and receding volume studies, a total of 40 μL of ultrapure water was increased or decreased in multiple doses of 5 μL at a rate of 2.67 μL s^{-1}. The measurements were made at room temperature.

The shape-memory behavior of the structured topographical surface was studied by deforming the lamellae at 70 °C. By advancing and receding the volume of a water drop, the lamellae were able to deform in direction of the water flow. The sample was fixed by cooling to 4 °C. The recovery of the original state of the sample was accomplished by heating the sample to 70 °C.

■ ASSOCIATED CONTENT

Ⓢ Supporting Information

The Supporting Information is available free of charge at https://pubs.acs.org/doi/10.1021/acsami.2c01078.

> Cyclic extensional measurements of thermo-polyurethane Young's modulus of the polymer; effect of voltage and pressure in MEW Roughness coefficient of the surfaces; contact angle and contact length for samples with higher distances between the lamellae (PDF)

> Video of deformable lamellae (MP4)

> Video recovery of the lamellae (MP4)

■ AUTHOR INFORMATION

Corresponding Author

Leonid Ionov − *Faculty of Engineering Sciences, University of Bayreuth, 95447 Bayreuth, Germany; Bavarian Polymer Institute, University of Bayreuth, 95447 Bayreuth, Germany;* ⊙ orcid.org/0000-0002-0770-6140; Email: leonid.ionov@uni-bayreuth.de

Authors

Gissela Constante − *Faculty of Engineering Sciences, University of Bayreuth, 95447 Bayreuth, Germany*

Indra Apsite − *Faculty of Engineering Sciences, University of Bayreuth, 95447 Bayreuth, Germany*

Paul Auerbach − *Fakultät Informatik/Mathematik, Hochschule für Technik und Wirtschaft Dresden, 01069 Dresden, Germany*

61

Sebastian Aland − *Fakultät Informatik/Mathematik, Hochschule für Technik und Wirtschaft Dresden, 01069 Dresden, Germany; Fakultät Mathematik und Informatik, Technische Universität Bergakademie Freiberg, 09599 Freiberg, Germany*

Dennis Schönfeld − *Fraunhofer Institute for Applied Polymer Research IAP, 14476 Postdam, Germany*

Thorsten Pretsch − *Fraunhofer Institute for Applied Polymer Research IAP, 14476 Postdam, Germany*

Pavel Milkin − *Faculty of Engineering Sciences, University of Bayreuth, 95447 Bayreuth, Germany*

Complete contact information is available at:
https://pubs.acs.org/10.1021/acsami.2c01078

Author Contributions

The manuscript was written through contributions of all authors. All authors have given approval to the final version of the manuscript.

Notes

The authors declare no competing financial interest.

■ ABBREVIATIONS

PEU, poly(ester-urethane); MDI, 4,4′-diphenylmethane diisocyanate; BD, 1,4-butanediol; PBA, poly(1,4-butylene adipate); X_c, degree of crystallinity; DMA, dynamic mechanical analysis; DSC, differential scanning calorimetry; SEM, scanning electron microscopy; MEW, melt electrowriting; PLA, polylactic acid; GPU, graphic processing unit

■ REFERENCES

(1) Wang, J.; Gao, W.; Zhang, H.; Zou, M.; Chen, Y.; Zhao, Y. Programmable Wettability on Photocontrolled Graphene Film. *Science Advances* 2018, 4 (9), eaat7392.

(2) Zhan, S.; Pan, Y.; Gao, Z. F.; Lou, X.; Xia, F. Biological and Chemical Sensing Applications Based on Special Wettable Surfaces. *TrAC Trends in Analytical Chemistry* 2018, 108, 183−194.

(3) Tao, C.; Bai, S.; Li, X.; Li, C.; Ren, L.; Zhao, Y.; Yuan, X. Formation of Zwitterionic Coatings With an Aqueous Lubricating Layer for Antifogging/Anti-Icing Applications. *Prog. Org. Coat.* 2018, 115, 56−64.

(4) Yang, Z.; Wang, L.; Sun, W.; Li, S.; Zhu, T.; Liu, W.; Liu, G. Superhydrophobic Epoxy Coating Modified by Fluorographene Used for Anti-Corrosion and Self-Cleaning. *Appl. Surf. Sci.* 2017, 401, 146−155.

(5) Zhang, Z.; Ge, B.; Men, X.; Li, Y. Mechanically Durable, Superhydrophobic Coatings Prepared by Dual-Layer Method for Anti-Corrosion and Self-Cleaning. *Colloids Surf., A* 2016, 490, 182−188.

(6) Zhang, Z.; Shen, W.; Ling, J.; Yan, Y.; Hu, J.; Cheng, Y. The Fluorination Effect of Fluoroamphiphiles in Cytosolic Protein Delivery. *Nat. Commun.* 2018, 9 (1), 1377.

(7) Razavi, S. M. R.; Oh, J.; Haasch, R. T.; Kim, K.; Masoomi, M.; Bagheri, R.; Slauch, J. M.; Miljkovic, N. Environment-Friendly Antibiofouling Superhydrophobic Coatings. *ACS Sustainable Chem. Eng.* 2019, 7 (17), 14509−14520.

(8) Ma, C.; Zhang, W.; Zhang, G.; Qian, P.-Y. Environmentally Friendly Antifouling Coatings Based on Biodegradable Polymer and Natural Antifoulant. *ACS Sustainable Chem. Eng.* 2017, 5 (7), 6304−6309.

(9) Yu, C.; Sasic, S.; Liu, K.; Salameh, S.; Ras, R. H. A.; van Ommen, J. R. Nature-Inspired Self-Cleaning Surfaces: Mechanisms, Modelling, and Manufacturing. *Chem. Eng. Res. Des.* 2020, 155, 48−65.

(10) Chakraborty, M.; Weibel, J. A.; Schaber, J. A.; Garimella, S. V. The Wetting State of Water on a Rose Petal. *Advanced Materials Interfaces* 2019, 6 (17), 1900652.

(11) Han, D.-D.; Cai, Q.; Chen, Z.-D.; Li, J.-C.; Mao, J.-W.; Lv, P.; Gao, B.-R. Bioinspired Surfaces with Switchable Wettability. *Frontiers in Chemistry* 2020, 8, 692 DOI: 10.3389/fchem.2020.00692.

(12) Shin, S.; Seo, J.; Han, H.; Kang, S.; Kim, H.; Lee, T. Bio-Inspired Extreme Wetting Surfaces for Biomedical Applications. *Materials* 2016, 9 (2), 116.

(13) Kwon, D. H.; Huh, H. K.; Lee, S. J. Wettability and Impact Dynamics of Water Droplets on Rice (*Oryza sativa* L.) Leaves. *Experiments in Fluids* 2014, 55 (3), 1691.

(14) Wang, S.; Jiang, L. Definition of Superhydrophobic States. *Adv. Mater.* 2007, 19 (21), 3423−3424.

(15) Cheng, Z.; Zhang, D.; Luo, X.; Lai, H.; Liu, Y.; Jiang, L. Superwetting Shape Memory Microstructure: Smart Wetting Control and Practical Application. *Adv. Mater.* 2021, 33 (6), 2001718.

(16) Popova, A. A.; Schillo, S. M.; Demir, K.; Ueda, E.; Nesterov-Mueller, A.; Levkin, P. A. Droplet-Array (DA) Sandwich Chip: A Versatile Platform for High-Throughput Cell Screening Based on Superhydrophobic-Superhydrophilic Micropatterning. *Adv. Mater.* 2015, 27 (35), 5217−5222.

(17) Zhao, B.; MacMinn, C. W.; Juanes, R. Wettability Control on Multiphase Flow in Patterned Microfluidics. *Proc. Natl. Acad. Sci. U. S. A.* 2016, 113 (37), 10251.

(18) Dwyer, D. B.; Liu, J.; Gomez, J. C.; Tovar, T. M.; Davoodabadi, A.; Bernier, W. E.; DeCoste, J. B.; Jones, W. E. Metal Hydroxide/Polymer Textiles for Decontamination of Toxic Organophosphates: An Extensive Study of Wettability, Catalytic Activity, and the Effects of Aggregation. *ACS Appl. Mater. Interfaces* 2019, 11 (34), 31378−31385.

(19) Cao, R.; Zhang, X.; Tan, W.; Shen, W. Precipitation Assay Meets Low Wettability on Paper: A Simple Approach for Fabricating Patterned Paper Sensors. *Cellulose* 2018, 25 (1), 583−592.

(20) Minko, S.; Müller, M.; Motornov, M.; Nitschke, M.; Grundke, K.; Stamm, M. Two-Level Structured Self-Adaptive Surfaces with Reversibly Tunable Properties. *J. Am. Chem. Soc.* 2003, 125 (13), 3896−3900.

(21) Zhang, D.; Cheng, Z.; Kang, H.; Yu, J.; Liu, Y.; Jiang, L. A Smart Superwetting Surface with Responsivity in Both Surface Chemistry and Microstructure. *Angew. Chem., Int. Ed.* 2018, 57 (14), 3701−3705.

(22) Xu, G.; Neoh, K. G.; Kang, E.-T.; Teo, S. L.-M. Switchable Antimicrobial and Antifouling Coatings from Tannic Acid-Scaffolded Binary Polymer Brushes. *ACS Sustainable Chem. Eng.* 2020, 8 (6), 2586−2595.

(23) Chen, M.; Besenbacher, F. Light-Driven Wettability Changes on a Photoresponsive Electrospun Mat. *ACS Nano* 2011, 5 (2), 1549−1555.

(24) Shen, Y.; Li, G.; Ma, Y.; Yu, D.; Sun, J.; Li, Z. Smart Surfaces Based on Thermo-Responsive Polymer Brushes Prepared from L-Alanine Derivatives for Cell Capture and Release. *Soft Matter* 2015, 11 (38), 7502−7506.

(25) Guselnikova, O.; Postnikov, P.; Elashnikov, R.; Svorcik, V.; Lyutakov, O. Multiresponsive Wettability Switching on Polymer Surface: Effect of Surface Chemistry and/or Morphology Tuning. *Advanced Materials Interfaces* 2019, 6 (7), 1801937.

62

(26) Brannum, M. T.; Steele, A. M.; Venetos, M. C.; Korley, L. T. J.; Wnek, G. E.; White, T. J. Light Control with Liquid Crystalline Elastomers. *Advanced Optical Materials* **2019**, *7* (6), 1801683.

(27) Apsite, I.; Biswas, A.; Li, Y.; Ionov, L. Microfabrication Using Shape-Transforming Soft Materials. *Adv. Funct. Mater.* **2020**, *30* (26), 1908028.

(28) Feng, W.; Chu, L.; de Rooij, M. B.; Liu, D.; Broer, D. J. Photoswitching between Water-Tolerant Adhesion and Swift Release by Inverting Liquid Crystal Fingerprint Topography. *Advanced Science* **2021**, *8* (8), 2004051.

(29) Wang, J.-N.; Liu, Y.-Q.; Zhang, Y.-L.; Feng, J.; Sun, H.-B. Pneumatic Smart Surfaces With Rapidly Switchable Dominant And Latent Superhydrophobicity. *NPG Asia Materials* **2018**, *10* (2), e470–e470.

(30) Wang, Y.; Lai, H.; Cheng, Z.; Zhang, H.; Liu, Y.; Jiang, L. Smart Superhydrophobic Shape Memory Adhesive Surface toward Selective Capture/Release of Microdroplets. *ACS Appl. Mater. Interfaces* **2019**, *11* (11), 10988–10997.

(31) Shao, Y.; Zhao, J.; Fan, Y.; Wan, Z.; Lu, L.; Zhang, Z.; Ming, W.; Ren, L. Shape Memory Superhydrophobic Surface with Switchable Transition Between "Lotus Effect" to "Rose Petal Effect. *Chemical Engineering Journal* **2020**, *382*, 122989.

(32) Joyee, E. B.; Szmelter, A.; Eddington, D.; Pan, Y. Magnetic Field-Assisted Stereolithography for Productions of Multimaterial Hierarchical Surface Structures. *ACS Appl. Mater. Interfaces* **2020**, *12* (37), 42357–42368.

(33) Chen, Y.; Wang, H.; Yao, Q.; Fan, B.; Wang, C.; Xiong, Y.; Jin, C.; Sun, Q. Biomimetic Taro Leaf-Like Films Decorated on Wood Surfaces Using Soft Lithography for Superparamagnetic and Superhydrophobic Performance. *J. Mater. Sci.* **2017**, *52* (12), 7428–7438.

(34) Kumar, A.; Gogoi, B. Development of Durable Self-Cleaning Superhydrophobic Coatings for Aluminium Surfaces Via Chemical Etching Method. *Tribol. Int.* **2018**, *122*, 114–118.

(35) van Dommelen, R.; Fanzio, P.; Sasso, L. Surface Self-Assembly of Colloidal Crystals for Micro- and Nano-Patterning. *Adv. Colloid Interface Sci.* **2018**, *251*, 97–114.

(36) Lv, T.; Cheng, Z.; Zhang, D.; Zhang, E.; Zhao, Q.; Liu, Y.; Jiang, L. Superhydrophobic Surface with Shape Memory Micro/Nanostructure and Its Application in Rewritable Chip for Droplet Storage. *ACS Nano* **2016**, *10* (10), 9379–9386.

(37) Li, J.; Wang, W.; Mei, X.; Pan, A. Effects of Surface Wettability on the Dewetting Performance of Hydrophobic Surfaces. *ACS Omega* **2020**, *5* (44), 28776–28783.

(38) Lai, H.; Shang, Y.; Cheng, Z.; Lv, T.; Zhang, E.; Zhang, D.; Wang, J.; Liu, Y. Control of Tip Nanostructure on Superhydrophobic Shape Memory Arrays Toward Reversibly Adjusting Water Adhesion. *Advanced Composites and Hybrid Materials* **2019**, *2* (4), 753–762.

(39) Wang, Z.; Hansen, C.; Ge, Q.; Maruf, S. H.; Ahn, D. U.; Qi, H. J.; Ding, Y. Programmable, Pattern-Memorizing Polymer Surface. *Adv. Mater.* **2011**, *23* (32), 3669–3673.

(40) Wu, H.; Zhang, R.; Sun, Y.; Lin, D.; Sun, Z.; Pan, W.; Downs, P. Biomimetic Nanofiber Patterns with Controlled Wettability. *Soft Matter* **2008**, *4* (12), 2429–2433.

(41) Fischer, S. C. L.; Hillen, L.; Eberl, C. Mechanical Metamaterials on the Way from Laboratory Scale to Industrial Applications: Challenges for Characterization and Scalability. *Materials* **2020**, *13* (16), 3605.

(42) Specht, M.; Berwind, M.; Eberl, C. Adaptive Wettability of a Programmable Metasurface. *Adv. Eng. Mater.* **2021**, *23* (2), 2001037.

(43) Walter, M.; Friess, F.; Krus, M.; Zolanvari, S. M.; Grün, G.; Kröber, H.; Pretsch, T. Shape Memory Polymer Foam with Programmable Apertures. *Polymers* **2020**, *12* (9), 1914.

(44) Schönfeld, D.; Chalissery, D.; Wenz, F.; Specht, M.; Eberl, C.; Pretsch, T. Actuating Shape Memory Polymer for Thermoresponsive Soft Robotic Gripper and Programmable Materials. *Molecules* **2021**, *26* (3), 522.

(45) Chalissery, D.; Schönfeld, D.; Walter, M.; Shklyar, I.; Andrae, H.; Schwörer, C.; Amann, T.; Weisheit, L.; Pretsch, T. Highly

(46) Gatti, F.; Amann, T.; Kailer, A.; Baltes, N.; Rühe, J.; Gumbsch, P. Towards Programmable Friction: Control of Lubrication with Ionic Liquid Mixtures by Automated Electrical Regulation. *Sci. Rep.* **2020**, *10* (1), 17634.

(47) Dalton, P. D. Melt Electrowriting with Additive Manufacturing Principles. *Current Opinion in Biomedical Engineering* **2017**, *2*, 49–57.

(48) Paxton, N. C.; Daley, R.; Forrestal, D. P.; Allenby, M. C.; Woodruff, M. A. Auxetic Tubular Scaffolds via Melt Electrowriting. *Materials & Design* **2020**, *193*, 108787.

(49) Kade, J. C.; Dalton, P. D. Polymers for Melt Electrowriting. *Adv. Healthcare Mater.* **2021**, *10* (1), 2001232.

(50) Hochleitner, G.; Fürsattel, E.; Giesa, R.; Groll, J.; Schmidt, H.-W.; Dalton, P. D. Melt Electrowriting of Thermoplastic Elastomers. *Macromol. Rapid Commun.* **2018**, *39* (10), 1800055.

(51) Uribe-Gomez, J.; Posada-Murcia, A.; Shukla, A.; Ergin, M.; Constante, G.; Apsite, I.; Martin, D.; Schwarzer, M.; Caspari, A.; Synytska, A.; Salehi, S.; Ionov, L. Shape-Morphing Fibrous Hydrogel/Elastomer Bilayers Fabricated by a Combination of 3D Printing and Melt Electrowriting for Muscle Tissue Regeneration. *ACS Applied Bio Materials* **2021**, *4* (2), 1720–1730.

(52) Liashenko, I.; Hrynevich, A.; Dalton, P. D. Designing Outside the Box: Unlocking the Geometric Freedom of Melt Electrowriting using Microscale Layer Shifting. *Adv. Mater.* **2020**, *32* (28), 2001874.

(53) Ionov, L.; Stoychev, G.; Jehnichen, D.; Sommer, J. U. Reversibly Actuating Solid Janus Polymeric Fibers. *ACS Appl. Mater. Interfaces* **2017**, *9* (5), 4873–4881.

(54) Stoychev, G.; Razavi, M. J.; Wang, X.; Ionov, L. 4D Origami by Smart Embroidery. *Macromol. Rapid Commun.* **2017**, *38* (18), 1700213.

(55) Abouzahr, S.; Wilkes, G. L. Structure Property Studies of Polyester- and Polyether-Based MDI-BD Segmented Polyurethanes: Effect of One- vs. Two-Stage Polymerization Conditions. *J. Appl. Polym. Sci.* **1984**, *29* (9), 2695–2711.

(56) Li, F.; Hou, J.; Zhu, W.; Zhang, X.; Xu, M.; Luo, X.; Ma, D.; Kim, B. K. Crystallinity and Morphology of Segmented Polyurethanes with Different Soft-Segment Length. *J. Appl. Polym. Sci.* **1996**, *62* (4), 631–638.

(57) Pretsch, T.; Jakob, I.; Müller, W. Hydrolytic Degradation and Functional Stability of a Segmented Shape Memory Poly(Ester Urethane). *Polym. Degrad. Stab.* **2009**, *94* (1), 61–73.

(58) Hojabri, L.; Jose, J.; Leao, A. L.; Bouzidi, L.; Narine, S. S. Synthesis and Physical Properties of Lipid-Based Poly(ester-urethane)s, I: Effect of Varying Polyester Segment Length. *Polymer* **2012**, *53* (17), 3762–3771.

(59) Bothe, M.; Emmerling, F.; Pretsch, T. Poly(ester urethane) with Varying Polyester Chain Length: Polymorphism and Shape-Memory Behavior. *Macromol. Chem. Phys.* **2013**, *214* (23), 2683–2693.

(60) Debuissy, T.; Pollet, E.; Avérous, L. Synthesis of Potentially Biobased Copolyesters Based on Adipic Acid and Butanediols: Kinetic Study Between 1,4- and 2,3-Butanediol and Their Influence on Crystallization and Thermal Properties. *Polymer* **2016**, *99*, 204–213.

(61) Fritzsche, N.; Pretsch, T. Programming of Temperature-Memory Onsets in a Semicrystalline Polyurethane Elastomer. *Macromolecules* **2014**, *47* (17), 5952–5959.

(62) Mirtschin, N.; Pretsch, T. Designing Temperature-Memory Effects in Semicrystalline Polyurethane. *RSC Adv.* **2015**, *5* (57), 46307–46315.

(63) Adam, N.; Franke, F.; Aland, S. A Simple Parallel Solution Method for the Navier-Stokes Cahn-Hilliard Equations. *Mathematics* **2020**, *8* (8), 1224.

(64) Aland, S.; Auerbach, P. A Ternary Phase-Field Model for Wetting of Soft Elastic Structures. *International Journal for Numerical Methods in Engineering* **2021**, *122* (16), 4114–4128.

(65) Aland, S.; Lowengrub, J.; Voigt, A. Two-Phase Flow in Complex Geometries: A Diffuse Domain Approach. *Comput Model Eng Sci* **2010**, *57* (1), 77–106.

63

(66) Py, C.; Reverdy, P.; Doppler, L.; Bico, J.; Roman, B.; Baroud, C. N. Capillary Origami: Spontaneous Wrapping of a Droplet with an Elastic Sheet. *Phys. Rev. Lett.* **2007**, *98* (15), 156103.

(67) Chen, C.-M.; Yang, S. Directed Water Shedding on High-Aspect-Ratio Shape Memory Polymer Micropillar Arrays. *Adv. Mater.* **2014**, *26* (8), 1283−1288.

(68) Uribe-Gomez, J.; Posada-Murcia, A.; Shukla, A.; Alkhamis, H.; Salehi, S.; Ionov, L. Soft Elastic Fibrous Scaffolds for Muscle Tissue Engineering by Touch Spinning. *ACS Applied Bio Materials* **2021**, *4* (7), 5585−5597.

Supporting Information

Smart Mechanically Tunable Surfaces With Shape Memory Behavior And Wetting-Programmable Topography

Gissela Constante[1], Indra Apsite[1], Paul Auerbach[2], Sebastian Aland[2,3], Dennis Schönfeld[4], Thorsten Pretsch[4], Pavel Milkin[1] and Leonid Ionov[1, 5*]

[1] Faculty of Engineering Sciences, University of Bayreuth, Ludwig Thoma Str. 36A, 95447 Bayreuth, Germany

[2] Fakultät Informatik/Mathematik, Hochschule für Technik und Wirtschaft Dresden, 01069 Dresden, Germany

[3] Fakultät Mathematik und Informatik, Technische Universität Bergakademie Freiberg, 09599 Freiberg, Germany

[4] Fraunhofer Institute for Applied Polymer Research IAP, Geiselbergstr. 69, 14476 Postdam, Germany

[5] Bavarian Polymer Institute, University of Bayreuth, 95447 Bayreuth, Germany.

[*] E-mail: leonid.ionov@uni-bayreuth.de

S-1
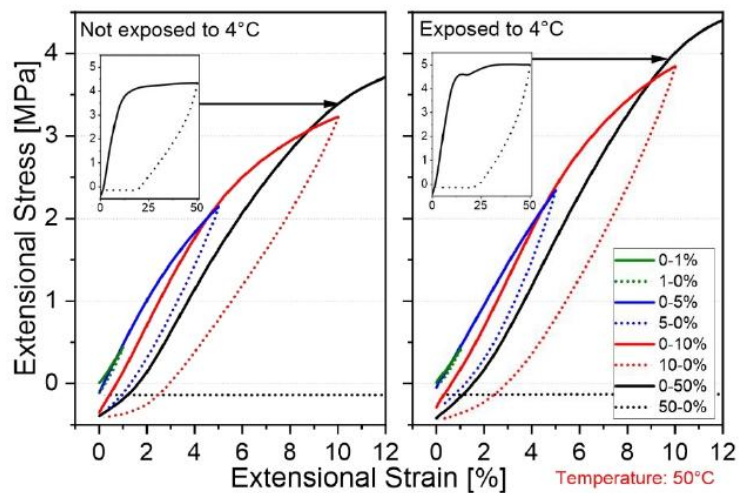
Figure S1. Stress-strain curve for TPU PBA-25 when it is exposed and not exposed to 4°C. Measurements made at 50°C.

On difference of **Figure 1c,** the plot was made for the polymer exposed and not exposed to low temperatures, and it was measured at 50 ˚C. In **Figure 1c,** the polymer was measured at 50 and 70 ˚C when was not exposed to 4 ˚C.

S-2

66

Table S1. Young's modulus calculated for each curve at different temperature.

Temperature of measurement	Strain curve	Exposed to 4°C	Young's Modulus
70 °C	0-1%	No	8 ± 1 MPa
70 °C	0-5%	No	9.8 ± 0.5 MPa
70 °C	0-10%	No	9.4 ± 0.9 MPa
70 °C	0-50%	No	9 ± 2 MPa
50 °C	0-1%	No	45.7 ± 0.8 MPa
50 °C	0-5%	No	51 ± 7 MPa
50 °C	0-10%	No	52 ± 4 MPa
50 °C	0-50%	No	42 ± 4 MPa
50 °C	0-1%	Yes	41 ± 2 MPa
50 °C	0-5%	Yes	49.6 ± 0.6 MPa
50 °C	0-10%	Yes	57 ± 2 MPa
50 °C	0-50%	Yes	52 ± 2 MPa
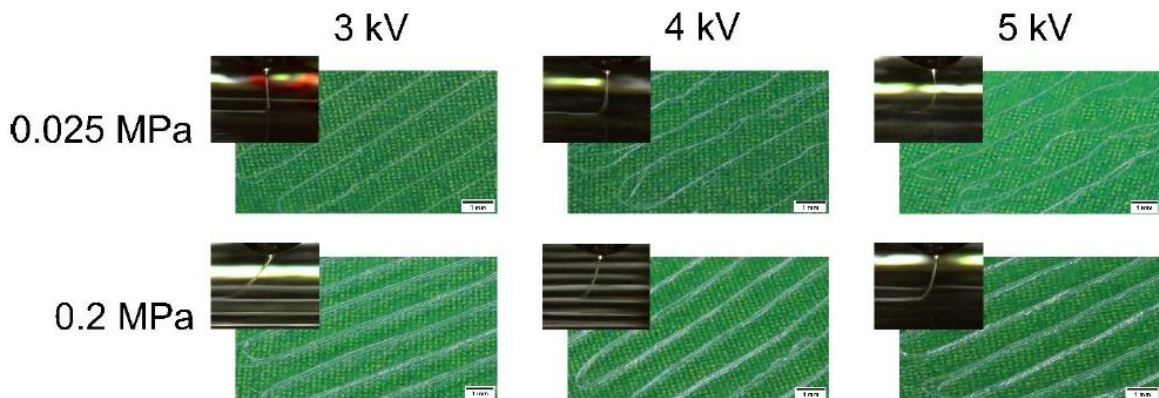
Figure S2. Study of the effect of the voltage and pressure in the fiber deposition by MEW.
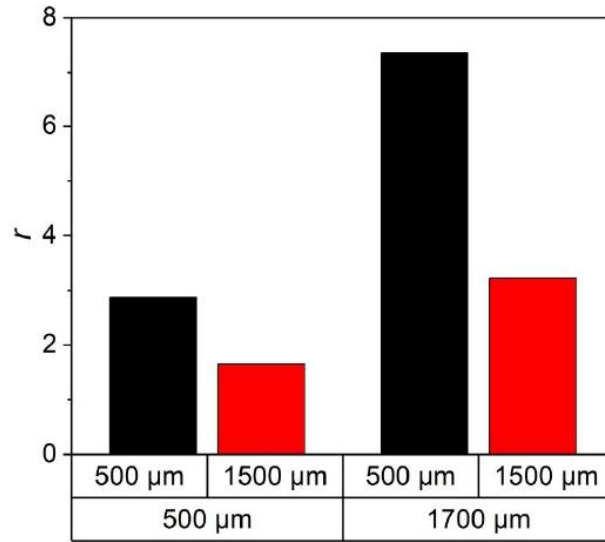
Figure S3. Roughness coefficient calculated for the topographical surfaces
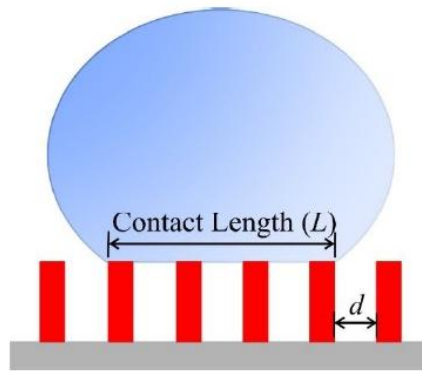
Figure S4. Scheme of the droplet on the lamellae showing the contact length (*L*) and distance between the lamellas (*d*).

S-4
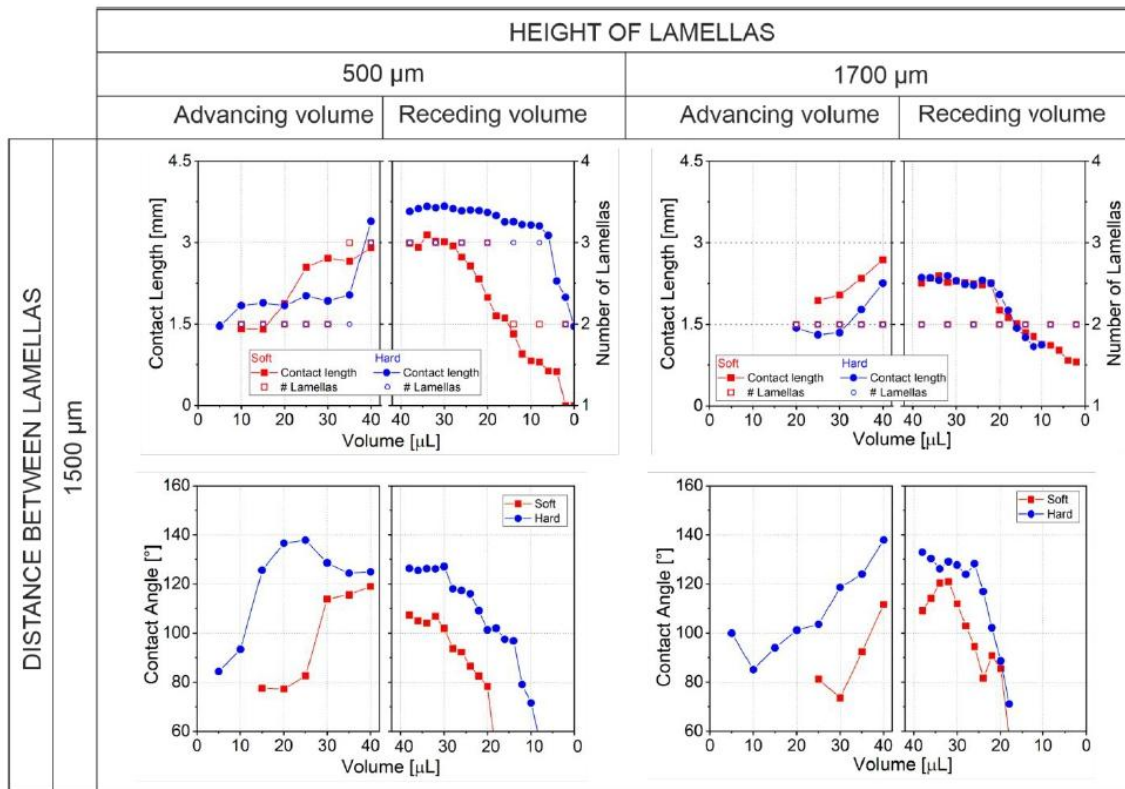
Figure S5. Measured contact angle (CA), contact length and number of lamellae by advancing and receding the volume of the droplet under different aspect ratio of the lamellas and high distance between lamellae.

9.2.Publication 2

Reversibly Photoswitchable High-Aspect Ratio Surfaces

Gissela Constante, Indra Apsite, Dennis Schönfeld, Thorsten Pretsch, and Leonid Ionov

Reversibly Photoswitchable High-Aspect Ratio Surfaces

Gissela Constante, Indra Apsite, Dennis Schönfeld, Thorsten Pretsch, and Leonid Ionov*

Herein, the fabrication of light-sensitive high-aspect ratio surfaces with switchable topography using melt-electrowriting of shape-memory polymers and deposition of light-to-heat converting black ink on it by dip coating is reported on. The lamellae exposed to low temperatures are hard and cannot be deformed by water droplets. The temperature reached upon illumination of surfaces is close to the melting point of the soft segment of the polyurethane that leads to softening of the polymer. Due to this, it is possible to locally deform and recover the light-softened surface structures by water droplets deposited on lamellae. The deformed state can be fixed by cooling down resulting in the crystallization of the polymer. Thus, the reversibility of local deformation can be achieved. Finally, the application of the developed approach and materials for the fabrication of smart light-controlled valves is demonstrated, which can be used for the controlled mixing of fluids in microfluidic devices.

1. Introduction

Flat (2D), curved (3D), and hierarchical (3D) surfaces with dynamic topography attract rising interest due to their growing potential in medicine,[1] biotechnology,[2] electronics,[3] robotics,[4] and design of actuators,[5] among others. The reshaping of the 2D surfaces or transformation of 3D surfaces in other 3D surfaces is usually triggered by either a physical or chemical stimulus, which can affect surfaces in two different ways: by changing the topography and/or by changing the chemical composition of the surface.[6] The change in the topography can be, for example, achieved by the action of a mechanical force (physical stimuli)[7]

G. Constante, I. Apsite, L. Ionov
Faculty of Engineering Sciences
University of Bayreuth
Ludwig Thoma Str. 36A, 95447 Bayreuth, Germany
E-mail: leonid.ionov@uni-bayreuth.de

D. Schönfeld, T. Pretsch
Shape Memory Polymers Group
Synthesis and Polymer Technology
Fraunhofer Institute for Applied Polymer Research IAP
Geiselbergstr. 69, 14476 Potsdam, Germany

L. Ionov
Bavarian Polymer Institute
University of Bayreuth
95447 Bayreuth, Germany

(iD) The ORCID identification number(s) for the author(s) of this article can be found under https://doi.org/10.1002/sstr.202300040.

or by applying any other stimuli such as light or temperature leading to bending, stretching, or compressing of micro- and nanostructures.[8]

The materials that can switch one or more properties in response to applied stimuli are known as "smart" materials. Smart materials convert one form of energy like thermal, electrical, chemical, or mechanical into another form.[9] Two-way transformation is usually achieved using hydrogels, electroactive polymers, and liquid crystalline elastomers.[10] Traditional shape-memory polymers (SMPs) allow only one-way shape transformation (relaxation from temporary shape to permanent one). The transformation to a temporary shape is usually achieved manually. SMPs can also be used for the design of surfaces with switchable topography,[11] although their manual deformation to temporary states is unavoidable.[12]

The shape-changing of SMPs is driven by the release of inner stress triggered by external stimuli like an increase in temperature.[13] Although thermoresponsive SMPs have a high recovery ratio, up to 100%, their local actuation is challenging because of the difficulty of local heating. The light as a signal can solve these problems of local triggering because local illumination is very straightforward. Moreover, light-responsive materials allowed remote activation, temporal control, and rapid switching.[14] Light-responsive materials actuate in different modes: 1) the first one by changing the conformational structure of photochromic groups (photochemically), for example, spiropyrans and azobenzenes;[15] 2) the second one by elevating the excitation level of the photochromic groups;[16] and 3) the third one by the transformation of light energy into heat known as a photothermal effect.[15,17] Photothermal effect allows local heating of, for example, polymers above their glass transition and/or melting temperature and, as follows, allows their local softening.[18] The typical photothermal materials, which absorb light and convert it into heat,[19] are carbon nanomaterials, gold nanomaterials, indocyanine green, and metallic sulfides/oxides.[20] The use of photothermal effects is in many cases more preferential because it allows separate tuning of properties of the thermoresponsive matrix and light-sensitive (photothermal) agents. An example of the application of the photothermal effect was observed in the control of light-responsive hydrogel valves used in microfluidic devices.[21] Another interesting example of a photothermal-responsive surface is presented by Jiao et al.[22] In their investigation, an anisotropic grooved surface composed of graphene and polyvinylidene coated with paraffin was created to control the droplet sliding. By the photothermal stimuli, the topographical surface is modified to manipulate the water drop,

**ADVANCED
SCIENCE NEWS**
www.advancedsciencenews.com

**small
structures**
www.small-structures.com

either pinning or sliding, effect used for the fabrication of anti-icing surfaces.[22]

In our previous work, we demonstrate an approach for the fabrication of surfaces with switchable high-aspect ratio lamellae based on SMPs using melt-electrowriting (MEW).[23] The mechanical properties of the lamellae can be switched between soft and hard states. The high-aspect ratio lamellae demonstrated possibilities to switch their shape by surface tension of the water and temperature, and manual deformation was not required. The temperature as a signal, used in our previous work,[23] can hardly be applied locally to achieve targeted switching of mechanical and wetting properties of surfaces. Using light as a signal presents more benefits. In this article, we have taken a step forward in designing high-aspect ratio surfaces with switchable topography and made them light-sensitive, which we expect should allow local manipulation with topography and wetting. The dip coating as the selected method for converting the lamellar surface into a photoresponsive is advantageous because it is simple, efficient, and inexpensive, and as the particles are not embedded into the molten polymer, the rheological properties and printing conditions are not affected.

2. Results and Discussion

The high-aspect ratio light-sensitive surfaces were fabricated using a two-step approach (**Figure 1**). First, lamellae of shape-memory poly(1,4-butylene adipate)-based polyurethane (TPU PBA-75) copolymer were deposited on a glass substrate using MEW (Figure 1a). In the second step, a layer of black light-absorbing ink was deposited on the top of the lamellae (Figure 1b). The use of two-step approach has essential advantages over the approach of light-absorbing material, which is usually carbon, iron oxide, or similar black particles, is mixed into the polymer and the polymer–particle blend is then deposited. In fact, it is known that particles are able to substantially change the rheological behavior of polymer melts, in particular when the particles tend to aggregate. The aggregated particles render
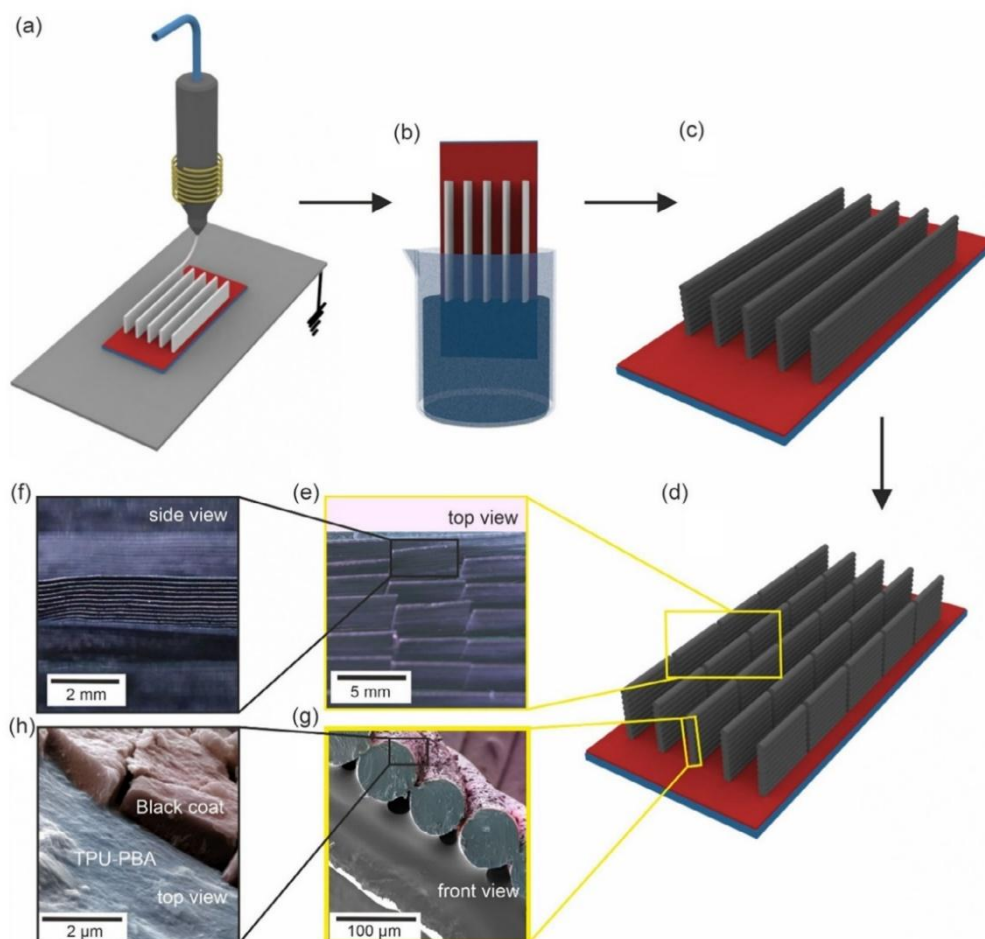
Figure 1. Scheme of fabrication of photosensitive structured surfaces with high-aspect ratio lamellae: a) fabrication of TPU-PBA lamellae using MEW; b) deposition of light-absorbing material on the lamellae using dip coating to form light-sensitive surfaces; c,d) the lamellae may be cut to reduce their length and form short flaps to increase the amplitude of actuation; e,f) optical imaging made with a macrocamera, and g,h) SEM of the surface of the black-coated lamella (pink color: black coating, blue color: polymeric fiber).

**ADVANCED
SCIENCE NEWS**

www.advancedsciencenews.com

**small
structures**

www.small-structures.com

the polymer's flow behavior with flow threshold points.[24] Such blends show elastic behavior over a very broad time-scale range and nearly do not flow when small stress is applied. The blends start to flow when the stress above a threshold value is applied.[24] Such kind of behavior makes the control of the flow behavior of polymers difficult. Therefore, in order to avoid these difficulties, we used a two-step approach—deposited polymer first and light-absorbing material next. Another advantage of this approach is that amount of light-absorbing material can be easily controlled in two ways: by its concentration in dispersion/solution and by varying the number of layers, which are deposited. On the contrary, the use of a one-step approach will require making new blends each time when the amount of light-absorbing material shall be varied. Thus, the main advantages of the use of a two-step fabrication approach are flexibility from point of view of fabrication of a variety of structures with different compositions and properties.

We have used poly(1,4-butylene adipate)-based polyurethane. The thermoresponsive polyurethane had a hard segment formed by the reaction between 4,4′-diphenylmethane diisocyanate (MDI) and 1,4-butanediol (BD). The soft segment was composed of poly(1,4-butylene adipate) (PBA). The soft segment possesses a melting peak temperature of around 40 °C and a crystallization onset temperature of 5 °C when applying a heating/cooling rate of 5 °C min^{-1} (Figure S1a, Supporting Information). Cold crystallization in second heating cycle disappears at lower scan rate because conditions are closer to equilibrium and chains have enough time to crystallization upon cooling that is evidenced by higher crystallization enthalpy in cooling cycle (Figure S1a, b, Supporting Information).

The mechanical properties of the polymer showed that the material can be in two states: hard and soft depending on the temperature. The elastic modulus in the hard state is 55 MPa approximately and in the soft state 8 MPa.[23] The low melting point of the mobile phase of poly(ester urethane) (PEU) can be easily attainable after few seconds of light exposure. As well, from the point of view of the mechanical properties, the PEU lamellar construct can be deformed by small forces as in the addition of water drop, eliminating the need of manual deformation.

The thickness of lamellae is determined by conditions of MEW ($V = 3$ kV, 200 μm of nozzle diameter, at 215 °C temperature and 2 mm distance from the electrified collector). The viscosity of the polymer decreased at a temperature over 200 °C as measured in the frequency sweep at a constant strain (5%) (Figure S3, Supporting Information) and by rotational rheology (Figure S4, Supporting Information) which shows the flowability of the polymer at 215 °C. The storage and loss moduli curves showed that the polymer starts to flow at temperatures higher than 180 °C as observed in Figure S2, Supporting Information. For the dip coating solution, we used commercial black ink as light-absorbing material—Edding T100 (Ahrensburg, Germany). The reasons for the selection of this material are the following: 1) it has a high extinction coefficient in a whole range of visible light (the material is very black even if the thickness of the layer is small); 2) it forms stable dispersion. The measured thickness of the coating was 0.9 ± 0.1 μm (Figure 1g,h) as it was measured using scanning electronic microscopy (SEM). This behavior is, however, expected in all kinds of inorganic granular materials —contact between particles is weak and breaks at low strain. After 5 and 10 cycles of deformation, the samples were analyzed by SEM (Figure S5, Supporting Information). It was observed that the black coating was stable; nevertheless, after 10 cycles of deformation, the coating formed few cracks on the surface of the polymeric lamella.

Next, we investigated the mechanical properties of coated lamellae to explain the effect of light-absorbing coating and light stimulation. First, cyclic extensional strain testing was performed to elucidate the properties of materials at relatively large deformation up to $\varepsilon = 25\%$ (**Figure 2**a). Young's modulus of the uncoated ("white") lamella was measured to be 49 ± 9 MPa. Exposure to light results in the decrease of the modulus down to 25 ± 3 MPa, which is explained by the increase of temperature of the material due to the photothermal effect and its softening due to melting of poly(1,4-butylene adipate) block—even white materials are able to absorb light which results in their softening. Young's modulus for the coated ("black") lamella with and without light exposure was 42 ± 2 and 6 ± 1 MPa, respectively (Figure 2a). The drop in Young's modulus is due to the melting
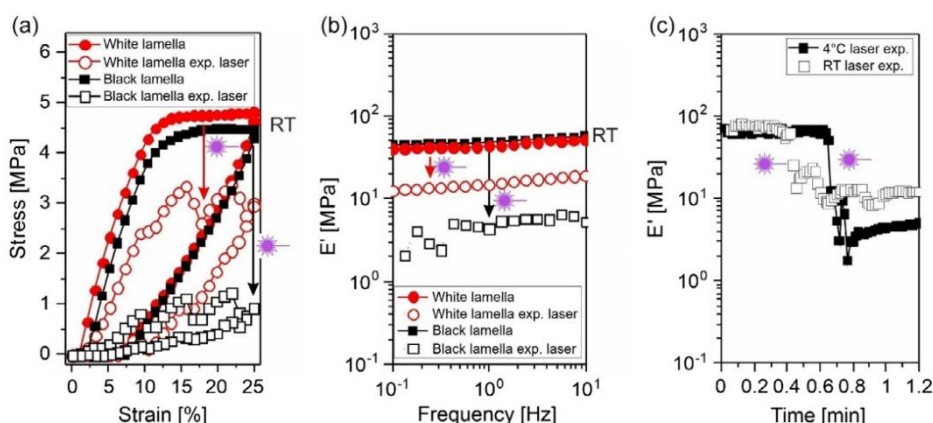
Figure 2. Mechanical characterization of the lamellae noncoated (white lamella) and coated with black ink (black lamella): a) a cyclic strain dynamic mechanical characterization ($\varepsilon_{max} = 25\%$) exposed and not exposed to light; b) frequency sweep characterization of lamella exposed and not exposed to light and coated and not coated with black ink; c) storage moduli of the black lamella when exposed to 4 °C and kept at RT.

of the soft segment of the polymer. The obtained values of Young's modulus of nonexposed lamellae with and without black coating allow a conclusion that the black coating does not affect Young's modulus of the lamella—contribution of thin and brittle particle layer to mechanical properties is negligible. On the other hand, black coating significantly improved the light sensitivity of polymer lamellae and allows manipulation of its mechanical properties by light.

An extensional frequency sweep was performed to characterize the mechanical properties of the lamellae at different time scales (Figure 2b). It was found that storage modulus dominates over loss modulus for the coated lamellae, which were exposed to light (Figure S6, Supporting Information). Therefore, the values of loss moduli are not shown. It was found that the storage modulus decreases tenfold from 49.1 to 4.7 MPa when the coated lamella was exposed to light (Table S1, Supporting Information). The storage modulus of uncoated lamellae decreases from 44.6 to 15.5 MPa which is 3 times lower than that in the case of coated lamellae. As mentioned above, this is explained by the inherent heat produced by light. Nevertheless, the storage modulus was still higher than that obtained when the material was exposed to 40 °C (8 MPa).[23] We did not observe any frequency dependence of storage modulus for coated and uncoated samples, which were exposed and not exposed to light. This means that softening of the polymer does not result in the appearance of a relaxation process on the investigated time scale.

In the third experiment, we studied the rate of softening of the polymer upon exposure to light (Figure 2c). We tested two kinds of lamellae: one, which was kept at room temperature (RT), and one, which was exposed to 4 °C to induce stronger crystallization. It was found that illumination with light resulted in the drop of Young's modulus on a time scale of a few seconds independent of how the sample was treated. This observation shows that softening of lamellae is a fast process. The mechanical tests clearly showed that the mechanical properties of coated lamellae can be manipulated by light and that softening of the polymer is very quick.

We studied the photothermal shape-memory behavior (deformation, fixation, and recovery) of the lamellae (**Figure 3**). First, the crystallized lamella was stretched by applying stress $\sigma = 5$ MPa which resulted in their elongation by $\varepsilon = 3\%$. Then, the stressed lamella was exposed to light which resulted in its deformation by $\varepsilon = 80\%$. The whole stretching process took

≈ 200 s that is because illumination was local and heating of the whole lamella takes a certain time. The shape fixation was performed by pouring liquid nitrogen vapor onto the sample in a stretched state. After that, the stress was released ($\sigma = 0$ MPa), and the strain was reduced to 73% due to the partial relaxation of the polymer chains. Nearly full shape recovery was achieved upon light exposure for 3 min. The final strain of the recovered sample was 3%. This experiment showed the possibility of photothermal actuation and thermal fixation of coated lamellae.

We studied the deformation of the coated lamella and flaps (5 mm long parts of lamella obtained by cutting) (**Figure 4**) by water droplet before and after illumination with light to investigate the interplay between surface tension and elastic forces. The nonilluminated lamella/flap could not be deformed by both advancing and receding water droplets. The lamella/flap was then exposed to light for 5 min to make it soft (Figure 4c,d), and then the surface temperature was set at 20 °C. The water droplet was deposited between lamellae/flaps (advancing droplet) which caused their deformation in the direction opposite to each other. Afterward, the droplet was soaked back (receding droplet) into the pipet to reduce its volume. Surface tension forces forced lamellae to bend toward each other. These findings show that the short flap experienced greater deformation (3.13 ± 0.7 mm) when exposed to light and advancing volume of water (Figure 4e). However, the difference between deformation of the continuous lamella and that of the short flap, when both were exposed to 4 °C before the deformation (which resulted in hard mechanical memory) or when they were exposed to light (resulting in soft mechanical memory), was found to be not significant. We also estimated the degree of deformation of the short flaps after the water volume was receded. Results showed that the maximum deformation of the short flaps that were exposed to light is 1.05 ± 0.2 mm. These findings confirm that lamellae can indeed be deformed at RT after exposure to light, and that once the stress is eliminated, the lamellae can recover their original position. This experiment showed that the sensitivity of coated lamellae to surface tension forces generated by water droplets can be switched by light.

The recovery of lamellae depends on their length. In order to investigate this phenomenon, we manually deformed heated long lamellae and then cooled them down to fix them in a temporary state. The recovery was induced by exposing lamellae to light. The recovery was measured in two areas of the surface: in
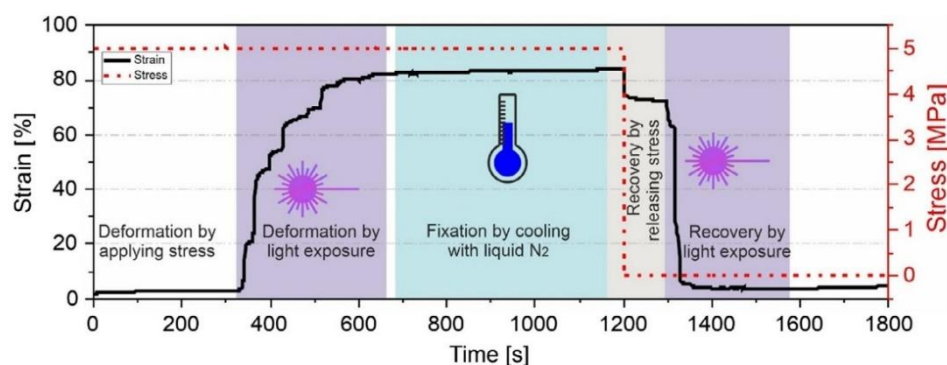

Figure 3. Photothermal shape-memory behavior of the black lamellae measured in dynamic mechanical analyzer at a constant stress ($\sigma = 5$ MPa) during deformation and $\sigma = 0$ MPa for recovery.
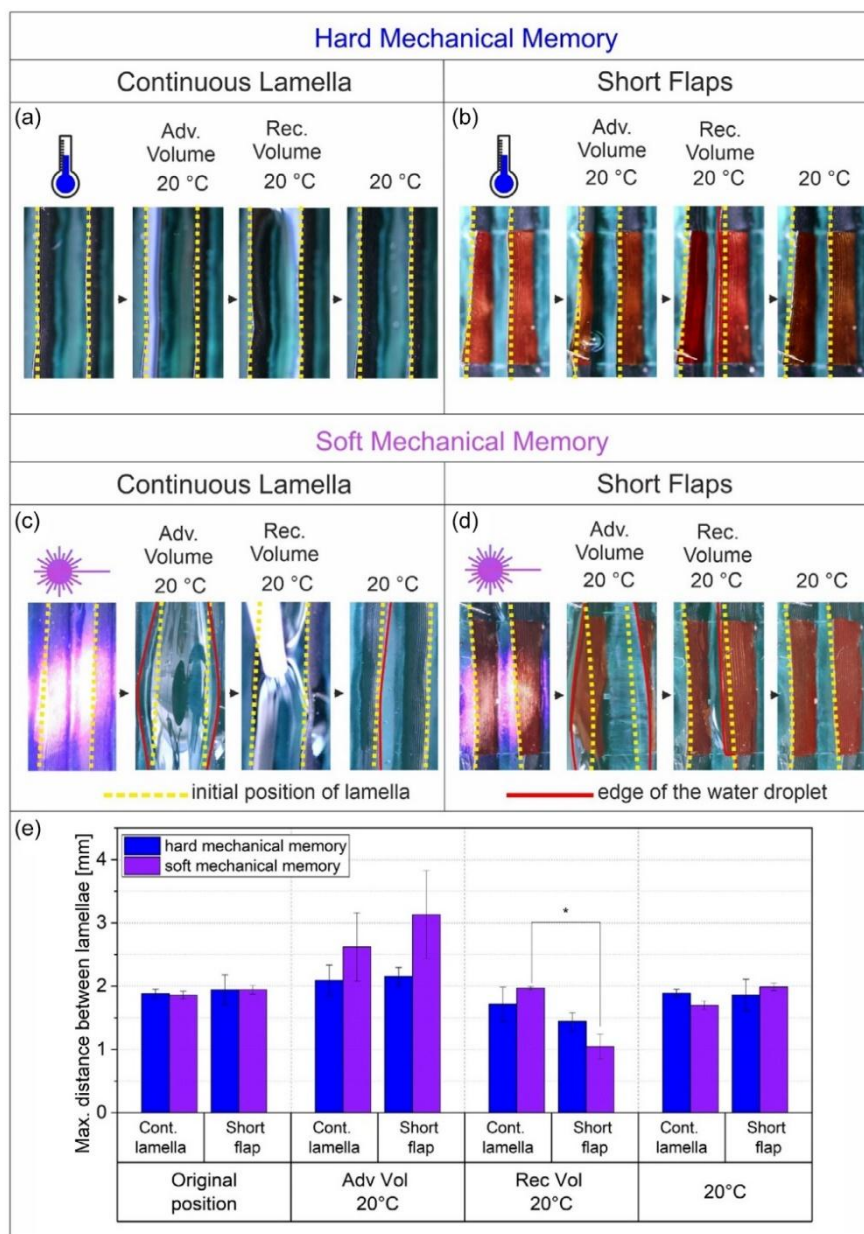
Figure 4. Deformation of the lamellae (left column a,c) and short flaps (right column b,d) exposed to 4 °C (hard state, upper panel (a) and (b)) and illuminated before deformation (soft state, lower panel, (c) and (d)). Dashed yellow line—lamella in the initial state, red line—edge of the water droplet after deformation. The short flaps were colored in red to facilitate the visualization. (e) Maximum distance measured between the lamellae. (* at the 0.05 level, there is a significant difference in the means) (ANOVA and Tukey test at $p = 0.05$; $n = 2$).

the center of the lamella and at the edges (**Figure 5**). It was observed that the recovery of the central part of lamella occurred within 600 s of light exposure was 21%, while the recovery of the edges reached 28% in 10 s of exposure. The reason for this difference is the inhomogeneous heating of the sample surface by light (Figure 5d). Indeed, complete recovery is only possible when the whole lamella is heated—hard nonilluminated part of lamellae oppose deformation. Heating of a fraction of lamella does not result in the recovery of even heated areas—the structure behaves as a beam with two fixed ends. The edge of the lamella is, however, "fixed" at one of its ends, which is the long lamella. As result, its recovery is large. This observation indicates that a large recovery can be achieved when the whole lamella is illuminated which can be realized by the use of a large and

75
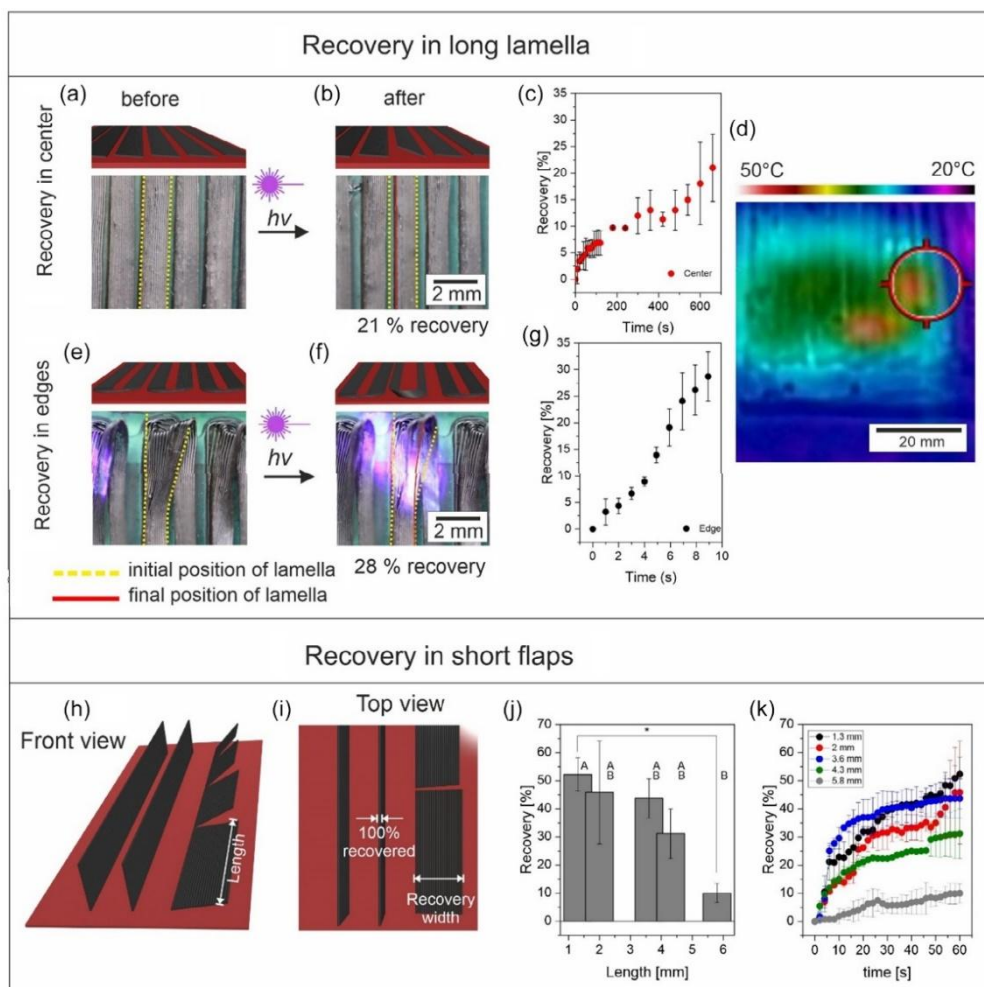
Figure 5. Studies of the efficiency of recovery of lamellae depending on their length: a–c) central part of lamellae is illuminated; e–g) edges of the lamella are illuminated; d) photothermal photography of the exposed areas to light. Yellow dashed line—initial position of the lamella, red line—final position of lamella after restoring: h,i) front and top view of the lamellae flaps at different length; j) achieved recovery after 60 s of light exposure while varying the length of the flap; and k) the recovery curve for flaps of different length.

sufficiently powerful laser beam or by the use of short lamellae. Moreover, in order to determine the efficiency of recovery of the short flaps, we cut the lamellae in different lengths: 1.3, 2, 3.6, 4.3, and 5.8 mm, and measured the width of the flap (Figure 5i) at different times during light exposure (Figure 5k). A fast recovery of the flap was observed at small lengths. After 60 s of exposure, a maximum of 52% of recovery was observed for flaps of 1.3 mm. There is a statistical difference of the recovery percentage between the flaps of 1.3 and 5.8 mm length at a significance of 95% (Figure 5j).

As discussed in our previous article,[23] it is evidenced that the surface tension ($F_s \approx \gamma \cdot dl$),[25] elastic deformation ($\delta \approx F \cdot H^3 / EI$, where H is the height of lamella, I is the second moment of inertia $I = a \cdot dl^3 / 12$, a is the thickness of a lamella, and dl is its length), and gravity ($F_g \approx \rho \cdot g \cdot h \cdot b \cdot dl$, where h is the height of the droplet and S is the surface area) interact to deform the lamellae.

The deflection is $\delta \approx \frac{\gamma \cdot H^3}{E \cdot a \cdot dl^2}$ and it decreases with the length of flaps. Thus, not complete heating of lamellae by light is not the only reason for weaker deformation of long lamellae. The longer are the flaps, the weaker they deform.

Two previous experiments showed separately that surface tension forces can cause considerable deformation of lamellae, deformation/recovery depends on the length of lamellae, and recovery can be induced by light. Therefore, we investigated the possibilities to induce deformation/recovery of lamellae by a combination of surface tension forces and light (**Figure 6**). We fabricated lamellae and cut a flap with a length ≈5 mm, which was further actuated by water droplets and light. Water droplet was deposited between two flaps and the flaps were illuminated with light to soften them. The water droplet was either advanced or receded. We observed that water droplets deformed flaps upon their illumination with light. Afterward, the

76

**ADVANCED
SCIENCE NEWS**

www.advancedsciencenews.com

small
structures

www.small-structures.com
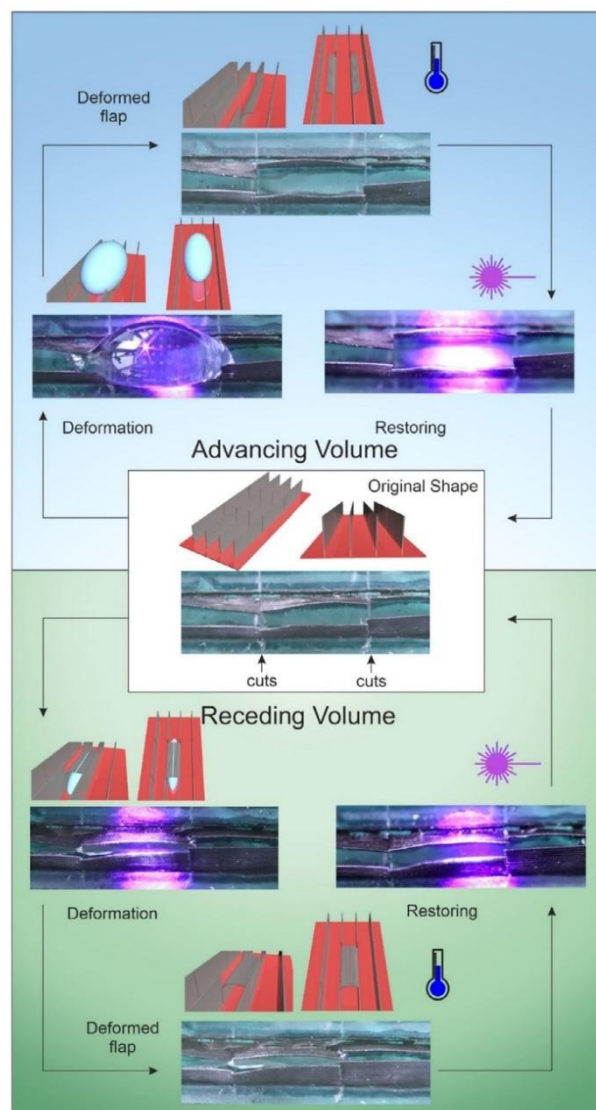
Figure 6. Deformation and recovery of the flaps made by light exposure by advancing volume droplet and receding volume water droplet.

temperature was reduced to 4 °C using the Peltier element, where the sample was placed, to store the temporary shape (deformed flap). The lamellae stayed in a temporary deformed state after the water droplet was removed. Illumination with light resulted in the recovery of deformed lamellae within 30–60 s. The recovery with light exposure was 5 times faster than the one achieved with thermal exposure in our previous investigation.[23] The reason for this difference is most probably faster heating with light—lamellae get heated by light faster because they directly absorb light. In the case of thermal heating, the heat needs to diffuse through the sample. It is important that the illumination of flaps, which contact with water droplets, does not result in their softening and bending. Indeed, the maximum

temperature reached in the water environment can be up to 27–28 °C which is 12 °C lower than the minimum required to bend the structures (Figure S7, Supporting Information). Such a big difference in comparison to behavior in the air can be explained by the heat capacity of the water, which is 4182 J kg^{-1} K, which is much higher than that of air, that is, 1005 J kg^{-1} K (density of air is much lower than that of water).[26]

Finally, we demonstrated the application of photothermally sensitive lamellae for the design of smart valves for microfluidic devices. We fabricated rectangular reservoirs for liquids. The walls of these reservoirs are formed by lamellae. The lamellae were cut with scissors to form flaps, which will act as valves. The main advantage of black-ink-coated flaps is the possibility of their individual control—they can be actuated independently from each other. Unlike our previous article,[23] where only recovery of the whole sample by heating was possible, here, each flap can soften individually which allows the design of smart light-controlled smart valves that can be used to control the mixing of liquids on a microscale.

An example of a such device with light-controlled valves is shown in **Figure 7**. Two valves (shown by red and yellow rectangles) were softened by light exposure to allow advancing water. When both valves remained in a closed state (no bending), the liquid, colored in red, did not flow out of the groove (Figure 7b). Illumination with light softens the lamellae that allow their bending by increasing the volume of the water in the channels (Figure 7c,d). The mixing of both fluids depended on the flow rate. It was possible to limit the mixing rate by an incomplete opening of the valve (e.g., using a half-opened valve) and by reducing the volume of liquids. After mixing, the temperature was rapidly dropped to 4 °C to fix the temporary shape. The recovery of the valves was made in the absence of the liquid because the forces exerted by the water droplet on the deformed flap (gravity, weight, capillarity force) restricted the recovery of the flap. Moreover, the temperature achieved during the photostimulation of the black lamella when it was in the contact with water is lower than the minimum required to get the soft state of the surface that is due to the higher heat conductivity of water discussed above (Figure S7, Supporting Information). The recovery time for each valve was different, possibly explained by the length of the valve. For the valve in a red rectangle, the time was 52 s, while for the vale in a yellow square took 84 s to recover.

3. Conclusion

This article reports the fabrication of light-sensitive structured surfaces with high-aspect ratio lamellae and lamellae flaps. The high-aspect ratio features were fabrication using MEW. The sensitivity to light was provided by using a combination of thermoresponsive SMP and its coating by black ink, which converts light into heat. The approach suggested in this study is a simple method involving dipping the lamellar surface into a black ink solution to stain the surface of the polymeric lamellae. Unlike incorporating black particles within the polymer, this method does not affect the degree of crystallinity of the material.

The lamellae exposed to low temperatures are hard and cannot be deformed by water droplets. The temperature reached upon exposure to light-coated polymer was close to the melting peak

**ADVANCED
SCIENCE NEWS**

www.advancedsciencenews.com

**small
structures**

www.small-structures.com
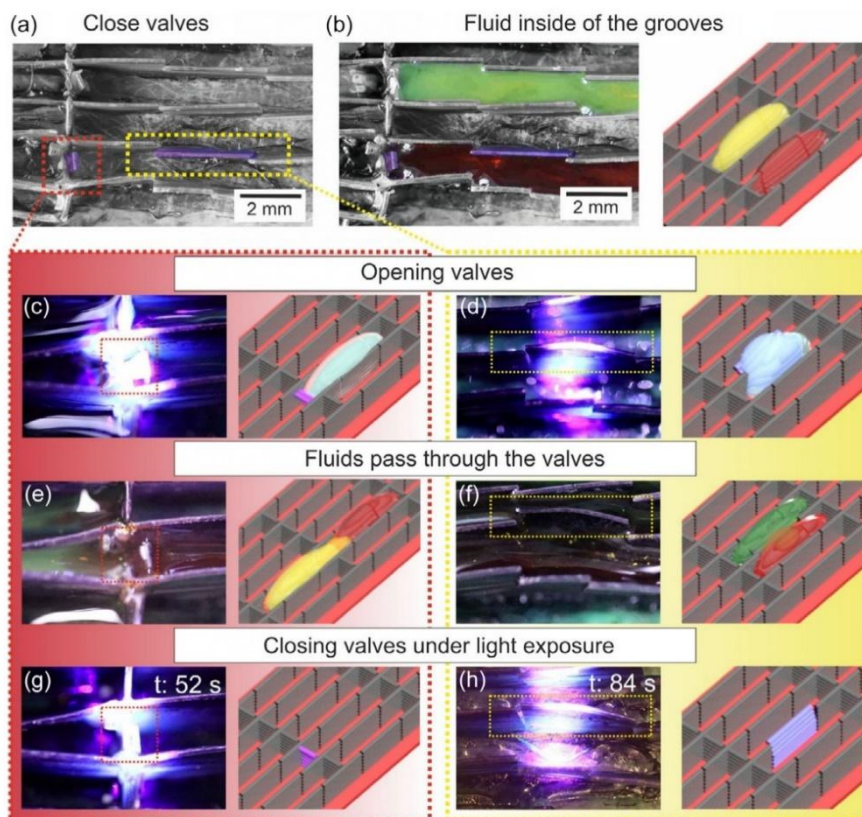
Figure 7. Use of multiple independently light-controlled smart valves for control of mixing of liquids: a) valves are closed and b) the liquid (colored in yellow and red) remained inside of the cavities formed by the flaps; c,d) by advancing volume of the water, the smart valves opened; and e,f) the fluids combined and circulated to other grooves. g,h) The recovery of the position of the flaps was conducted by photothermal effect; smart valves are highlighted in red and yellow squares.

temperature of the soft segment of the polyurethane which led to softening of the polymer. Due to this effect, it was possible to deform and recover the surface by water droplets deposited on lamellae. This soft state can be preserved even after exposition to light which allows deformation due to the soft mechanical memory shown by the surface. The deformed state can be fixed by cooling down resulting in the crystallization of the polymer. The deformation and recovery extent as well as rate depend on the length of lamellae—shorter lamellae flaps are deformed stronger, recovered complete, and do it faster than long ones that are also due to inhomogeneity of heating. Finally, we demonstrated the application of the developed approach and materials for the fabrication of smart light-controlled valves, which can be used for the controlled mixing of fluids in microfluidic devices. This brings a potential application in the creation of multiple smart valves that can act independently, opening and closing the passage for combining fluids and reactions.

4. Experimental Section

Materials: For the fabrication of the lamellar surface, a thermoresponsive polyester urethane (polybutylene adipate based) was required. For its synthesis, poly(1,4-butylene adipate) (PBA) diol Desmophen 2505 was selected from Covestro Deutschland AG (Leverkusen, Germany) and 4,4′-diphenylmethane diisocyanate (MDI) was purchased from Fisher Scientific (Schwerte, Germany). 1,4-butanediol (BD), as well as a molecular sieve with a pore size of 4 Å, was obtained from Alfa Aesar (Kandel, Germany). Polylactide (PLA 4032D) was obtained from NatureWorks Ltd. (Minnetonka, MN, USA) and chloroform from Merck (Darmstadt, Germany). Black ink Edding T100 (Ahrensburg, Germany) was diluted with isopropanol from Merck (Darmstadt, Germany).

Synthesis of TPU: Poly(1,4-butylene)-based poly(ester urethane) (TPU PBA-75) was synthesized as previously described.[23] Briefly, 0.037 mol of dried PBA-diol Desmophen 2505 reacted at 120 °C with 0.157 mol of MDI for 90 min. The isocyanate prepolymer reacted with 0.12 mol dried BD. The reaction stopped by pouring the melt onto a plate covered with a polytetrafluoroethylene film. Finally, TPU PBA-75 was cured in an oven at 80 °C for 120 min and ground into granules for further use.

Spin Coating of the Glass Slides: Glass slides of 26 mm × 76 mm were coated with 500 μL of a solution of PLA in chloroform (10 mg mL^{-1}) with a Spin Coater Ossila (UK). The rotational speed was set at 500 rpm for 10 s to ensure total coverage of the surface, and then it increased to 4000 rpm for 1 min.

Fabrication of the Surfaces: The lamellar surface was fabricated as previously described.[23] Briefly, the MEW of TPU PBA-75 was made in a 3D Discovery printer Regen Hu (Villaz-St-Pierre, Switzerland). The conditions for MEW were set at 215 °C, 3 kV of voltage, pneumatic pressure at 0.1 MPa, the distance between collector and nozzle was 2 mm, and the

translation speed (F) was 100 mm s^{-1}. The extrusion was made with a metallic needle of 200 μm inner diameter. By stacking the fibers one upon each other, the lamellar surface was fabricated. To create the flap surface, the lamellae were cut transversally every 5 mm with a sharp razor blade. The distance between the lamellae was 1500 μm, and the height was 1500 μm.

Dip Coating: The lamellar surface was dip-coated in a solution of a commercial black ink Edding T100 (Germany) in isopropanol at 25% v/v. A dip coater Ossila (UK) was used. The samples were immersed for 10 s at 10 mm s^{-1}, followed by a withdrawal with a speed rate of 1 mm s^{-1}. The samples were dried in a vertical position.

SEM: The SEM photographs were made by using a scanning electron microscope Thermo Fischer Scientific Apreo 2 SEM (Germany). A lamella section was fixed on an SEM stub with the help of copper double-phase adhesive tape. The sample was sputtered with ≈1.3 nm platinum to ensure conductivity using a Leica EM ACE600 (Wetzlar, Germany). The sputtering rate was set at 0.02 nm s^{-1}, with a current of 35 mA, under Argon 0.05 mbar.

Dynamical Mechanical Analysis: The mechanical properties of the material were measured in a Modular Compact Rheometer MCR 702 Multidrive from Anton Paar GmbH (Ostfildern, Germany). Mechanical properties measurement was done for the lamella when it was not black-coated and exposed and not exposed to light. A logarithmic frequency sweep from 100 to 0.1 Hz was done with constant extensional stress (σ) of 0.25 MPa. The white and black lamella were exposed to light for 3 s every 30 s to avoid the degradation of the material.

The extensional cyclic experiment was done in a linear ramp mode increasing the strain (ϵ) from 0.01% to 25% with an extension rate of 1% min^{-1}.

To measure the elastic deformation and recovery of the black-coated lamellae, the rheological measurements were done in five steps: the first one was made at a constant stress of 5 MPa, and the strain was measured, which shows the deformation of the lamella for 300 s. In the second stage, the sample was exposed to light laser while keeping the stress at 5 MPa for 300 s. In this stage, the sample was exposed to light for 3 s every 30 s. The third stage was done by the fixation of the stretched lamella while pouring liquid nitrogen, and the stress was set at 5 MPa for 600 s. The fourth and fifth stages were the recovery of the sample by releasing the stress without and with light exposure, respectively.

For the light exposure, we used a violet laser diode module. The laser had a wavelength (λ) of 405 nm, class IIIb, with an elliptical beam with an adjustable focus. The distance between the sample and laser light was set at 10 cm for all the experiments.

Deformation Studies: The lamellae surface was cut into flaps of 5 mm in length. The deformation studies were made for the long lamella and the flaps. The deformation of the structure was made under the photothermal effect produced by light exposure while the water volume increased or decreased depending if it was advancing or receding volume. The shape-memory behavior of the structured topographical surface was studied by deforming the lamellae under light exposure. By advancing and receding the volume of a water drop, the lamellae were able to deform in the direction of the water flow. The sample was fixed by cooling it to 4 °C. The recovery of the original state of the sample was accomplished by the photothermal effect provided by light exposure.

Statistical Analysis: The statistical analysis was made in Origin Lab software. Data were produced with two replicates. The analysis of variance (ANOVA) was performed at a significance of 95% ($p = 0.05$). Tukey test was used as comparison test at a $p = 0.05$.

Supporting Information

Supporting Information is available from the Wiley Online Library or from the author.

Acknowledgements

Conflict of Interest

The authors declare no conflict of interest.

Data Availability Statement

The data that support the findings of this study are available from the corresponding author upon reasonable request.

Keywords

[1] a) A. Kirillova, L. Ionov, *J. Mater. Chem. B* **2019**, *7*, 1597; b) E. Gultepe, J. S. Randhawa, S. Kadam, S. Yamanaka, F. M. Selaru, E. J. Shin, A. N. Kalloo, D. H. Gracias, *Adv. Mater.* **2013**, *25*, 514.

[2] a) A. Kirillova, R. Maxson, G. Stoychev, C. T. Gomillion, L. Ionov, *Adv. Mater.* **2017**, *29*, 1703443; b) H. Wei, Q. Zhang, Y. Yao, L. Liu, Y. Liu, J. Leng, *ACS Appl. Mater. Interfaces* **2017**, *9*, 876.

[3] a) S. Sundaram, D. S. Kim, M. A. Baldo, R. C. Hayward, W. Matusik, *ACS Appl. Mater. Interfaces* **2017**, *9*, 32290; b) B. Q. Y. Chan, Y. T. Chong, S. Wang, C. J. J. Lee, C. Owh, F. Wang, F. Wang, *Chem. Eng. J.* **2022**, *430*, 132513.

[4] Q. Ge, A. H. Sakhaei, H. Lee, C. K. Dunn, N. X. Fang, M. L. Dunn, *Sci. Rep.* **2016**, *6*, 31110.

[5] D. Kokkinis, M. Schaffner, A. R. Studart, *Nat. Commun.* **2015**, *6*, 8643.

[6] a) A. Samanta, W. Huang, H. Chaudhry, Q. Wang, S. K. Shaw, H. Ding, *ACS Appl. Mater. Interfaces* **2020**, *12*, 18032; b) L. Zhong, H. Zhu, Y. Wu, Z. Guo, *J. Colloid Interface Sci.* **2018**, *525*, 234;

[7] a) L. Pocivavsek, S. -H. Ye, J. Pugar, E. Tzeng, E. Cerda, S. Velankar, W. R. Wagner, *Biomaterials* **2019**, *192*, 226; b) J. -N. Wang, Y. -Q. Liu, Y. -L. Zhang, J. Feng, H. -B. Sun, *NPG Asia Mater.* **2018**, *10*, e470.

[8] a) K. Okada, Y. Miura, T. Chiya, Y. Tokudome, M. Takahashi, *RSC Adv.* **2020**, *10*, 28032; b) M. Ebara, K. Uto, N. Idota, J. M. Hoffman, T. Aoyagi, *Adv. Mater.* **2012**, *24*, 273;

[9] a) S. Bahl, H. Nagar, I. Singh, S. Sehgal, *Mater. Today Proc.* **2020**, *28*, 1302; b) Y. Song, Y. Hu, Y. Zhang, G. Li, D. Wang, Y. Yang, Y. Zhang, Y. Zhang, W. Zhu, J. Li, D. Wu, J. Chu, *ACS Appl. Mater. Interfaces* **2022**, *14*, 37248.

[10] I. Apsite, S. Salehi, L. Ionov, *Chem. Rev.* **2022**, *122*, 1349.

[11] a) S. A. Turner, J. Zhou, S. S. Sheiko, V. S. Ashby, *ACS Appl. Mater. Interfaces* **2014**, *6*, 8017; b) X. Luo, H. Lai, Z. Cheng, P. Liu, Y. Li, X. Yu, Y. Liu, *Chem. Eng. J.* **2021**, *403*, 126356.

[12] a) N. García-Huete, J. M. Cuevas, J. M. Laza, J. L. Vilas, L. M. León, *Polymers* **2015**, *7*, 1674; b) J. Song, M. Gao, C. Zhao, Y. Lu, L. Huang, X. Liu, C. J. Carmalt, X. Deng, I. P. Parkin, *ACS Nano* **2017**, *11*, 9259.

79

**ADVANCED
SCIENCE NEWS**

www.advancedsciencenews.com

**small
structures**

www.small-structures.com

[13] a) J. K. Park, S. Kim, *Lab Chip* **2017**, *17*, 1793; b) Y. Shao, J. Zhao, Y. Fan, Z. Wan, L. Lu, Z. Zhang, W. Ming, L. Ren, *Chem. Eng. J.* **2020**, *382*, 122989.

[14] a) H. Yang, W. R. Leow, T. Wang, J. Wang, J. Yu, K. He, D. Qi, C. Wan, X. Chen, *Adv. Mater.* **2017**, *29*, 1701627; b) W. Wang, D. Shen, X. Li, Y. Yao, J. Lin, A. Wang, J. Yu, Z. L. Wang, S. W. Hong, Z. Lin, S. Lin, *Angew. Chem. Int. Ed.* **2018**, *57*, 2139.

[15] J. T. Schiphorst, Technische Universiteit Eindhoven, Eindhoven, Netherlands **2018**.

[16] D. Habault, H. Zhang, Y. Zhao, *Chem. Soc. Rev.* **2013**, *42*, 7244.

[17] G. Stoychev, A. Kirillova, L. Ionov, *Adv. Opt. Mater.* **2019**, *7*, 1900067.

[18] M. Herath, J. Epaarachchi, M. Islam, C. Yan, F. Zhang, J. Leng, *J. Intell. Mater. Syst. Struct.* **2019**, *30*, 3124.

[19] S. Xu, X. Bai, L. Wang, *Inorg. Chem. Front.* **2018**, *5*, 751.

[20] A. Raza, U. Hayat, T. Rasheed, M. Bilal, H. M. N. Iqbal, *J. Mater. Res. Technol.* **2019**, *8*, 1497.

[21] X. Lin, W. Xie, Q. Lin, Y. Cai, Y. Hua, J. Lin, G. He, J. Chen, *Polym. Chem.* **2021**, *12*, 3375.

[22] Z.-Z. Jiao, H. Zhou, X.-C. Han, D.-D. Han, Y.-L. Zhang, *J. Colloid Interface Sci.* **2023**, *629*, 582.

[23] G. Constante, I. Apsite, P. Auerbach, S. Aland, D. Schönfeld, T. Pretsch, P. Milkin, L. Ionov, *ACS Appl. Mater. Interfaces* **2022**, *14*, 20208.

[24] P. Milkin, M. Danzer, L. Ionov, *Macromol. Rapid Commun.* **2022**, *43*, 2200307.

[25] C. Py, P. Reverdy, L. Doppler, J. Bico, B. Roman, C. N. Baroud, *Phys. Rev. Lett.* **2007**, *98*, 156103.

[26] H. Brooks, C. Wright, S. Harris, A. Fsadni, *Addit. Manuf.* **2018**, *22*, 138.

80

Supporting Information

Reversibly photoswitchable high-aspect ratio surfaces

Gissela Constante, Indra Apsite, Dennis Schönfeld, Thorsten Pretsch, and Leonid Ionov*
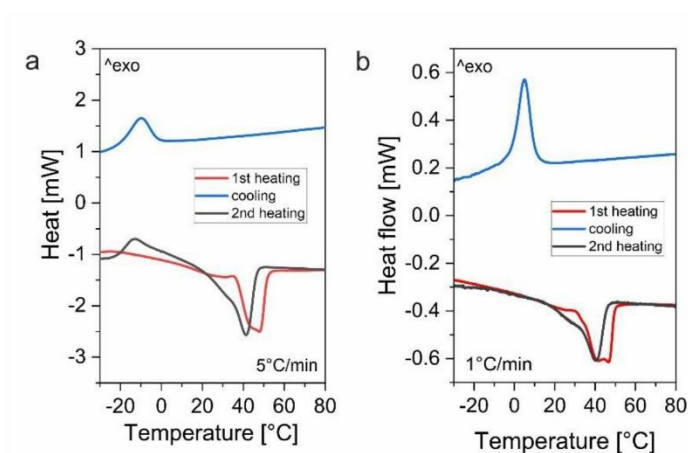
Figure S1. Dynamic Scanning Calorimetry (DSC) of the PEU (TPU PBA-75) (a) at a heating rate of 5 °C·min⁻¹ and (b) at 1 °C·min⁻¹
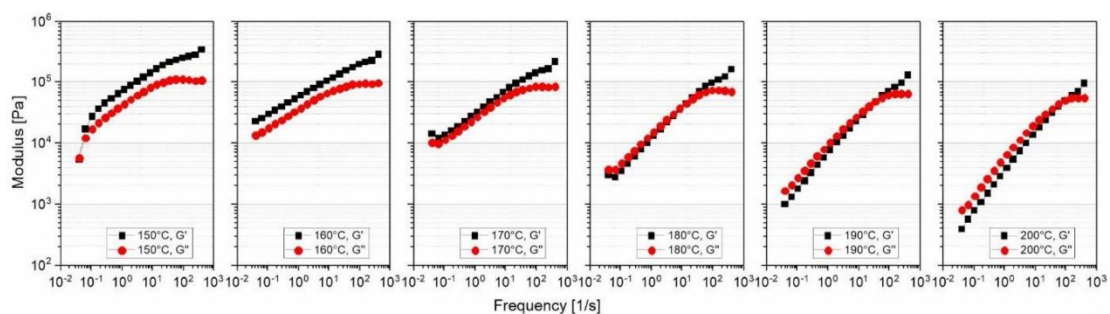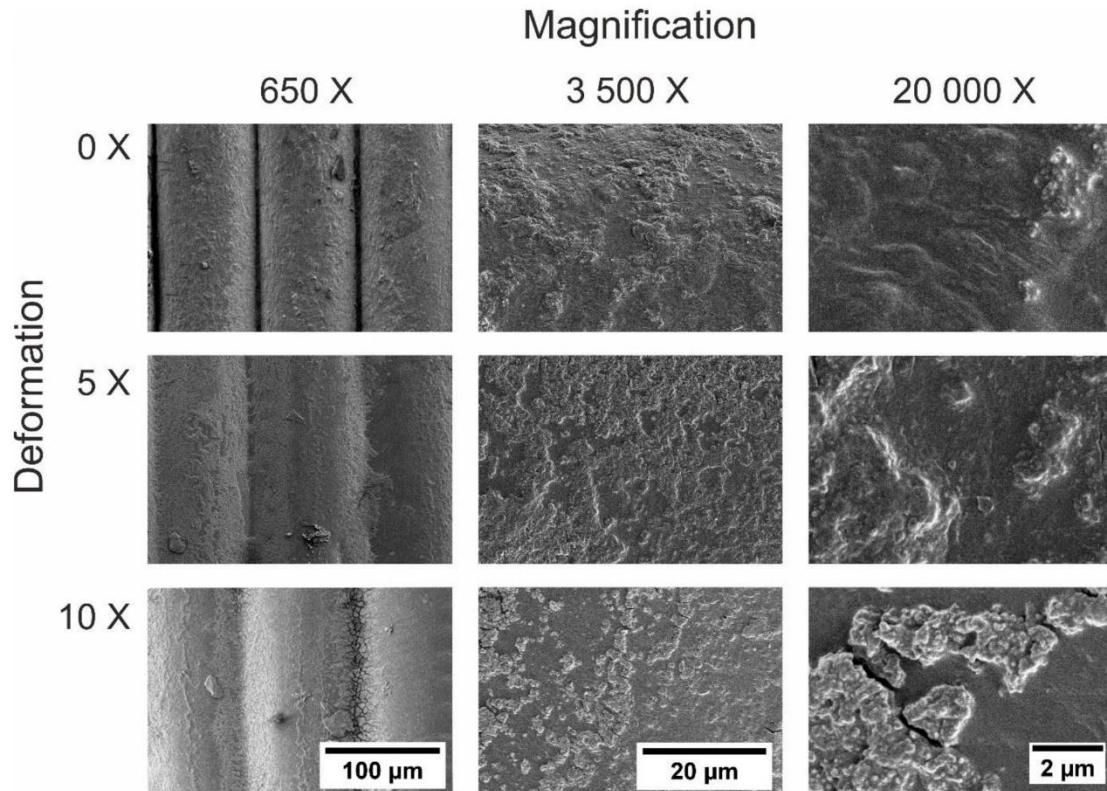

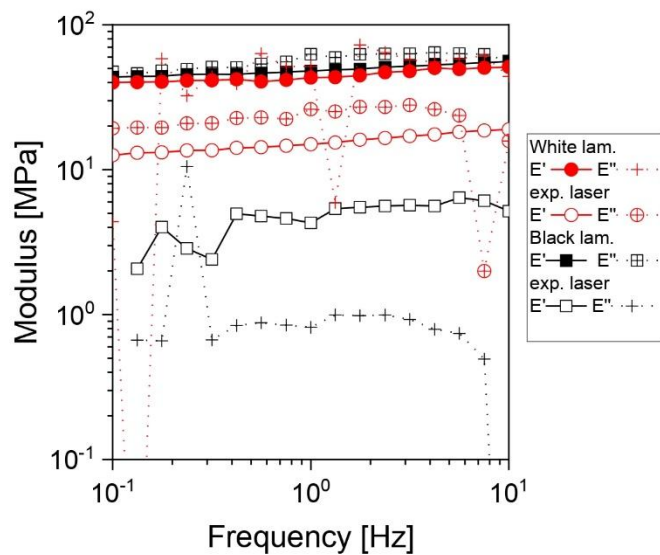**Figure S2.** Storage and loss modulus of the PEU (TPU PBA-75) at a constant shear strain (γ) of 5 %

1
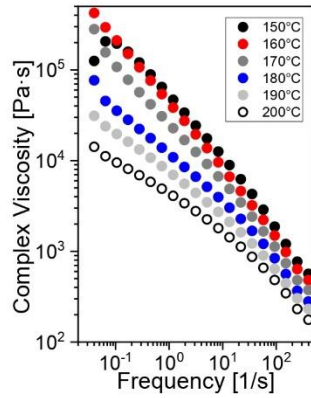
Figure S3. Complex viscosity measured by frequency sweep of the PEU (TPU PBA-75) at a constant shear strain (γ) of 5 %
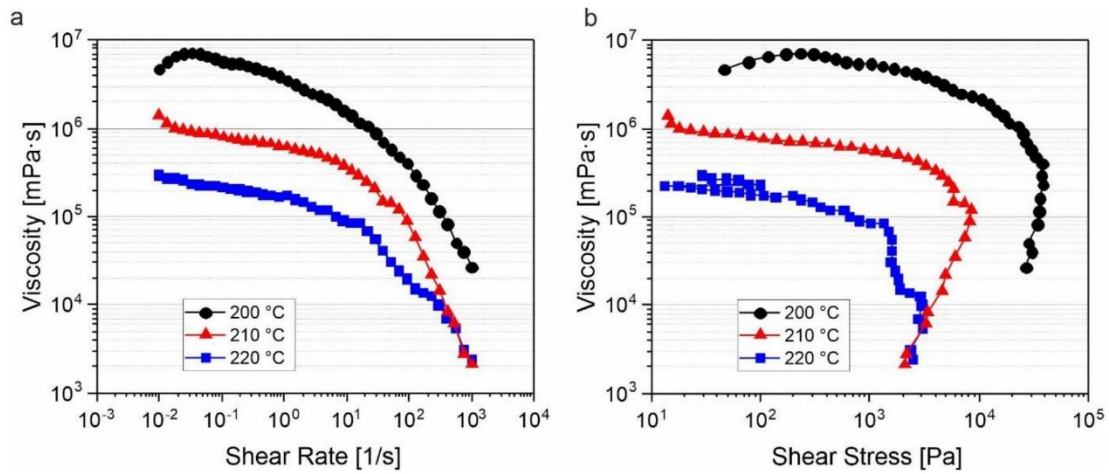
Figure S4. Viscosity curve of the PEU (TPU PBA-75)

2

Figure S5. SEM images describing the coating state on the lamella after 5 and 10 cycles of deformation at different magnifications.

Figure S6. Storage and Loss moduli measured in the extensional frequency sweep of the coated and non-coated TPU PBA lamella, exposed and not exposed to light.

3

Table S1. Storage Modulus obtained from the extensional frequency sweep of the lamellae before and after black ink coating and light exposure.

Sample	Storage Modulus
White lamella	44.6 ± 4 MPa
White lamella light exp.	15.5 ± 2 MPa
Black lamella	49.0 ± 4 MPa
Black lamella light exp.	5.0 ± 1 MPa
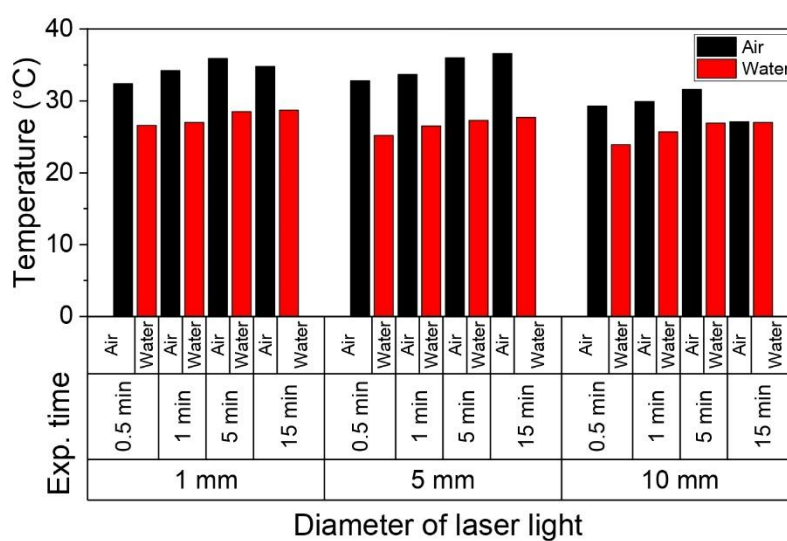
Figure S7. Maximum temperature achieved on the black lamellar surface when the surrounding environment is air and water.

4
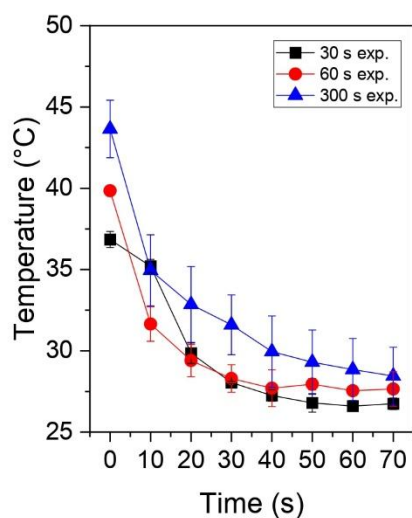
Figure S8. Decay of temperature after different times of light exposure
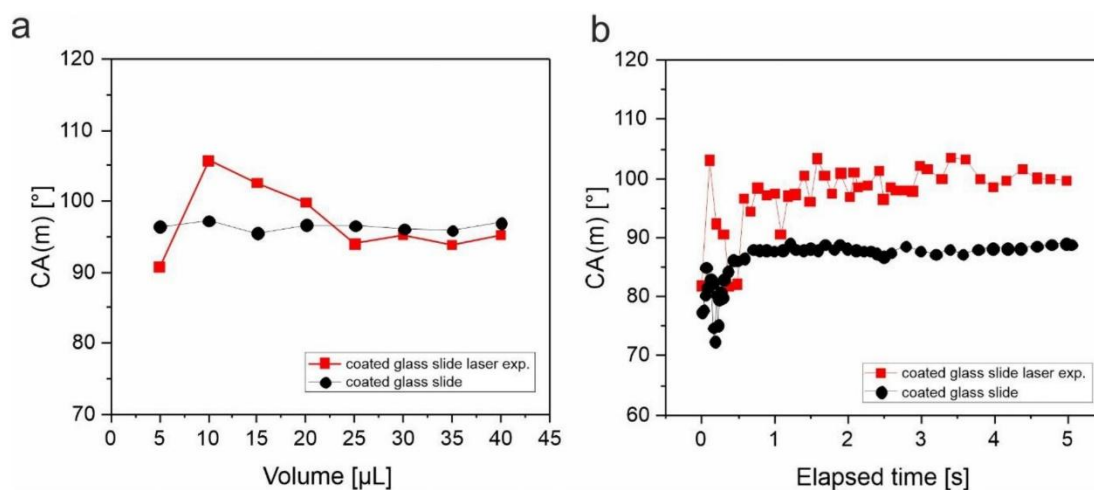
Figure S9. Measured a) advancing contact angle on the black coated glass slide, and b) the sessile drop measurements on the black coated glass slide before and after light exposure

Videos:

1.- Deformation and valve opening

2.- Passage of fluid through valve 2

3.- Recovery of valve 2

5

9.3.Publication 3

Switchable Elastocapillarity of High-Aspect-Ratio Topographically Structured Surfaces

Gissela Constante, Dennis Schönfeld, Thorsten Pretsch, Pavel Milkin, Ilia Sadilov, and Leonid Ionov

Switchable Elastocapillarity of High-Aspect-Ratio Topographically Structured Surfaces

Gissela Constante, Dennis Schönfeld, Thorsten Pretsch, Pavel Milkin, Ilia Sadilov, and Leonid Ionov*

Cite This: https://doi.org/10.1021/acs.langmuir.5c02002

Read Online

ACCESS | Metrics & More | Article Recommendations | Supporting Information

ABSTRACT: Elastocapillarity, the interplay between elasticity and capillarity, is of great importance for various fields, including surface control, microfluidics, biotechnology, robotics, medicine, microtechnology, and more. This study investigates the elastocapillarity of surfaces with partially cantilever-like vertical lamellae with switchable mechanical properties, where one side is fixed to a substrate, and the other side can move freely. In this work, we want to understand the interaction between lamellae and water droplets during their sliding. Specifically, we want to understand how the flexibility of the lamellae affects the sliding of water droplets and how the deformation of the lamellae during sliding depends on their flexibility and interaction with the water droplet. We control flexibility by the mechanical properties of the lamellae, which depend on the mechanical properties of the polymer forming them, and how lamellae are attached/adhered to the substrate. Depending on fabrication, lamellae can have three kinds of contacts with the substrate: strong adhesion (fusion of the bottom of the lamellae to the substrate), intermediate adhesion (high-friction lamellae–substrate contact), and weak adhesion (low-friction lamellae–substrate contact—lamellae with an air gap underneath). Moreover, it was found that lamellae neglect the effect of the material of the substrate on water droplet sliding, and freely moving lamellae promote the fastest sliding of droplets due to capillary forces. The water droplets are also able to cause the deformation of lamellae during sliding. We found that rigid lamellae rigidly and strongly/intermediately attached to a substrate are not deformed by droplets; the upper parts of soft lamellae strongly and intermediately attached to a substrate were deformed by the water droplet, while their lower parts remained immobile, and the sliding droplet can deform both rigid and soft lamellae weakly connected to a substrate.

Deformation by elastocapillarity

PU-PBA / PLA / PDMS — higher friction force

PU-PBA / PLA / AIR — lower friction force
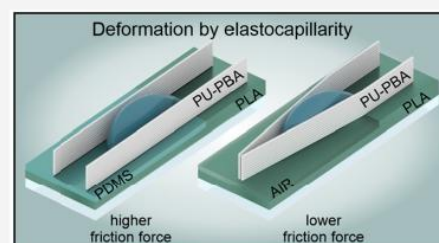
■ INTRODUCTION

The understanding of elastocapillarity is essential for diverse applications, including controlling surface wettability,[1−3] designing microfluidic systems,[4] and understanding biological processes such as cell adhesion,[5] transportation of substances,[4] soft robotics,[6] medical devices,[5] and microtechnology.[7] One remarkable example is the fabrication of self-folded conduits by wrapping a membrane around a droplet due to elastocapillarity presented by Samy et al. They established a correlation between droplet size and capillary length scale[8] and showed that the wrapping of a thin PDMS sheet can be done by a liquid drop. In another example, it was shown that elastocapillarity affects the rolling and movement of solid particles. In particular, it was predicted that the movement of nanoparticles on soft elastic substrates is a result of the interplay of capillary, elastic, and friction forces.[9]

For capillaries and parallel rods, the equilibrium rising height of the water (h_J) can be estimated by Jurin's law

$$h_J = \frac{2\gamma}{\rho g d} \tag{1}$$

where γ is the surface tension, ρ is the density of water, g is the gravity, and d is the distance between the rods. This estimation is, however, made for rigid materials, which do not get

considerably deformed (d is a constant). The soft walls can be strongly deformed and even collapsed by capillary forces. As a result, the gap between the walls is reduced (d decreases), and the equilibrium capillary rise correspondingly increases.[10,11] The deformation by capillary forces strongly depends on the mechanical properties of the material that constitutes the surface.[12,13]

$$l_e = \frac{(1 - \nu^2)\gamma}{\pi E} \tag{2}$$

Here, l_e is the length of elastic deformation, ν is Poisson's ratio, γ is the surface tension of water, and E is the Young's modulus of the polymer. This equation shows that the bending scales with the inverse of the elastic modulus of the material, and soft materials deform more easily. The heating above melting or glass transition temperature results in softening of materials that must affect their interactions with liquids and influence

ACS Publications

A

deformation.[14] In particular, for soft materials such as elastomers,[15] hydrogels,[16] or synthetic polymer meshes,[17] the interaction of surface tension and elasticity made by the elastocapillarity becomes significant. This phenomenon is observed in various natural and artificial systems, from gels and biological tissues to micro- and nanoscale devices.[18−20]

Sliding of a droplet on topographically structured surfaces was also a topic of numerous investigations, and it was shown that the droplet shape, velocity, contact angle hysteresis, and critical inclination angle determine the sliding behavior.[21,22] Karpitschka and collaborators focused their research on understanding the behavior of droplets on inclined solid surfaces. In their investigation, the water droplet slid onto a soft substrate and formed a wetting ridge. While sliding, it was visible that the drop moved along the substrate like surfing the ridge. The surfing of the droplet happens when the contact line of the drop slides down the wetting ridge, forming one after the other.[22] These results provide information in biological studies for cell patterning and self-organization of cell tissues or in the physics field for the development of capillarity-based microrheometers.[22,23]

Similar to the capillary rise, the sliding of droplets along inclined trenches is also expected to be dependent on the mechanical properties of materials forming the trenches. Indeed, sliding along the grooves is common with capillary rise, as the sliding depends on the distance between the walls of the groove, which could be fixed if the material is stiff or variable if the material is soft. Wetting behavior (not water sliding) of such surfaces formed by high-aspect-ratio lamellar surfaces with switchable mechanical properties by water has been studied in our previous publications.[12,24] We have shown that bending of lamellae with a high aspect ratio can be realized by applying forces exerted by water droplets. The deflection of the lamellae was strongly dependent on their mechanical properties, which depend on temperature. At room temperature, the material of lamellae was stiff and could not be deformed by droplets, while at higher temperatures, the elastic modulus of the material decreased significantly so that the lamellae could be deformed. In these studies, the first layer of the lamellae was fixed on the substrate along its full length by melting during deposition, i.e., the lower part of the lamellae was undeformable. The understanding of how water deforms such structures that are partially free-standing, and only one end is grounded (cantilever-like), has also been the topic of several investigations. For example, the formation of vertical hair bundles[3] and complex hierarchical patterns[10] is produced by the effect of capillarity, hydrodynamics, elasticity of the material, and bundle length.[25] However, the elastocapillarity of not completely cantilever-like lamellae (resembling horizontal flat hairs) with switchable mechanical properties, which are attached to a substrate by one side and the other is able to slide parallel to the substrate, has not been properly investigated, as the contribution of friction forces is not considered.

The aim of this work is to understand the interaction between lamellae and water droplets during their sliding. Specifically, we want to understand how the flexibility of the lamellae affects the sliding of water droplets and how the deformation of the lamellae during sliding depends on their flexibility and interaction with the water droplet. Flexibility is controlled by the mechanical properties of the lamellae (depending on the mechanical properties of the polymer forming lamellae) and how lamellae are attached/adhered to the substrate. So, in this paper, we introduce a new variable,

the strength of the interactions between lamellae and the substrate, and investigate its contribution.

We propose the analysis of this deformation mechanism from a different perspective, by sliding a droplet on a structured surface such as when surfaces are cleaned. Parallel walls, attached to one end, can deform in 3 different directions: x, y, and z. Along the x- and y-axes, sliding occurs on the surface, while along the z-axis, bending occurs in the top layers. During the sliding of the droplet on the lamellar surface, the water brings both lamellae together, resulting in a reduction of the gap between the two lamellae. Through the exploration of the elastocapillarity of a high-aspect-ratio lamellar surface, we hope to gain deeper insights into the remarkable interplay between the substrate and elasticity, ultimately unlocking new avenues for innovative technological advancements, such as control of surface deformations, control of droplets' movement, and pinning behavior. The combination of substrates with different adhesions and wettabilities, along with the deformation of lamellae produced by a water droplet, can be applied to regulate fluid flow. We previously utilized this concept in the development of smart valves on lamellar surfaces.

■ MATERIALS AND METHODS

Materials. The fabrication of the free-standing lamella required the shape-memory polymer poly(1,4-butylene adipate)-based polyurethane (PU−PBA). The synthesis of PU−PBA was made by the reaction of poly(1,4-butylene adipate) (PBA) diol Desmophen 2505 from Covestro Deutschland AG (Leverkusen, Germany), 4,4′-diphenylmethane diisocyanate (MDI), which was purchased from Fisher Scientific (Schwerte, Germany), and 1,4-butanediol (BD) obtained from Alfa Aesar (Kandel, Germany). The substrate was made with a solution of polylactide (PLA 4032D) from NatureWorks Ltd. (Minnetonka, MN) and chloroform from Merck (Darmstadt, Germany). The coating of PDMS was made with the base and curing agent Sylgard 184 Silicon elastomer from The Dow Chemical Company (Midland, MI) and dissolved in hexane from Merck (Darmstadt, Germany). The sacrificial layer was made of poly(vinyl alcohol) (PVA) 89−98 kDa from Merck (Darmstadt, Germany).

Synthesis of TPU. Poly(1,4-butylene adipate)-based polyurethane (PU−PBA) was synthesized as previously described[12,24,26,27] using the prepolymer method. Briefly, 0.037 mol of dried PBA-diol Desmophen 2505 was reacted with 0.157 mol of MDI at 120 °C for 90 min. Then, 0.120 mol of dried BD was added to react with the isocyanate prepolymer. As soon as the viscosity increased significantly, the reaction was stopped by pouring the melt onto a plate covered with a poly(tetrafluoroethylene) film. Finally, PU−PBA was cured in an oven at 80 °C for 120 min and ground into granules for further use.

Spin Coating of the Glass Slides. Glass slides of 26×76 mm² were coated with 500 μL of a solution of PLA in chloroform (10 mg mL⁻¹) with a Spin Coater Ossila (U.K.). The rotational speed was set at 500 rpm for 10 s to ensure total coverage of the surface, and then it increased to 4000 rpm for 1 min.

Dip Coating. The PLA-coated glass slides were dip-coated in two different solutions: PVA in water and PDMS in hexane. For the first one, a solution of 20% w/v PVA in Milli-Q water was prepared. The solution was heated to 60−70 °C until it became transparent. To distinguish the disappearance of the layer after the removal of the sacrificial layer, a drop of diluted rhodamine was added. The PDMS coating was made by the addition of a thin coat of the Sylgard 184 silicone elastomer by reacting a prepolymer base (part A) and a cross-linking curing agent (part B) in a ratio of 10:1. They were mixed at room temperature. Then, 20% w/w of reacted PDMS in hexane was made for the dip coating. A glass slide was coated with the sacrificial layer of PVA at an immersion speed of 6 mm s⁻¹, 10 s of dwelling

time, and a withdrawal of 1 mm s^{-1}. The PVA and PDMS coating covered the 46 mm length of the glass slide.

Fabrication of the Surfaces. The free-standing lamellae were fabricated by melt electrowriting (MEW) on a custom-made device. A filament of PU−PBA with a 1.75 mm diameter was introduced to the filament fused printer/MEW, and the metallic needle with a diameter of 200 μm was used for the printing. A metallic collector was connected to a voltmeter LNC 30000-2neg from Heinziger Electronic GmbH (Rosenheim, Germany). The conditions for melt electrowriting were as follows: 230 °C, 4.5 kV voltage, the distance between the collector and the nozzle was 5 mm, and the translation speed was 1200 mm min^{-1}. The extrusion rate was set at 0.06 mm. The distance between the lamellae was 3 mm, and the height was 2 mm. The G-Code was generated with FullControl GCode Designer Open-Source Software.[28]

The sample that was coated with a layer of PVA was washed by pouring slowly Milli-Q water until the lamellae were detached from the surface (free-standing lamella), while the section that was in contact with the PLA coating remained intact.

Scanning Electron Microscopy (SEM). A scanning electron microscope (Thermo Fischer Scientific Apreo 2 SEM, Germany) was used for imaging the samples. The samples were fixed on an aluminum stub with the help of double-sided copper tape and then sputtered with ~1.3 nm platinum to ensure conductivity using a Leica EM ACE600 (Wetzlar, Germany). The sputtering rate was set at 0.02 nm/s, with a current of 35 mA, under 0.05 mbar argon.

Rheological Measurements. In a rheometer, MCR 702 MultiDrive from Anton Paar (Graz, Austria) a plate−plate geometry with a diameter of 25 mm was used to estimate the friction force between the polymer PU−PBA and PLA, and PU−PBA and PDMS. The disks of 25 mm of PU−PBA and PLA material were prepared by casting the molten polymer in a metallic mold and pressing until a uniform disk was formed. The PDMS disk was prepared by pouring the mixed parts A and B of the prepolymer and cross-linker into the mold and exposing it to 80 °C for 2 h of curing time. The PU−PBA disk was fixed to the geometry by using double-sided tape. The second disk, made of PLA and PDMS, was also attached to the base of the rheometer using double-sided tape because the forces involved in sliding both disks against each other were smaller than the force required to detach the tape from the disks. A perpendicular force was applied to the disks while subjecting them to a low shear rate of 0.1 s^{-1} to measure the torque. The following equation was used to estimate the friction coefficient

$$M = \frac{2}{3}\mu F r \tag{3}$$

where M is the torque (mN·m), μ is the friction coefficient, F is the normal force (N), and r is the radius of the disks (mm).

Sliding Droplet Measurements. In a drop shape analyzer Kruss DSA25 (Krüss GmbH, Hamburg, Germany), a droplet of 20 μL was placed on the substrates PLA−PDMS and PLA−AIR with and without lamellae. The sample holder was tilted to 90°. The video and images were recorded on Advance Kruss software. The sliding measurements were captured at a rate of 10 frames per second, and contact angles were measured from each frame. The position, length, and height of the droplet were measured manually using ImageJ software.

Elastocapillarity Deformation. A droplet of 40 μL was placed between two lamellae with the help of the drop shape analyzer Kruss DSA25 (Krüss GmbH, Hamburg, Germany). The sample holder was tilted up to 90° at a maximum of 120°/min. The samples on the two different substrates PLA−PDMS and PLA−AIR were studied when the polymer PU−PBA was soft (70 °C) and rigid (4 °C).

■ RESULTS AND DISCUSSION

Fabrication of Free-Standing Lamellae. The free-standing lamellae were fabricated on a substrate in a way that one part of the lamellae is fixed on a substrate and another part is able to freely move like a cantilever (Figure 1). Initially,
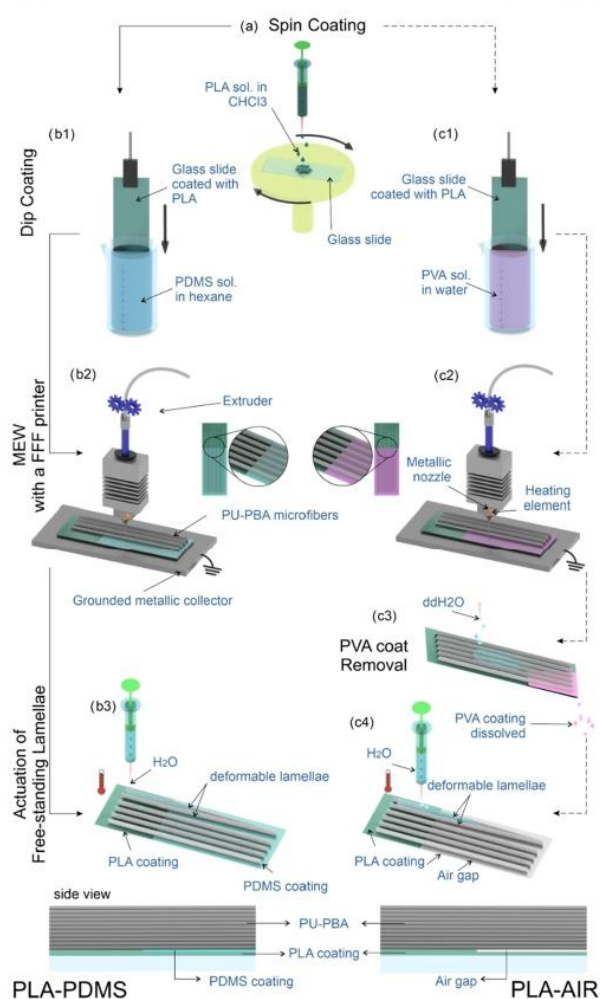

Figure 1. Fabrication methodology for free-standing lamellae. (a) Spin coating of polylactide (PLA) solution on a glass slide, and (b1) dip coating of the PLA-coated glass slide into polydimethylsiloxane (PDMS) solution and (c1) into poly(vinyl alcohol) (PVA) solution. (b2, c2) Melt electrowriting of stacked fibers of polyurethane polybutylene adipate-based (PU−PBA) on different substrates (PDMS and PVA), respectively. (c3) The PVA coating is removed with water. (b3, c4) The actuation of the free-standing lamellae made by elastocapillarity on PDMS and PLA, respectively.

the whole glass slide was coated with a thin layer (0.6 ± 0.1 μm) of polylactide (PLA) using spin coating (Figures 1a and 2e). The PLA layer served to promote adhesion for the initial layer of PU−PBA microfibers, effectively anchoring one end of the structure. The adhesion is explained by the partial melting of the microfibers during deposition (Figure 1b$_2$,c$_2$), allowing the fibers to fuse with the PLA layer, as shown in the scanning electron microscopy (SEM) image (Figure 2c). Thus, the contact between the lamellae and substrate is provided by noncovalent bonds and mechanical interlocking. Additionally, the comparable surface tension values of PLA (34 mN/m for PLA at 25 °C)[29] and PU−PBA (ranging from approximately 33 to 46 mN/m)[30,31] further prevent the separation of these layers after melting.

In order to tailor the ability of the free part to move, half of the substrate was modified by applying two different coatings:
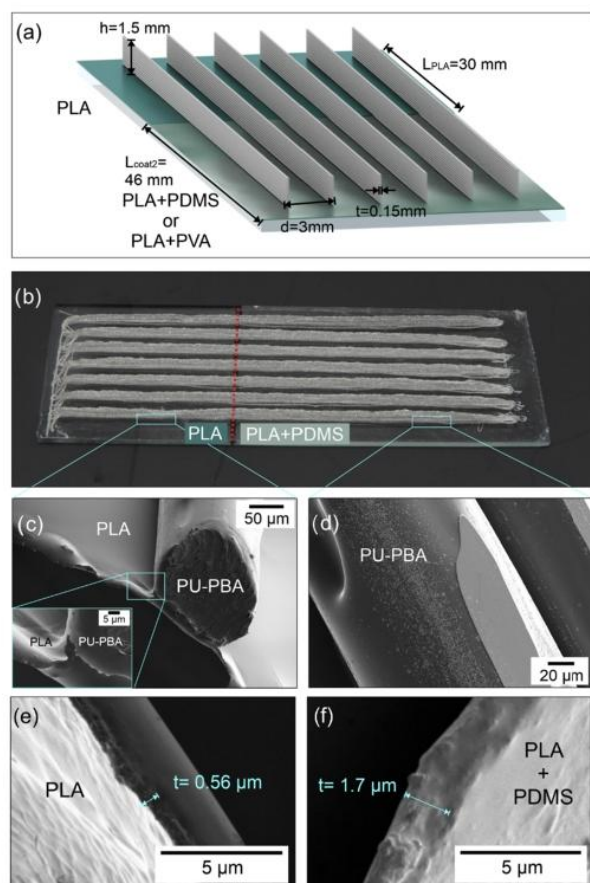
Figure 2. Structured lamellar surface (a) schema diagram of the surface, (b) MEW sample on the combined surface with PLA and PDMS, (c) SEM image of the MEW fiber on the PLA surface showing its adherence by melting, (d) SEM image of the MEW fiber after being in contact on the PDMS surface, and (e, f) the thicknesses of the PLA coating and PLA + PDMS coating obtained by SEM imaging.

poly(dimethylsiloxane) (PDMS) (Figure 1b$_1$) and poly(vinyl alcohol) (PVA) (Figure 1c$_1$). In the first case, a hydrophobic soft PDMS coating, characterized by its low surface energy (19−21 mN/m),[32,33] was applied to a part of the glass slide through a dip-coating process. The thickness of the PDMS layer was determined by the difference between the thickness of the PLA−PDMS coating and the sole PLA layer (Figure 2e,f), yielding a measured thickness of ca. 1 μm for the PDMS coating. In the second case, a sacrificial layer was applied on top of PLA and then removed after deposition of lamellae. PVA was used because it is a water-soluble polymer. After the fiber's deposition, the PVA coating was selectively removed through multiple water rinses, as shown in Figure 1c$_3$. Thus, the free part of the lamellae was able to contact PDMS (Figure

1b$_3$) or to have a gap between lamellae and the substrate (Figure 1c$_4$). It was visually observed that the lamellae did not adhere or fuse to the substrates PDMS (PLA−PDMS substrate) and PLA, after the removal of the sacrificial layer of PVA (PLA−AIR). In both cases, one section of the lamella was attached to the PLA-coated surface, while the other section remained nonadherent. The PLA coated 30 mm of the glass slide, and the second coating covered 46 mm of the glass slide. The second coating was applied through dip coating, as illustrated in Figure 2a. The role of part of the lamellae strongly attached to the PLA substrate is 2-fold: it ensures the position of the free part of the lamellae, which otherwise simply falls, and acts as a reference.

The fibers were fabricated through melt electrowriting (Figure 1b$_2$,c$_2$), exhibiting an average diameter of 150 ± 20 μm (Figure 2d). The larger diameter of these fibers compared to polycaprolactone fibers (about 10 μm[34]) is attributed to the rapid increase in the viscosity of polyurethane with decreasing temperature due to the formation of hydrogen bonds. The design was created using FullControl GCode,[28] ensuring continuous printing without disturbances. By stacking 10 layers, the resulting lamellae reached a height of approximately 1500 μm. The separation distance between individual lamellae was set to 3 mm. The conditions during fabrication were set at a constant voltage of 4.5 kV, at a 230 °C temperature of extrusion, an extrusion value of 0.6 mm for FullControl GCode, and a feed rate of 1200 mm/min.

Notably, the fibers that came in contact with the PDMS coating exhibited a flat surface at their base, which can be attributed to their deposition in the molten state. This effect was a result of the temperature gradient between the extrusion needle and the collector. Conversely, the fibers deposited on the PLA surface adhered to the material, and as evidenced in the SEM image, these fibers seamlessly integrated with the PLA coating, resulting in a cohesive fusion (Figure 2c).

We characterized the wetting properties of pure polymers (Table 1). PDMS is the most hydrophobic one with the largest value of advancing contact angle and a contact angle hysteresis of around 10°. Advancing contact angles on PLA and PU−PBA are very close, but PU−PBA demonstrates a very lower value of contact angle hysteresis.

Estimation of the Friction Coefficient between Materials. The ability of part of the lamellae to move above the substrate (slide along the substrate surface) is a critical factor in achieving their deformation and recovery when the lamellae are brought together by surface tension. It is expected that a low value of the friction coefficient between lamellae and the substrate would reduce the force required to bring the two lamellae together, enabling them to collapse under minimal forces, such as surface tension. Experimental determination of the friction force involves various setups, such as employing force sensors[35] or measuring the deflection of a glass microneedle.[36] Techniques such as these provide valuable insights into the complex interplay of forces influencing the

Table 1. Wetting Properties of Individual Materials

polymer material	sessile drop CA (deg)	adv. CA (deg) at 90° tilt angle	rec. CA (deg) at 90° tilt angle	adv. CA (deg) inflating	rec. CA (deg) deflating	CA hysteresis
polylactic acid (PLA)	79 ± 3	77 ± 4	53 ± 7	79 ± 3	56 ± 3	23
poly(1,4-butylene adipate)-based polyurethane (PU−PBA)	76 ± 2	88 ± 9	22 ± 16	75 ± 2	67 ± 1	8
poly(dimethylsiloxane) (PDMS)	96 ± 5	98 ± 3	61 ± 4	104 ± 2	91 ± 3	13

dynamics of a sliding droplet. The estimation of the friction coefficient was derived from torque measurements realized with a rheometer MCR 702 MultiDrive from Anton Paar (Figure 3a). The torque (M) is directly proportional to the
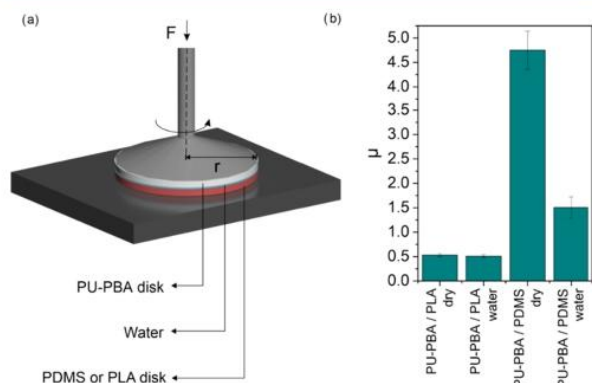
Figure 3. Estimation of the friction coefficient, (a) by measuring the torque at specified forces performed in a rheometer setup, where a disk of PU−PBA was glued to the plate−plate geometry (25 mm) and in the bottom a disk of PLA or PDMS glued to the base for performing the shearing with and without water as a lubricant, and (b) friction coefficient between the materials that constitute the lamella and substrate with and without the presence of water.

friction coefficient and the normal force applied during the measurement. To simulate the wetting conditions during the deformation of the lamellae, water was added between the two disks. The addition of water resulted in a reduction in torque compared with samples without water. This result was explained by the lubricant effect that water had on the two objects. The highest friction coefficient was observed when interacting with the PDMS surface (Figure 3b). This behavior was attributed to the inherent softness and rubbery behavior of cross-linked PDMS—both soft PDMS and relatively soft lamellae can be mutually deformed during contact, which allows a higher contact area compared to the case when two rigid materials are brought in contact with each other. Thus, depending on fabrication, lamellae can have three kinds of contacts with the substrate: strong adhesion (fusion of the bottom of the lamellae to the PLA substrate), intermediate adhesion (lamellae−PDMS contact), and weak adhesion (lamellae with an air gap underneath).

Although we measured the friction coefficient, the obtained value reflects interactions between materials that are moving with respect to each other. However, the coefficient of static friction—relevant at the onset of movement—can differ significantly, as initiating motion requires a force sufficient to overcome the stall force and break the initial contact. Consequently, accurately accounting for the frictional effects between the lamellae and substrates presents a notable challenge.

Sliding Measurements of the Water Drop on a Combined Substrate without Lamellae. Next, the effect of the substrate properties on the sliding of the droplet without lamellae was analyzed by investigating its movement at a tilting angle of 90°—the sample is vertical (Figure 4). First, a 20 μL large droplet of water was initially placed on the PLA side of the PLA−PDMS sample, and it slid to the PDMS part. The velocity of the droplet was calculated by the tracking position of the droplet's leading edge (Figure 4a,b). The velocity of the

sliding droplet for the PLA surface was 0.3 mm/s, and that for PDMS was 1.8 mm/s. From the position of the water droplet versus time, the acceleration was calculated, as shown in Figure S1. Initially, the droplet accelerated under the influence of gravity. When it reached the border between PLA and PDMS substrates, the droplet experienced a significant deceleration, and upon fully transitioning to the PDMS surface, it accelerated rapidly. A considerable change in sliding speed occurred in the region where the droplet crossed the boundary between the two surfaces when its receding edge was on the PLA part and its front (advancing) edge was the PDMS part. During this transition, the velocity of the water droplet dropped to 0.08 mm/s (Figure 4b), accompanied by a decrease in drop length (Figure 4c) and height (Figure 4d). The decrease in the velocity and length of the droplet can be explained by the initial increase of the contact angle hysteresis ($\Delta\theta$): the advancing contact angle (θ_A) on the PDMS surface varied between 100 and 110°, while the receding contact angle (θ_R) on PLA was 45° (Figure S1c). When a small portion of the droplet was in contact with PDMS, the remaining part of the droplet that was in contact with the PLA surface had better wettability than PDMS, making the droplet stay pinned because the borderline prevented the droplet from moving forward. The length of the droplet remains relatively constant around 5 mm, meaning that the droplet slides on the surface; its front and back move. It is important to note that the acceleration of the sliding of the droplet is 0 m/s^2 (Figure S1)—the droplet moved with the contact rate, meaning that the friction force between the droplet and the substrate does not depend linearly on the movement rate. In other words, the friction force reaches the gravity force at the observed speed of sliding.
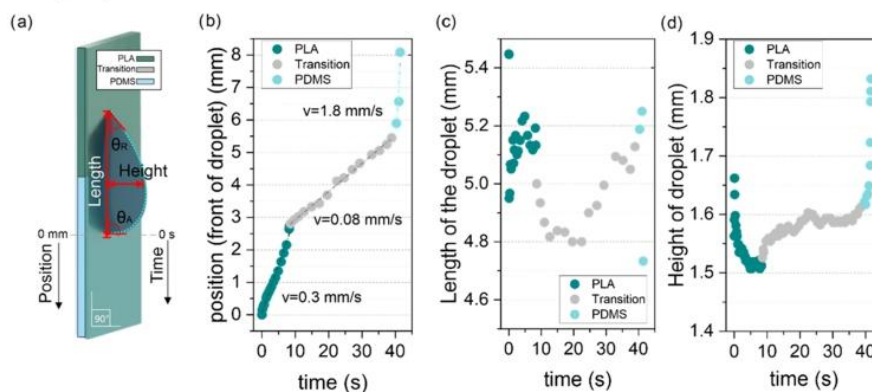
Sliding Measurements of the Lamellar Surface with a Combined Substrate. A similar analysis on a tilting table was made for the PLA- and PDMS-coated glass slide with melt-electrowritten PU−PBA lamellae to understand the contribution of lamellae (Figure 4e−h). At room temperature, a 20 μL water droplet was placed between two lamellae (Figure S1d). As the water slid between the lamellae, the position versus time curve was measured (Figure 4f). The velocity and acceleration were calculated from the first and second derivatives of position (Figure S1b−e).

The presence of lamella had three effects on the sliding water drop: first, an increase in the absolute speed; second, neglect of the effect of the substrate on the velocity of the water drop; and third, elongation of the droplet before the sliding. These effects could be explained by considering the difference in the geometries of structures with and without lamellae. The narrow space between lamellae induces elongation of the droplet, and the deformation of the tops of lamellae allows even greater elongation of the droplet. In contrast, a more spherical droplet on a flat surface without lamellae produces less pressure at its advancing front than an elongated droplet does. This pressure can be approximated by $P = \rho g l \sin \alpha$, where ρ and g are the fluid density and gravitational acceleration, respectively, α is the tilting angle, and l is the length of the droplet, which depends on the presence of lamellae and their collapse by the droplet, thereby enhancing the pressure at the advancing front. In order to provide a better comparison between the sliding of the droplet on a flat surface and a surface with lamellae, we propose to normalize the sliding speed of the droplet because the gravity forces scale with the droplet length (Table 2) to yield a relative
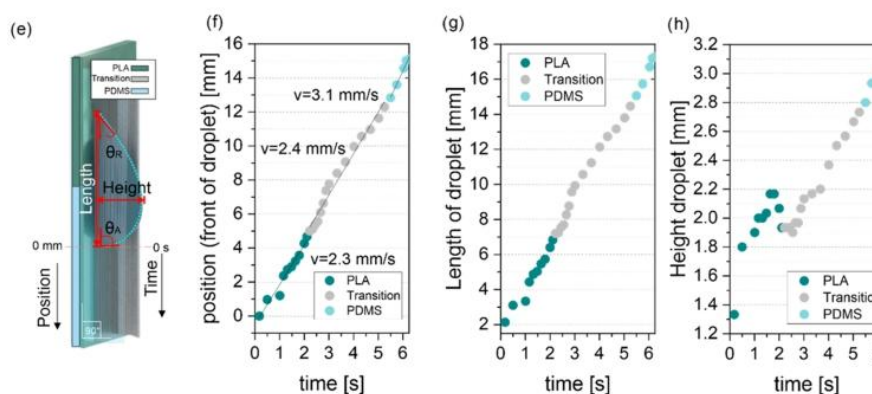
Figure 4. (a−d) Sliding of a water droplet on a combined substrate without lamellae tilted by 90°. (a) Schema of the sliding droplet on combined surfaces without lamellae, (b) advancing position of the droplet versus time, (c, d) the length and height of the sliding droplet on the combined substrate composed of PLA and PDMS. (e−h) Sliding of a water droplet on a combined substrate with a hard lamellar surface tilted by 90°. (e) Schema of the experiment, (f) advancing position of the droplet versus time, (g) the length, and (h) and height of the sliding droplet on the combined substrate composed of PLA−PDMS and the lamellar surface.

Table 2. Normalized Speed of the Sliding Droplet on Surfaces with and without Lamellae

	measured speed rate (mm/s)	droplet length (mm)	relative sliding speed rate (1/s)
droplet on the flat PLA substrate	0.3	5	0.06
droplet on the flat transition state (PLA−PDMS) substrate	0.08	5	0.016
droplet on the flat PDMS substrate	1.8	5	0.36
droplet between lamellae written on the PLA substrate	2.3	17.3	0.13
droplet between the transition state (PLA−PDMS) substrate	2.4	17.3	0.14
droplet between lamellae written on the PDMS substrate	3.1	17.3	0.18

sliding speed rate (1/s) of the droplet. This normalization provides qualitative estimation, as the droplet is not a cylinder with a certain length and constant width and height— the width and height change along with the length of the droplet and also depend on material properties, which define the shape

of the droplet. While lamellae increase absolute values of sliding speed on both PAL and PDMS (Figure 4), the normalized speed increases on moderately hydrophobic PLA and decreases on hydrophobic PDMS (Table 2).

The contact area of the water droplet on surfaces with lamellar topography is considerably higher in comparison with that on surfaces without lamellae (Figure S2). As a result, the contact area of the water droplet with the surface in combination with the capillary effect accelerated the motion of the droplet along the grooves. The contact droplet with lamellae (1.5 mm high each, considering two lamellae) was comparable to the distance between them (3 mm), leading to a significant contribution of droplet−lamellae interactions to sliding properties.

The sliding forces acting on a droplet can be expressed as a difference of gravity force $F_g \sim k_1 \, mg$, where k_1 is a coefficient related to the shape of the droplet, and friction forces proportional to the difference in receding and advancing contact angles $F_f \sim k_2 \, L\gamma(\cos \theta_{rec} - \cos \theta_{adv})$,[23,37] where k_2 is a dimensionless factor related to the shape of the three-phase contact line (solid, liquid, and air), L is the droplet diameter, γ is the surface tension of water, and θ_{rec} and θ_{adv} are the receding and advancing contact angles, respectively. Introducing lamellae changes k_1, k_2, and $\cos \theta_{rec} - \cos \theta_{adv}$, the droplet
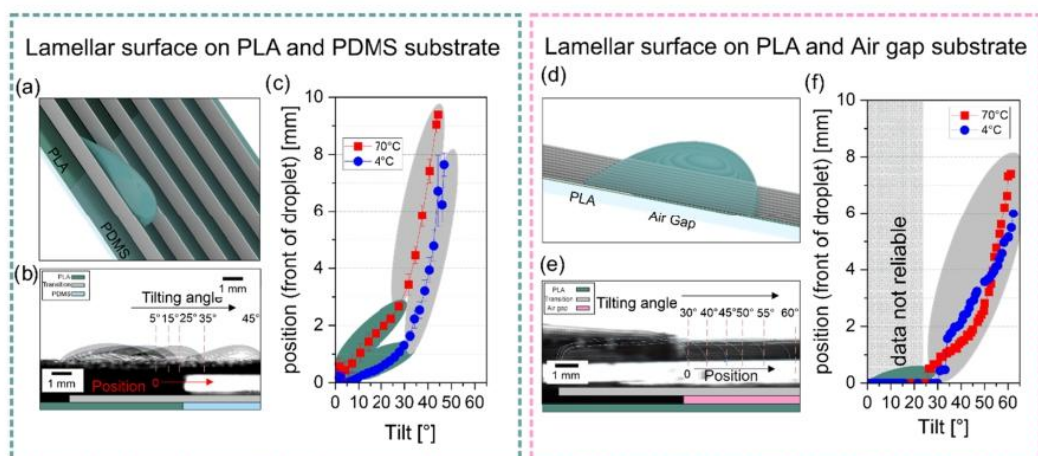
Figure 5. Sliding droplet at increasing tilting angles on the lamellar surface on a combined surface of PLA and PDMS, (a) schema of the experiment, (b) imaging of the sliding droplet at different times, and (c) position of the droplet versus tilting angle. The sliding droplet on the lamellar surface on the PLA−Air gap surface, (d) schema of the experiment, (e) imaging of the sliding droplet at different times, and (f) position of the droplet versus tilting angle.

becomes more elongated, and, as discussed above, it increases the gravity force and reduces the average value of $\cos\theta_{rec} - \cos\theta_{adv}$ (it is 0.13 for PEU−PU and 0.36 for PLA). Thus, the reason for the increase in sliding speed in the presence of lamellae is the elongated shape of the drop and the more hydrophobic properties of the material of the lamellae than the material of the substrate.

Effect of Tilting Angle on Deformation of Free-Standing Lamellae on Combined PLA−PDMS and PLA−AIR Surfaces at Soft and Rigid States. Droplet sliding measurements at an increased tilting angle were performed for cantilever-like lamellae with different substrates: PLA−AIR and PLA−PDMS when the PU−PBA lamellae were in a rigid and soft state (Figure 5). To understand the effect of the mechanical properties of lamellae on sliding behavior, a 40 μL droplet slid along the lamellae at temperatures of 70 °C (soft PU−PBA lamellae) and 4 °C (rigid PU−PBA lamellae). The measurement schemas are shown in Figure 5a for the PLA−PDMS substrate and in Figure 5d for the lamellar surface on the PLA−AIR substrate. At a tilting rate of 120°/min, the position (Figure 5c−f), length of the droplet, and height were measured (Figure S3). The stacked images of a droplet on the PLA−PDMS substrate were taken after 5, 15, 25, 35, and 45° tilting angles (Figure 5b). For PLA−AIR, the images show the droplet advancement at 30, 40, 45, 50, 55, and 60° tilting angles (Figure 5e). In this experiment, two variables are changed simultaneously: tilting angle and the material of the substrate (droplet during sliding moved from one material to another). Therefore, only the parts of the curves corresponding to the same materials can be compared. When analyzing the position of the droplet and its velocity on the lamellae−PLA−PDMS substrate (Figure 5c), it was observed that the droplet slid faster when the temperature was 70 °C than at 4 °C. The same experiment was done for the lamellar surface on the PLA−Air gap substrate (Figure 5f). In both cases, the position and velocity of the sliding droplet at 70 °C (soft lamellae) are higher than those at 4 °C (stiff lamellae). Moreover, we observed an acceleration of the droplet on the air gap side of the lamellae (PLA−Air gap substrate). Faster sliding at elevated temperatures can be explained by deformation of lamellae, which reduces the distance between them and is also

an effect of the reduction of the elastic modulus of the lamellae, making them softer. The reduction of the distance is expected to be stronger when the lamellae have poor adhesion to the substrate (Air gap) and both their lower and upper parts are able to move.

Analysis of Deformation of Lamellae by a Droplet. Deformation studies were conducted on lamellae placed on both different substrates: PLA−PDMS and PLA−Air gap (Figure 6) to understand the origin of the change in the speed of droplet movement described in Figure 5. First, the lamellar surface was exposed to 4 °C to switch the lamellar state to a rigid state, and a large droplet was allowed to slide between the two lamellae. When the substrate was PLA−PDMS, the rigid lamellae were undeformed (Figure 6b−e). The negligible bending of the top of rigid lamellae, observed in Figure 6c at 24 and 30 s, was explained by the large height of the lamellae—the higher the lamella, the stronger the deformation.

$$\delta \sim \frac{l^3}{Eh^3} \tag{4}$$

Here, l is the height of the lamella, h is its thickness, and E is the modulus. On the other hand, the increase of temperature to 70 °C resulted in the bending of the upper layer, while the lower part of the lamellae remained unaffected (Figure 6d,e). Since the friction force is significant, more force is required to move the lamellae at the lower layer compared to the upper layer. As the water slid onto the surface, the deformed lamellae recovered their initial shape. The deformation and collapsing of the lamellae by the elastocapillarity effect were also explained by the interaction of the lamellae with their substrate.

The analysis of the deformation of the free-standing section of lamellae on the PLA−Air gap surface (Figure 6f−m) revealed that, despite not being physically attached to the substrate (air gap), the lamellae experienced friction force, restricting the movement of the lamellae on the substrate surface; the lower part of lamellae was partially mobile when it was both in rigid and soft states. Thus, the behavior of lamellae on the PLA−Air gap substrate was different from that on the PLA−PDMS substrate: the water droplet was able to collapse
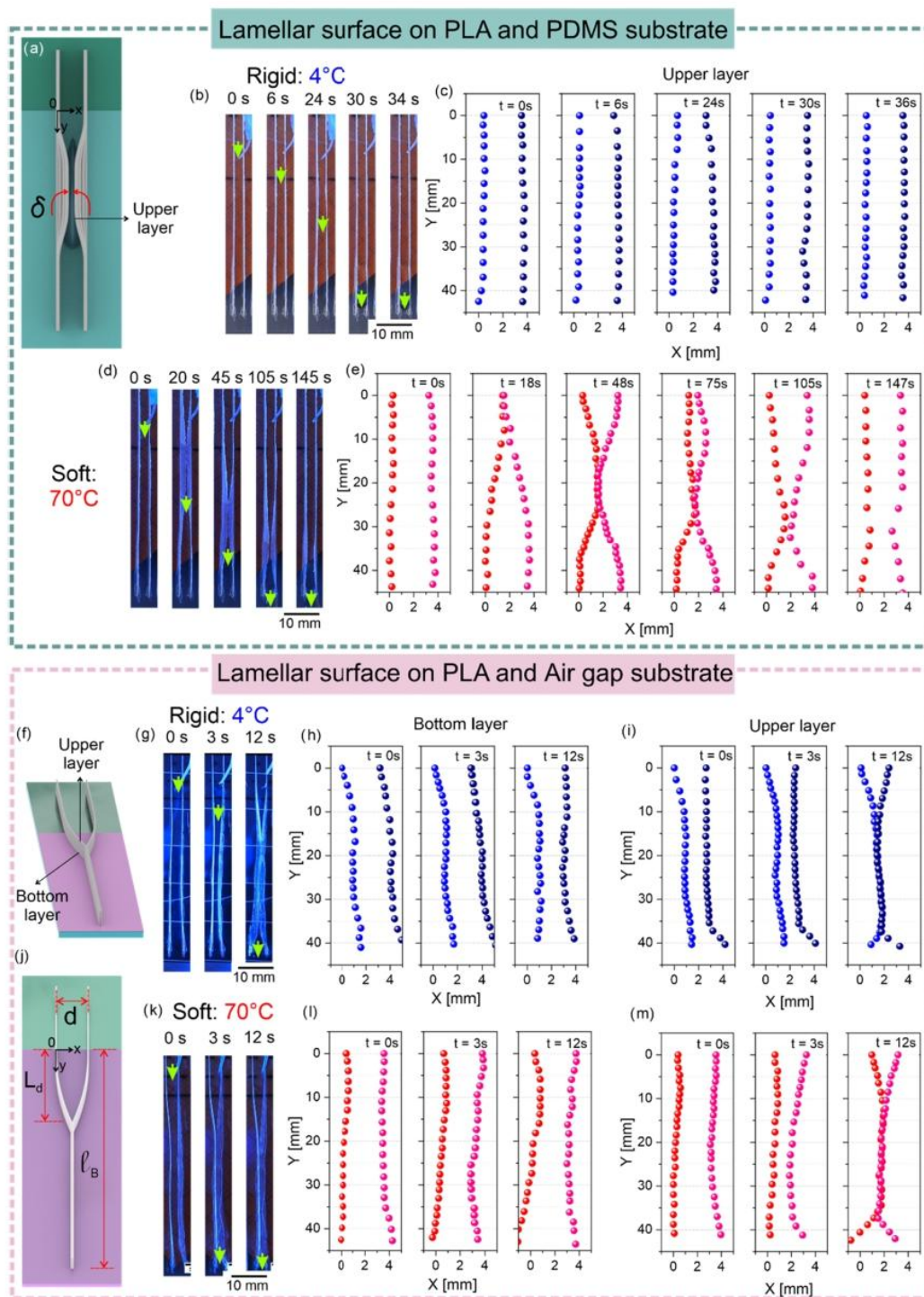
Figure 6. Deformation of the free-standing lamella on PLA−PDMS and PLA−Air. (a) Schema of the lamellae deposited partially on PLA and the remaining section of lamellae on PDMS; here, δ is shown as the deflection of the lamellae. (b, d) Images of the lamellae deposited on PLA−PDMS (top view) at 4 and 70 °C, respectively. (c, e) Digitalization of the position of the lamellae at 4 and 70 °C. (f, j) The schema of the lamellae deposited partially on PLA and the other section remains free-standing (Air gap). In the schema, d is the distance between two neighboring lamellae, l_B is the length of bending, and L_d is the spacing length. (g, k) Images of the deformation of lamellae at 4 and 70 °C, respectively. Digitalization of the position of the lamellae measured by the position of the lower layer (h, l) and upper layer (i, m) at 4 and at 70 °C, respectively.

the lamellae together in the PLA−Air gap case, even when lamellae were in both rigid and soft states. In other words, on the PLA−Air gap substrate, the collapse of the free-standing part of the lamellae was independent of the mechanical
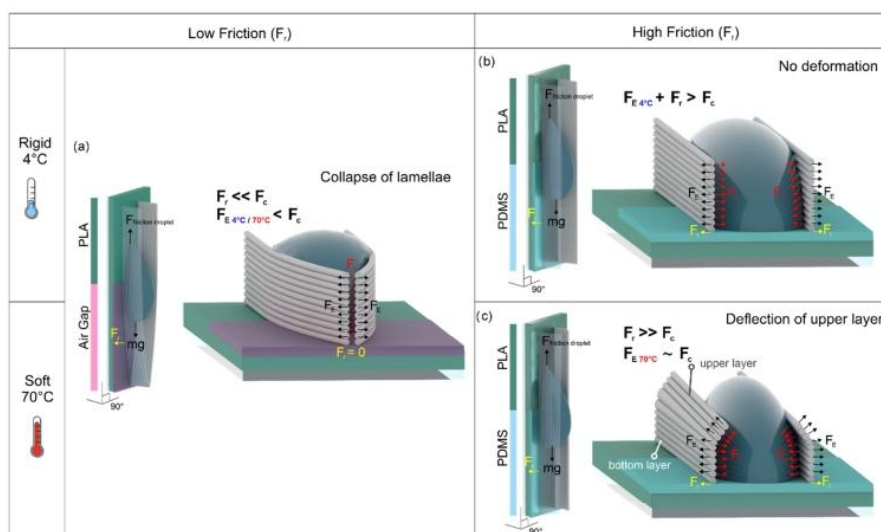
Figure 7. Schema of the deformation of the lamellae when they are slid at a tilting angle of 90° (a, b) on the PLA−PDMS substrate at 4 °C (rigid state of lamellae) and 70 °C (soft state of the lamellae). (c) Deformation of lamellae on the PLA−Air Gap substrate at different temperatures (4 and 70 °C).

properties of the material, as observed in Figure 6f−k. Summing up, on PLA−PDMS, the lamella was restricted from two sides: (i) the lower part in contact with the PDMS substrate and (ii) the line where it connected to the fixed section on the PLA substrate. In the case of the PLA−Air gap substrate, the lamella was restricted only from one side: the line where it connected to its part fixed on the PLA substrate. Following this analysis, it became evident that the deformation or collapsing of two neighboring long-free-standing lamellae was independent of the elastic modulus of the material.

In order to explain the observed phenomenon, we considered the spacing length (L_d; Figure 6a) between the collapsed part of the lamella and the end of its fixed part, which can be expressed as[10,38]

$$L_d \sim l_B^{1/2} \cdot d^{1/2} \tag{5}$$

where d is the distance between lamellae. The length of bending (l_B) was calculated for a thin lamella where the thickness was much smaller than the width, given as follows.

$$l_B = \sqrt{\frac{Et^3}{24(1-\nu^2)\gamma}} \tag{6}$$

In this equation, E represents the elastic modulus of the polymer, t is the thickness of the lamella, ν is Poisson's ratio (typically between 0.48 and 0.5 for polyurethanes),[39] and γ is the surface tension of water.[38,40] l_B was calculated using this equation for the lamellae with high and low elastic moduli— rigid and soft states. The results showed that when E was high (55 MPa at 4 °C),[12] a minimum length of 12 mm was required to be deformed by the capillary force of water. Then, l_B was calculated for low E (8 MPa at 70 °C),[12] which resulted in a minimum length of 4.9 mm. The length of the lamellae in our experimental samples exceeded both values of l_B. It was around 46 mm, meaning that lamellae must deform at any temperature when they have no friction with the substrate. L_d was calculated for the lamellae at 70 and 4 °C by using the estimated value of l_B. The calculated L_d for soft lamellae was

3.8 mm, while for rigid lamellae, it was 6 mm. Nevertheless, the experimentally obtained values of L_d were significantly higher than the calculated ones: 11.6 ± 1.6 nm for soft lamellae and 9.9 ± 0.3 mm for rigid lamellae. After the statistical analysis, L_d in the rigid and soft states showed no significant differences at $p = 0.05$. It is important to note that these approximations were made for thin rods and lamellae not in contact with other substrates. L_d values calculated from these equations were nearly three and two times smaller than the actual measured value for soft and rigid states, respectively, indicating a significant influence of friction forces from the substrates on lamella coalescence.

Applied Forces on the Deformation of the Cantilever-Like Lamellae. When assessing the forces acting on the sliding of the lamellae on the substrates, one can conceptualize it as an object in motion on a tilted surface, primarily propelled by gravity (g; Figure 7). The forces that intervene in the deformation of two neighboring lamellae while sliding a droplet between two lamellae are explained by (i) the water drop with capillarity force (F_C) that pulls the lamellae together.[41] Capillary forces (F_C) increase with deformability (softness) of lamellae, as softness decreases the distance between lamellae. (ii) The opposite force avoiding the deformation of the lamellae is the elastic force (F_E),[41] which is affected by the elastic modulus (E) and the geometry of the lamellae (thickness and height). Since the geometry of the lamellae remains constant, F_E depends strongly on the elastic modulus of the material. F_E at 4 °C is calculated based on the elastic modulus of PU−PBA (~55 MPa) after crystallization of the polymer chains. In contrast, F_E at 70 °C corresponds to the elastic modulus (~8 MPa) when the polymer chains are in a fully amorphous state and (iii) the friction force (F_r) between the lamellae and its substrate (Figure 3). F_r depends on the interactions between the lamella and the substrate. The contact of two soft materials exhibits a higher F_r as presented between the lamella and PDMS. The interplay between these three forces results in different types of deformation of both lamellae on various substrates. A high elastic force combined with a high friction force (rigid lamellae on the PLA−PDMS surface)

hinders the deformation of the lamellae. Low elastic force, on the other hand, leads to stronger deflection of the lamellae. However, when the lamellae are soft, a high friction force still hinders the deformation of the lower part of the lamellae, which also restricts, but does not completely limit, the deformation of the top part (soft lamellae on the PLA−PDMS surface). When the friction force is low (as seen with cantilever-like lamellae standing on a PLA−Air gap substrate; Figure 7c), the capillary force always exceeds the elastic force, leading to the collapse of the lamellae in both their rigid and soft states. Since the length of the lamellae exceeds the maximum bending length (l_B), their collapse becomes independent of temperature (and the softness/rigidity of the lamellae) due to the dominance of capillary forces.

CONCLUSIONS

In conclusion, an approach for the fabrication of free-standing PU−PBA lamellae, cantilever-like, was made involving strategic modifications to the substrate. We employed different polymer coatings to control the mobility of one lamella section while allowing the other to move freely. The use of polylactide (PLA) and poly(dimethylsiloxane) (PDMS) coatings and the soluble poly(vinyl alcohol) (PVA) layer to create an air gap under the lamellae enabled precise adhesion and nonadherence of different lamella sections. The substrate properties played an important role in the sliding behavior of water droplets, as demonstrated by the sliding experiments. The experimental determination of friction coefficients revealed that soft PDMS substrates demonstrate the highest friction force with the lamellae material, while water, acting as a lubricant, reduced the frictional force between the surfaces. The sliding drop analysis showed that the droplet exhibited different velocities on PLA and PDMS surfaces, with notable acceleration and deceleration at the substrate interface and rolling down onto the PDMS side. This comprehensive analysis provides insights into the dynamic interplay between the substrate properties and water droplet behavior on heterogeneous surfaces. Nevertheless, samples that included the lamellar surface revealed that the velocities in both substrates remain similar, showcasing capillarity-driven acceleration along the lamellar grooves. Moreover, deformation studies on lamellae at different temperatures showed temperature-dependent behavior. At 4 °C, rigid-state lamellae exhibited minimal deformation. At 70 °C, soft-state lamellae showed a more pronounced bending of the top layer due to the dominance of capillary forces over the elastic forces. The recovery of deformation occurred as the water droplet moved along the lamellae, emphasizing the role of capillary forces and lateral adhesion in this process. On PDMS surfaces, free-standing lamellae exhibited stronger friction forces, preventing significant movement. Nevertheless, for lamellae on the PLA−Air gap substrate, the capillary forces were higher than the elastic forces of the material, leading to their collapse.

In our previous research, we explored the applicability of the surface for fabricating smart valves in microfluidics. The free-standing lamellae can be applied to control the fluid passage by closing or opening the groove through a combination of substrates. Overall, this study analyzes the capillary-driven dynamics and surface interactions that influence water droplet behavior on lamellar surfaces, offering valuable insights for applications such as folding processes for soft robotics. Future investigations should consider friction forces as a crucial parameter in understanding and predicting the behavior of deforming structures.

ASSOCIATED CONTENT

Ⓢ Supporting Information

The Supporting Information is available free of charge at https://pubs.acs.org/doi/10.1021/acs.langmuir.5c02002.

> Sliding of a water droplet on a combined substrate (PLA−PDMS) without lamellae tilted by 90° (Figure S1); schema of the contact area of a water drop (Figure S2); schema of the sliding droplet at increasing tilting angle on the lamellar surface on the PLA−PDMS substrate and on the PLA−Air gap substrate (Figure S3); schema of the shape memory effect of the surface when a water droplet slides into the grooves (Figure S4); and schema of the forces in the sliding droplet between two lamellae (Figure S5) (PDF)
> Sliding droplet 90 PLA−PDMS with lamellae (MP4)
> Sliding droplet 90_PLA−PDMS no lamellae (MP4)
> 4 °C PLA−PDMS lamella inc tilt (MP4)
> 70 °C PLA−PDMS lamellae inc tilt (MP4)
> PLA−Air gap 4 °C lamellae inc tilting angle (MP4)
> PLA−Air gap 70 °C lamellae inc tilting angle (MP4)
> PLA−Air gap 4 °C lamellae (MP4)
> PLA−Air gap 70 °C lamellae (MP4)
> PLA−PDMS 4 °C lamellae (MP4)
> PLA−PDMS 704 °C lamellae (MP4)

AUTHOR INFORMATION

Corresponding Author

Leonid Ionov − *Faculty of Engineering Sciences, University of Bayreuth, 95447 Bayreuth, Germany; Bavarian Polymer Institute, University of Bayreuth, 95447 Bayreuth, Germany;* ● orcid.org/0000-0002-0770-6140; Email: leonid.ionov@uni-bayreuth.de

Authors

Gissela Constante − *Faculty of Engineering Sciences, University of Bayreuth, 95447 Bayreuth, Germany*

Dennis Schönfeld − *Fraunhofer Institute for Applied Polymer Research IAP, 14476 Potsdam, Germany*

Thorsten Pretsch − *Fraunhofer Institute for Applied Polymer Research IAP, 14476 Potsdam, Germany*

Pavel Milkin − *Faculty of Engineering Sciences, University of Bayreuth, 95447 Bayreuth, Germany;* ● orcid.org/0000-0002-4474-885X

Ilia Sadilov − *Faculty of Engineering Sciences, University of Bayreuth, 95447 Bayreuth, Germany;* ● orcid.org/0000-0001-7944-1754

Complete contact information is available at:
https://pubs.acs.org/10.1021/acs.langmuir.5c02002

Author Contributions

The manuscript was written through the contributions of all authors. All authors have given approval to the final version of the manuscript.

through the German Federation of Industrial Research Associations (Project 19820 BR).

Notes

The authors declare no competing financial interest.

■ REFERENCES

(1) Weijs, J. H.; Andreotti, B.; Snoeijer, J. H. Elasto-capillarity at the nanoscale: on the coupling between elasticity and surface energy in soft solids. *Soft Matter* **2013**, *9* (35), 8494−8503.

(2) Holmes, D. P.; Brun, P. T.; Pandey, A.; Protière, S. Rising beyond elastocapillarity. *Soft Matter* **2016**, *12* (22), 4886−4890.

(3) Ha, J.; Kim, Y. S.; Jiang, K.; Siu, R.; Tawfick, S. Hydrodynamic Elastocapillary Morphing of Hair Bundles. *Phys. Rev. Lett.* **2020**, *125* (25), No. 254503.

(4) Samy, R. A.; Suthanthiraraj, P. P. A.; George, D.; Iqbal, R.; Sen, A. K. Elastocapillarity-based transport of liquids in flexible confinements and over soft substrates. *Microfluid. Nanofluid.* **2019**, *23* (8), 100.

(5) Yousafzai, M. S.; Yadav, V.; Amiri, S.; Staddon, M. F.; Errami, Y.; Jaspard, G.; Banerjee, S.; Murrell, M. Cell-Matrix Elastocapillary Interactions Drive Pressure-Based Wetting of Cell Aggregates. *Phys. Rev. X* **2022**, *12* (3), No. 031027.

(6) Zhang, Y.; Yin, M.; Xu, B. Elastocapillary rolling transfer weaves soft materials to spatial structures. *Sci. Adv.* **2023**, *9* (34), No. eadh9232.

(7) Wei, Z.; Schneider, T. M.; Kim, J.; Kim, H.-Y.; Aizenberg, J.; Mahadevan, L. Elastocapillary coalescence of plates and pillars. *Proc. R. Soc. A* **2015**, *471* (2175), No. 20140593.

(8) Samy, R. A.; Satpathi, N. S.; Sen, A. K. Elastocapillary interaction between a long rectangular membrane and a liquid drop. *Soft Matter* **2021**, *18* (1), 228−235.

(9) Tian, Y.; Liang, H.; Dobrynin, A. V. Elastocapillarity and rolling dynamics of solid nanoparticles on soft elastic substrates. *Soft Matter* **2020**, *16* (9), 2230−2237.

(10) Bico, J.; Roman, B.; Moulin, L.; Boudaoud, A. Elastocapillary coalescence in wet hair. *Nature* **2004**, *432* (7018), 690.

(11) Durand, M. Mechanical approach to surface tension and capillary phenomena. *Am. J. Phys.* **2021**, *89* (3), 261−266.

(12) Constante, G.; Apsite, I.; Auerbach, P.; Aland, S.; Schönfeld, D.; Pretsch, T.; Milkin, P.; Ionov, L. Smart Mechanically Tunable Surfaces with Shape Memory Behavior and Wetting-Programmable Topography. *ACS Appl. Mater. Interfaces* **2022**, *14* (17), 20208−20219.

(13) Das, S.; Marchand, A.; Andreotti, B.; Snoeijer, J. H. Elastic deformation due to tangential capillary forces. *Phys. Fluids* **2011**, *23* (7), No. 072006.

(14) Apsite, I.; Salehi, S.; Ionov, L. Materials for Smart Soft Actuator Systems. *Chem. Rev.* **2022**, *122* (1), 1349−1415.

(15) Py, C.; Reverdy, P.; Doppler, L.; Bico, J.; Roman, B.; Baroud, C. N. Capillary Origami: Spontaneous Wrapping of a Droplet with an Elastic Sheet. *Phys. Rev. Lett.* **2007**, *98* (15), No. 156103.

(16) Chen, T.; Bakhshi, H.; Liu, L.; Ji, J.; Agarwal, S. Combining 3D Printing with Electrospinning for Rapid Response and Enhanced Designability of Hydrogel Actuators. *Adv. Funct. Mater.* **2018**, *28* (19), No. 1800514.

(17) Ionov, L. 3D Microfabrication using Stimuli-Responsive Self-Folding Polymer Films. *Polym. Rev.* **2013**, *53* (1), 92−107.

(18) Evans, A. A.; Spagnolie, S. E.; Bartolo, D.; Lauga, E. Elastocapillary self-folding: buckling, wrinkling, and collapse of floating filaments. *Soft Matter* **2013**, *9* (5), 1711−1720.

(19) Azam, A.; Laflin, K. E.; Jamal, M.; Fernandes, R.; Gracias, D. H. Self-folding micropatterned polymeric containers. *Biomed. Microdevices* **2011**, *13* (1), 51−58.

(20) Stoychev, G.; Puretskiy, N.; Ionov, L. Self-folding all-polymer thermoresponsive microcapsules. *Soft Matter* **2011**, *7* (7), 3277−3279.

(21) Jerison, E. R.; Xu, Y.; Wilen, L. A.; Dufresne, E. R. Deformation of an Elastic Substrate by a Three-Phase Contact Line. *Phys. Rev. Lett.* **2011**, *106* (18), No. 186103.

(22) Karpitschka, S.; Das, S.; van Gorcum, M.; Perrin, H.; Andreotti, B.; Snoeijer, J. H. Droplets move over viscoelastic substrates by surfing a ridge. *Nat. Commun.* **2015**, *6* (1), No. 7891.

(23) Gao, N.; Geyer, F.; Pilat, D. W.; Wooh, S.; Vollmer, D.; Butt, H.-J.; Berger, R. How drops start sliding over solid surfaces. *Nat. Phys.* **2018**, *14* (2), 191−196.

(24) Constante, G.; Apsite, I.; Schönfeld, D.; Pretsch, T.; Ionov, L. Reversibly Photoswitchable High-Aspect Ratio Surfaces. *Small Struct.* **2023**, *4* (10), No. 2300040.

(25) Ha, J.; Kim, Y. S.; Siu, R.; Tawfick, S. Dynamic pattern selection in polymorphic elastocapillarity. *Soft Matter* **2022**, *18* (2), 262−271.

(26) Uribe-Gomez, J.; Schönfeld, D.; Posada-Murcia, A.; Roland, M.-M.; Caspari, A.; Synytska, A.; Salehi, S.; Pretsch, T.; Ionov, L. Fibrous Scaffolds for Muscle Tissue Engineering Based on Touch-Spun Poly(Ester-Urethane) Elastomer. *Macromol. Biosci.* **2022**, *22* (4), No. 2100427.

(27) Pasini, C.; Soreño, Z. V.; Schönfeld, D.; Pretsch, T.; Constante, G.; Sadilov, I.; Ionov, L. 4D Fabrication of Two-Way Shape Memory Polymeric Composites by Electrospinning and Melt Electrowriting. *Macromol. Rapid Commun.* **2024**, *45* (11), No. 2400010.

(28) Gleadall, A. FullControl GCode Designer: Open-source software for unconstrained design in additive manufacturing. *Addit. Manuf.* **2021**, *46*, No. 102109.

(29) Valerio, O.; Misra, M.; Mohanty, A. K. Statistical design of sustainable thermoplastic blends of poly(glycerol succinate-co-maleate) (PGSMA), poly(lactic acid) (PLA) and poly(butylene succinate) (PBS). *Polym. Test.* **2018**, *65*, 420−428.

(30) Król, P.; Król, B. Surface free energy of polyurethane coatings with improved hydrophobicity. *Colloid Polym. Sci.* **2012**, *290*, 879−893.

(31) Zhai, M.; McKenna, G. B. In *Surface Energy of a Polyurethane as a Function of Film Thickness*, Proeedings of the Annual Technology Conerence SPE ANTEC, 2014.

(32) Vudayagiri, S.; Junker, M. D.; Skov, A. L. Factors affecting the surface and release properties of thin polydimethylsiloxane films. *Polym. J.* **2013**, *45* (8), 871−878.

(33) Kuo, A. C. Poly(dimethylsiloxane). In *Polymer Data Handbook*; Wiley, 1999; Vol. 2.

(34) Constante, G.; Apsite, I.; Alkhamis, H.; Dulle, M.; Schwarzer, M.; Caspari, A.; Synytska, A.; Salehi, S.; Ionov, L. 4D Biofabrication Using a Combination of 3D Printing and Melt-Electrowriting of Shape-Morphing Polymers. *ACS Appl. Mater. Interfaces* **2021**, *13* (11), 12767−12776.

(35) Backholm, M.; Molpeceres, D.; Vuckovac, M.; Nurmi, H.; Hokkanen, M. J.; Jokinen, V.; Timonen, J. V. I.; Ras, R. H. A. Water droplet friction and rolling dynamics on superhydrophobic surfaces. *Commun. Mater.* **2020**, *1* (1), 64.

(36) Suda, H.; Yamada, S. Force Measurements for the Movement of a Water Drop on a Surface with a Surface Tension Gradient. *Langmuir* **2003**, *19* (3), 529−531.

(37) Li, X.; Bodziony, F.; Yin, M.; Marschall, H.; Berger, R.; Butt, H.-J. Kinetic drop friction. *Nat. Commun.* **2023**, *14* (1), No. 4571.

97

(38) Roman, B.; Bico, J. Elasto-capillarity: deforming an elastic structure with a liquid droplet. *J. Phys.: Condens. Matter* **2010**, *22* (49), No. 493101.

(39) Tsukinovsky, D.; Zaretsky, E.; Rutkevich, I. Material Behavior in Plane Polyurethane-Polyurethane Impact with Velocities from 10 to 400 m/sec. *J. Phys. IV France* **1997**, *07* (C3), C3-335−C3-339.

(40) Neukirch, S.; Roman, Bt.; de Gaudemaris, Bt.; Bico, J. Piercing a liquid surface with an elastic rod: Buckling under capillary forces. *J. Mech. Phys. Solids* **2007**, *55* (6), 1212−1235.

(41) Sadilov, I.; Constante, G.; Dulle, M.; Schönfeld, D.; Pretsch, T.; Ionov, L. Reversibly Switchable Topography Enabled by Melting and Crystallization of Melt-Electrowritten Polymer Fibers. *ACS Mater. Lett.* **2025**, *7* (2), 401−408.

Supplementary information

Switchable elastocapillarity of high aspect ratio topographically structured surfaces

Gissela Constante[1], Dennis Schönfeld[2], Thorsten Pretsch[2]; Pavel Milkin[1], Ilia Sadilov[1], and Leonid Ionov[1,3]*

[1] Faculty of Engineering Sciences, University of Bayreuth, Ludwig Thoma Str. 36A, 95447 Bayreuth, Germany

[2] Fraunhofer Institute for Applied Polymer Research IAP, Geiselbergstr. 69, 14476 Potsdam, Germany

[3] Bavarian Polymer Institute, University of Bayreuth, 95447 Bayreuth, Germany.

[*] E-mail: leonid.ionov@uni-bayreuth.de
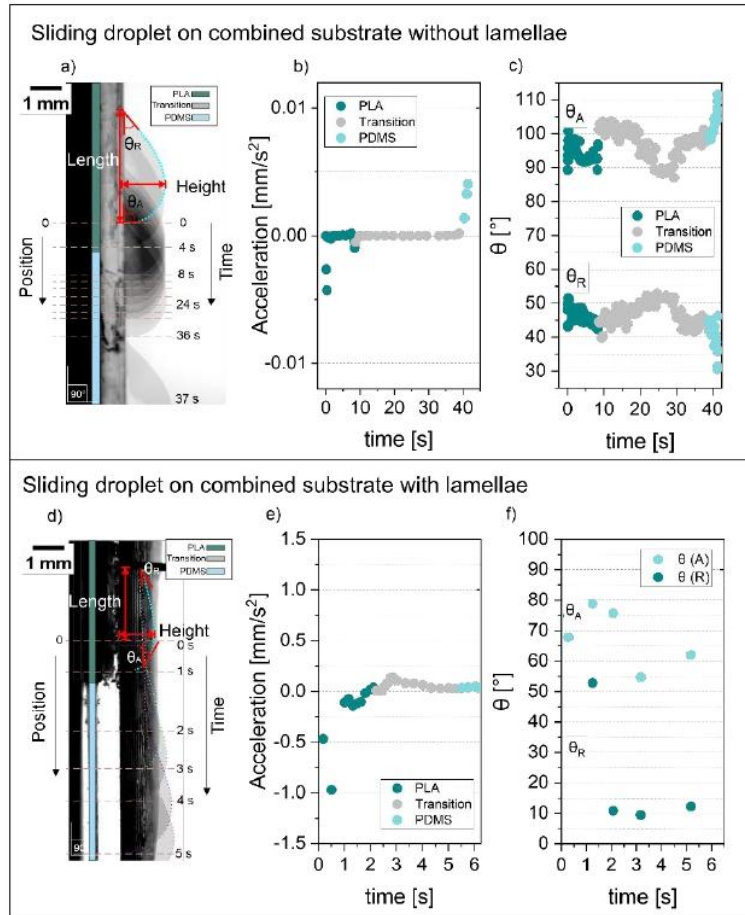
Figure S1. Sliding of water droplet on combined substrate (PLA-PDMS) without lamellae tilted by 90˚, a) images stack at different times, b) acceleration of the droplet, c) measured contact angle advancing and receding. Sliding of water droplet on combined substrate with lamellae tilted by 90˚, d) images stack at different times, e) acceleration of the droplet, f) measured contact angle advancing and receding.

Contact area of water drops on surfaces with and without lamellae. To explain observed behavior on the surface with lamellae, we propose the following estimation of the contact area of the water droplet. The contact area between the droplet and the substrate depends on the properties of the substrate. On a smooth surface without lamellae, the contact area beneath the droplet can be modeled as an oval (**Figure S2**). Conversely, when the water droplet is placed between the lamellae, the contact area with the topographical surface increases due to the confinement within the grooves by surrounding walls (**Figure S2**). To facilitate calculations, we considered the area beneath the droplet as an ellipse, while the lateral interaction with the lamella was conceptualized as a rectangle (**Figure S2**). The area of the ellipse is $Area_{ellipse} = r \cdot b \cdot \pi$, and for the rectangles $Area_{rectangle} = w \cdot l$. Where: r is the minor radius of the droplet, b is the major radius of the droplet, w is the height of the water drop in contact with the lamella, and l is the length of the droplet. Since b is dependent on the variation of the length of the droplet, we estimated b by the volume of ellipsoids equation ($V_{ellipse} = \frac{4}{3}\pi \cdot a \cdot b \cdot r$; where, a is the half of the height of the water drop). From this estimation: b is 6.4 mm, and the calculated area of the bottom of the water drop is 30 mm². While for the droplet between the lamellae, $l=2b$, results in an area of 19 mm². In conclusion, for the water droplet that is on the surface, the contact area was 30 mm², and for the water droplet between the lamellae was 68 mm². In other words, the contact area of the droplet with lamellae is considerable and significantly affects the movement of the droplet.
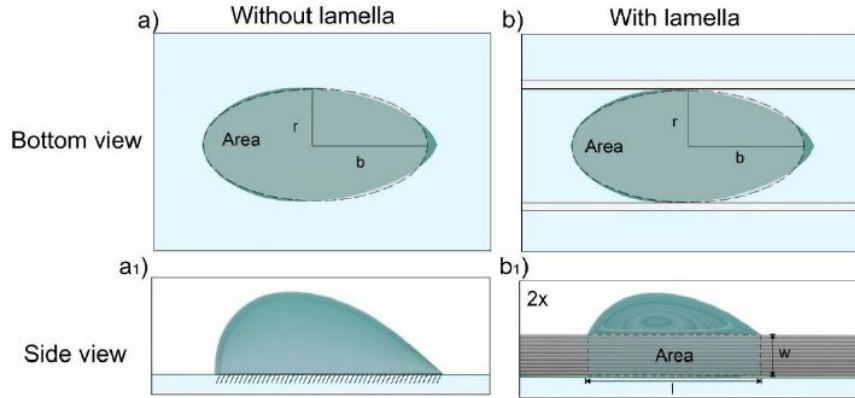
Figure S2. Schema of the contact area of a water drop, a) bottom view under the droplet on the flat surface and b) between the lamellae. a1) side view of the water drop without lamella and b1) with the lamellar surface.

Sliding of water droplet on soft and hard surfaces at increasing tilting angle. A sliding droplet was placed initially on the PLA substrate between two lamellae. The droplet slid while the tilting angle increased. When the droplet passed from the PLA surface to the PDMS surface, the droplet reduced its length and roll off. The fast rolling of the droplet was explained by the hydrophobicity of the surface (**Figure S3b**). For the substrate PLA-Air gap, as the droplet slid across PLA-Air gap, the length increased, suggesting that the water did not roll down but adhered to the lamella due to the capillary effect (**Figure S3e**). As the tilting angle increased, the water droplet increased its length until it left the surface. The capillary effect seemed stronger at elevated temperatures. The combination of capillary effects in narrow channels and lamellae deformation resulted in a decrease in lamellae spacing. This interspacing reduction facilitated the rapid elongation of the water droplet.

We analyzed the droplet height on both surfaces, as illustrated in **Figure S3c and f**. The height of the droplet was measured as the distance between the bottom of the lamellae and the top of the droplet (**Figure S3a and d**). **Figure S3c** represents the data obtained for surface PLA and PDMS, and it showed a notable reduction in the height of the water droplet with increasing tilting angle. This reduction can be explained by the water evaporation upon heating the sample to 70 °C. In contrast, the height remained unchanged when measured at 4 °C. However, when the water droplet slid on the PDMS surface at 70 and 4 °C, the height increased, likely attributed to the rolling of the drop. In the case of PLA-Air gap (**Figure S3f**), the height remained mostly consistent. No distinguishable difference in droplet height was observed between 70°C and 4°C on the PLA-Air gap substrate. This observation is different for the PDMS surface. The possible explanation for the different behavior of droplets on PLA-Air gap and PLA-PDMS surfaces at 70°C is the reduction of distance between the lamellae on the PLA-Air gap surface, which squeezes the water droplet preserving the initial height.
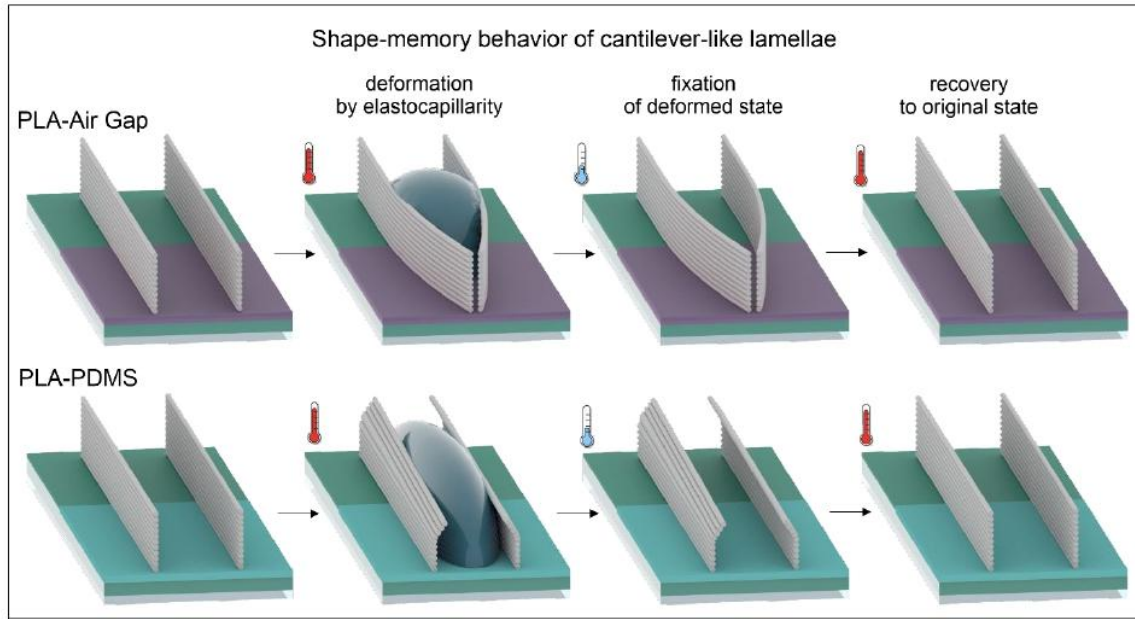
Figure S4. Schema of the shape memory effect of the surface when a water droplet slid into the grooves.

In our previous publication[1], the deformation of fixed lamellae were determined by the interplay of buckling force, capillary force and elastic force. In our scenario, buckling force is neglected due to its low expansion during heating, and, we include the friction force between the free-standing lamella and its substrate. In summary, the forces presented in the front plane, the elastic force and friction force are antagonist to capillary force for deformation of lamellae. As explained before, when the analysis of the sliding droplet is made in different plane (**Figure S5**), one can also observe (i) the friction force of the sliding droplet based on the equation of motion ($F_{friction\ droplet} = mg\sin\alpha - m^* dU/dt$, where m is the mass of the droplet, g is the gravity, α is the tilting angle and dU/dt is the acceleration of the droplet)[41], and (ii) the force of the droplet ($F=mg$). Since in this plane, the deformation of lamellae is not observed, we have not considered for explain the effect of the sliding droplet in the deformation of the lamellae.
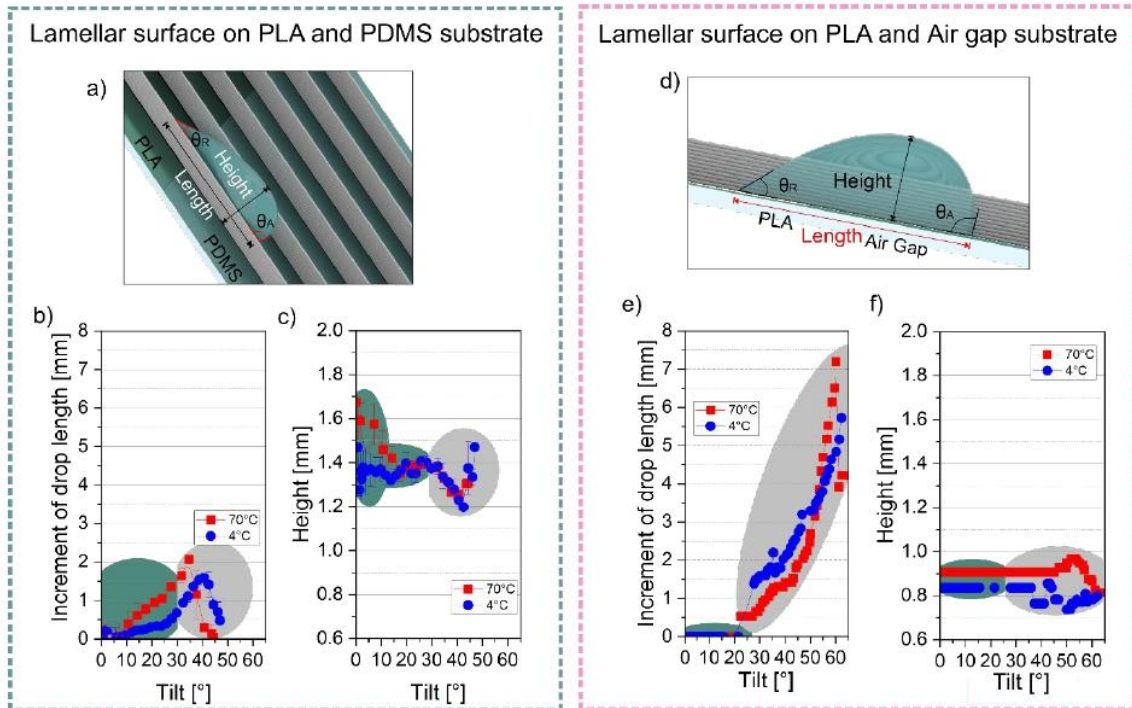
Figure S3. a) Schema of sliding droplet at increasing tilting angle on lamellar surface on PLA and PDMS substrate, and d) on PLA and Air Gap substrate. Length and height measurements of a sliding droplet at increasing tilting angles on the lamellar surface on a combined surface of PLA and PDMS (b-c), and on lamellar surface on PLA-Air gap surface (e-f), respectively.
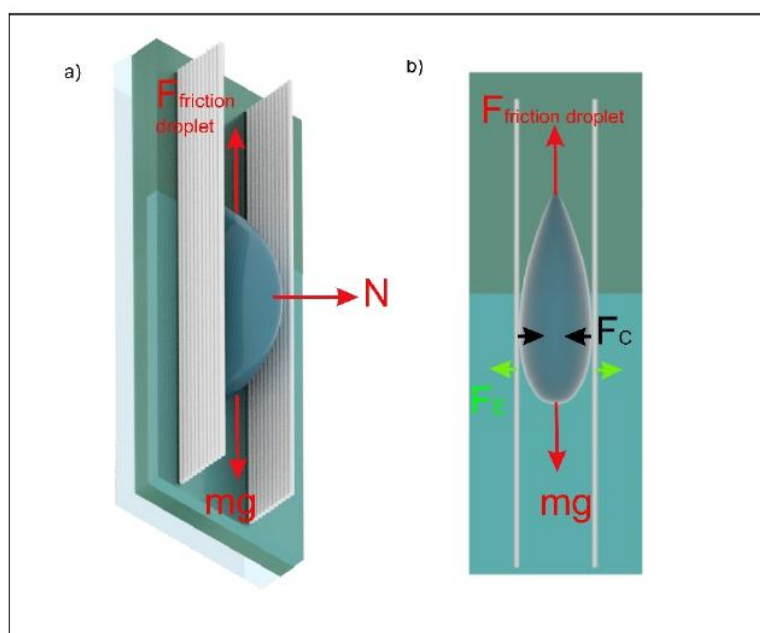
Figure S5. Schema of the forces in the sliding droplet between two lamellae. a) side plane of the diagram, and b) top view.

1. Sadilov, I.; Constante, G.; Dulle, M.; Schönfeld, D.; Pretsch, T.; Ionov, L., Reversibly Switchable Topography Enabled by Melting and Crystallization of Melt-Electrowritten Polymer Fibers. *ACS Materials Letters* **2025,** *7* (2), 401-408.

Acknowledgments

A heartfelt thank you to my family for their unconditional love and support. To my father Luis for his love, to my mother Grace for being the reason that I am here, to my sisters Tati and Mica for being the ones I love the most, and for my beloved granddad Luis for encouraging me to pursue my dreams, and despite his physical absence he still lives on my heart. I must give special thanks to my best friend, my person, Karen, whose unwavering friendship and ability to bring joy into my life have been a constant source of comfort and

happiness. Thanks to Ute and Stefan for being like family to me; your presence has made a significant difference in my journey. I also wish to express my appreciation to relatives and friends, whose companionship has brought colour to my life. Your presence and support, whether near or far, have meant the world to me.

This dissertation is a testament to the collective efforts and support of many individuals. To all who have helped me along the way, I extend my deepest gratitude.

(Eidesstattliche) Versicherungen und Erklärungen

(§ 9 Satz 2 Nr. 3 PromO BayNAT)

Hiermit versichere ich eidesstattlich, dass ich die Arbeit selbstständig verfasst und keine anderen als die von mir angegebenen Quellen und Hilfsmittel benutzt habe (vgl. Art. 97 Abs. 1 Satz 8 BayHIG).

(§ 9 Satz 2 Nr. 3 PromO BayNAT)

Hiermit erkläre ich, dass ich die Dissertation nicht bereits zur Erlangung eines akademischen Grades eingereicht habe und dass ich nicht bereits diese oder eine gleichartige Doktorprüfung endgültig nicht bestanden habe.

(§ 9 Satz 2 Nr. 4 PromO BayNAT)

Hiermit erkläre ich, dass ich Hilfe von gewerblichen Promotionsberatern bzw. - vermittlern oder ähnlichen Dienstleistern weder bisher in Anspruch genommen habe noch künftig in Anspruch nehmen werde.

(§ 9 Satz 2 Nr. 7 PromO BayNAT)

Hiermit erkläre ich mein Einverständnis, dass die elektronische Fassung meiner Dissertation unter Wahrung meiner Urheberrechte und des Datenschutzes einer gesonderten Überprüfung unterzogen werden kann.

(§ 9 Satz 2 Nr. 8 PromO BayNAT)

Hiermit erkläre ich mein Einverständnis, dass bei Verdacht wissenschaftlichen Fehlverhaltens Ermittlungen durch universitätsinterne Organe der wissenschaftlichen Selbstkontrolle stattfinden können.

Bayreuth, 07.07.2025

……………………………………………………………………………………..
Ort, Datum, Unterschrift